Passive Magnetic Shielding Characterisation for Static Fields within the BeamEDM Experiment

Masterarbeit der Philosophisch-naturwissenschaftlichen Fakultät der Universität Bern

Albert Einstein Center for Fundamental Physics
Laboratory for High Energy Physics (LHEP)

vorgelegt von
Alexander Gottstein

März 2021

Leiter der Arbeit:
Prof. Florian Piegsa

Abstract

Within the scope of the BeamEDM experiment – a novel experimental approach to search for the neutron's electric dipole moment using pulsed neutron beams – a two-layer MuMetal shielding is employed to passively shield magnetic background fields. The shielding was preliminarily characterised for its shielding capacity using a mapper wagon equipped with five fluxgate magnetometers. This thesis focuses on the shielding of static magnetic fields generated by Helmholtz-like magnetic coils. Shielding factors are calculated for longitudinally and transversely applied magnetic fields, by comparing the measured field strengths before and after the shielding's installation. Shielding factors of 41 and 200 are found for longitudinal and transversal fields, respectively. For the final BeamEDM shielding design featuring feedthrough cylinders, the shielding capability is reduced locally by up to 30%. A preliminary analysis of magnetic field data recorded during the August 2020 BeamEDM beamtime at Institute Laue–Langevin (ILL), Grenoble, affirms the passive magnetic shielding's effectivity, also in combination with the utilised active magnetic field stabilisation.

Contents

1 | Introduction

This thesis documents the work conducted within the scope of the master's project. The master's project has been conducted within the framework of the BeamEDM project, an experiment in development by the Fundamental Neutron and Precision Physics research group at the laboratory for high energy physics (LHEP) of the University of Bern.
In the first section of the thesis the most important theoretical concepts are explained, that are needed for a well-based discussion and profound understanding of the subsequent subjects. In a first step, the basic idea behind the neutron's electric dipole moment (nEDM) and the associated physics are explained, as well as the basic concept of the experimental searches for it using a pulsed neutron beam, as this is the novel working principle of the BeamEDM experiment. This part is followed by a theory block that explains the concepts of magnetic shielding and the measurements associated with it.
Subsequently, the documentation of the magnetic shielding characterising measurements conducted in the scope of this thesis follows. This contains a detailed description of the experimental set-up with which the preliminary characterisation of the passive magnetic MuMetal shielding was conducted. The results obtained for the shielding characterisation for static magnetic fields are discussed and compared to theoretical and simulated results of comparable shieldings. In a last part, magnetic field data recorded during the first beam time of BeamEDM featuring a MuMetal shielding are analysed. Based on this analysis the laboratory shielding effectivity is revised.

1.1 | Searching for the Neutron's Electric Dipole Moment

The subatomic world currently is best described by the Standard Model (SM) of particle physics. Although it has its known flaws, the SM delivers theoretical predictions for certain phenomena which have been verified experimentally with a startling precision. A fundamental concept within the SM is the existence of abided symmetries. Until 1956, when the famous *Wu experiment* [1] was conducted, it was believed that the world, as how it was described by then known physics, was symmetric under charge conjugation (C), parity transformation (P), and time reversal (T). The Wu experiment, however, showed, that the P-symmetry is not only violated but maximally broken within the beta decay of ^{60}Co. Further on, the violation of CP symmetry, the combination of the standalone C and P symmetries, was shown in the decay of K mesons in 1964 [2].
CPT-symmetry breaking – the violation of the combined symmetry of the three standalone symmetries C, P and T – however, is still unobserved. The invariance of the SM under CPT-transformations is postulated by the CPT theorem [3, 4]. A consequence that follows from the CPT theorem is that if a pair of symmetries, e.g. CP, is violated, then the third standalone symmetry (in this case T symmetry) has to be violated as well, in order to preserve CPT invariance.
The CP violation was included within the SM by Cabibbo, Kobayashi and Maskawa, who introduced a CP violating phase in the CKM matrix, which related the quark's mass eigenstates with their flavour eigenstates in weak interactions [5]. CP violation is an important factor in current big questions in physics, such as the presence of a matter-antimatter asymmetry within the observable universe. For the formation of a universe with such an asymmetry, also called the baryon asymmetry of the universe (BAU), CP and C violation are one of three necessary conditions[1] that have to be fulfilled according

[1] The other two conditions being Baryon number violation and interactions out of thermal equilibrium.

to the proposal of the Russian physicist A. Sakharov in 1967 [6]. From cosmological observations the universe's baryon asymmetry η is measured to be about

$$\eta = \frac{\eta_B - \eta_{\overline{B}}}{\eta_\gamma} = 6.1^{+0.3}_{-0.2} \times 10^{-10}, \tag{1.1}$$

where η_B ($\eta_{\overline{B}}$) is the number density of (anti-)baryons in the universe and η_γ is the number density of photons, estimated from CMB observations [7, 8]. The CP violating processes allowed within the electro-weak sector of the SM are currently deficient to describe a baryon asymmetry of this order of magnitude. An estimate with parameters from the standard cosmological model estimates a baryon asymmetry of about $\eta \simeq 10^{-18}$ [9], which is off of the observed value by eight orders of magnitude.
Besides the CP violation originating in the CKM description of weak interactions, a second source of CP violation is present in the SM. A CP-odd term is found within the QCD Lagrangian, i.e. the vacuum polarisation term [10]. This term features a mixing angle $\bar{\theta}$, which determines the strength of CP violation, and in principle could take on any value from 0 to 2π.

The Neutron's Electric Dipole Moment (nEDM)

The SM's prediction for CP violation can be probed by measuring the electric dipole moment of the neutron (nEDM), as its existence would imply a direct violation of P and T symmetry. This becomes evident by looking at the interaction Hamiltonian of a neutron in an electric ($\vec{E}$) and magnetic ($\vec{B}$) field in the non-relativistic limit,

$$\mathcal{H} = -\vec{d_\mathrm{n}} \cdot \vec{E} - \vec{\mu}_\mathrm{n} \cdot \vec{B}, \tag{1.2}$$

where $\vec{\mu}_\mathrm{n}$ is the neutron's magnetic moment and $\vec{d_\mathrm{n}}$ is its electric dipole moment. By separately applying the parity operators $\hat{P}$ and $\hat{T}$ to the Hamiltonian, its parity violating nature becomes apparent:

$$\hat{P}\mathcal{H} = -\vec{d_\mathrm{n}} \cdot \left(-\vec{E}\right) - \vec{\mu}_\mathrm{n} \cdot \vec{B} \qquad \neq (\pm 1)\mathcal{H}, \tag{1.3a}$$

$$\hat{T}\mathcal{H} = -\left(-\vec{d_\mathrm{n}}\right) \cdot \vec{E} - (-\vec{\mu}_\mathrm{n}) \cdot \left(-\vec{B}\right) \neq (\pm 1)\mathcal{H}. \tag{1.3b}$$

From (1.3b) alone and the implications of the CPT theorem we can conclude that a non-vanishing nEDM entails a violation of CP symmetry. From both sources of CP violation within the SM a theoretical estimation for such a nEDM can be made. The CP violating phase in the CKM-matrix allows for a prediction of the nEDM [11] of the size $d_n^{\mathrm{CKM}} \sim 10^{-32}\ e \cdot \mathrm{cm}$, where e is the elementary charge. This value is way below the current upper limit set by nEDM experiments conducted at PSI [12] of

$$d_\mathrm{n} = (0.0 \pm 1.1_{\mathrm{stat}} \pm 0.2_{\mathrm{sys}}) \times 10^{-26}\ e \cdot \mathrm{cm}, \tag{1.4}$$

and would be very difficult to detect with current and near future experimental techniques. The second source of CP violation from the QCD-Lagrangian results in a nEDM that is proportional to the mixing angle $\bar{\theta}$ and is equal to $d_\mathrm{n}^{\mathrm{QCD}} \simeq \bar{\theta} \cdot 1 \times 10^{-16}\ e \cdot \mathrm{cm}$. Together with the limit from (1.4) we can set an experimental limit on the mixing angle as $\bar{\theta} \lesssim 10^{-10}$. This inflicts a problem of naturalness on the mixing angle, which is known as the *strong CP problem*. The value seems to be unnaturally small - fine-tuned as the saying goes - as currently no underlying mechanism regulates the value of the angle by means of natural parameters, i.e. dimensionless parameters of order 1.

The task of searching for the nEDM is therefore relevant from several points of view, however, due to the seemingly small size of d_n it is not an easy one. Experiments that are looking for a nEDM are all based on the same general idea of exposing neutrons to strong static magnetic and electric fields, leading to a precession of the neutrons, whose frequency allegedly changes under polarity reversal of the electric field. It is this frequency shift that possibly entails the measurable value of the nEDM. This is based on the following effect: Neutrons exposed to an external magnetic field feel a torque $\vec{M} = \vec{\mu} \times \vec{B}$ that leads to a precession of the neutrons magnetic moment about the magnetic field, the so-called Larmor precession. The angular frequency ω_L of this precession, called the Larmor frequency, is given by

$$\omega_\mathrm{L} = -\gamma_\mathrm{n} |\vec{B}|, \tag{1.5}$$

where $\gamma_\mathrm{n} = -2\pi \cdot 29.1646943(69)\ \mathrm{MHz\,T^{-1}}$ is the neutron's gyromagnetic ratio. From the neutron's Hamiltonian in (1.2) we can see that the existence of a nEDM entails a similar effect to the neutrons precession in the presence of an electric field, i.e. we have an additional pseudomagnetic precession $\vec{\omega}_E = d_\mathrm{n}\vec{E}$. Ongoing nEDM experiments are essentially searching for the frequency shift that occurs when the magnetic and electric field are set parallel and anti-parallel, where the respective precession frequencies are given by

$$\omega_{\uparrow\uparrow} = \frac{2}{\hbar}\left(2\mu_\mathrm{n}B + d_\mathrm{n}E\right), \tag{1.6a}$$

$$\omega_{\uparrow\downarrow} = \frac{2}{\hbar}\left(2\mu_\mathrm{n}B - d_\mathrm{n}E\right). \tag{1.6b}$$

From measuring both precession frequencies $\omega_{\uparrow\uparrow}$ and $\omega_{\uparrow\downarrow}$ one can then quantify a value for the electric dipole moment as

$$d_\mathrm{n} = \frac{\hbar \cdot (\omega_{\uparrow\uparrow} - \omega_{\uparrow\downarrow})}{4E}. \tag{1.7}$$

In the BeamEDM experiment, described in the upcoming subsection, this frequency shift $\Delta\omega = (\omega_{\uparrow\uparrow} - \omega_{\uparrow\downarrow})$ is measured between two separate interaction zones for neutron beams. For the two neutron beams the magnetic field is held constant and at the same level, but the electric field polarity is different for the two. For an electric field strength of $E = 40\,\mathrm{kV\,cm^{-1}}$ a frequency shift of $\Delta\omega/2\pi \lesssim 425\,\mathrm{nHz}$ needs to be assessed, in order to match the current upper limit from (1.4). Beyond that, equation (1.7) only legitimately follows from equations (1.6) with the assumption of having the same constant magnetic field in both interaction zones. A small inhomogeneity in the magnetic field ΔB can already mimic a false nEDM signal on the order of

$$d_\mathrm{false} = -\frac{\mu_\mathrm{n}\Delta B}{2E}, \tag{1.8}$$

which means that with the same electric field configuration we need to be sensitive to magnetic field inhomogeneities of at least $\Delta B \approx 20\,\mathrm{fT}$. Magnetic field changes of such low magnitudes can already occur from the process of electric field reversal itself or from HV breakdowns. An electric field reversal could change the magnetisation of a surrounding object for instance, which could then change the overall magnetic field. Depending on the experimental method, different approaches can be used to minimise such magnetic field changes. For nEDM experiments using neutron beams for example, a two beam-method can be deployed, where simultaneously both field alignments (i.e. $\omega_{\uparrow\uparrow}$ and $\omega_{\uparrow\downarrow}$) are measured. With this method, on the other hand, one would be sensitive to magnetic field gradient drifts occurring over the measurement period. As a consequence, nEDM

experiments deploy active and passive magnetic shielding methods which minimise the arising magnetic field changes. Moreover, the local magnetic field can be monitored using magnetometers, so that a change in magnetic fields can be recorded and taken into account in post-process data analysis. A consequence of using a beam of cold neutrons, i.e. neutrons with velocities of $v_\mathrm{n} \sim 1000\,\mathrm{m\,s^{-1}}$, is, that we are also sensitive to a systematic effect called the $v \times E$ effect. This effect arises from relativistic considerations. A particle moving through an electric field will see - from its rest frame point of view - a moving magnetic field. The emerging magnetic field of

$$\vec{B}_{v\times E} = -\gamma \frac{\vec{v} \times \vec{E}}{c^2} \tag{1.9}$$

leads to a false nEDM signal, where γ is the Lorentz factor, which is approximately 1 for cold neutrons. With a small misalignment of an angle α between the electric field and the magnetic field the $v \times E$ effect has a first order impact on the frequency shift $\Delta\omega$ of

$$\Delta\omega \approx -\gamma_\mathrm{n} \cdot \alpha \frac{vE}{c}. \tag{1.10}$$

As can be seen, however, the effect is linear in the neutron's velocity v. This fact is what the novel concept of the BeamEDM experiment wants to take advantage of.

In general, employing standard error propagation on equations (1.7) and (1.8), the sensitivity of a nEDM search [10] is given by

$$(\delta d_\mathrm{n})^2 = \sigma^2(d_\mathrm{n}) + 2\left(\frac{\mu_\mathrm{n}}{2|E|}\delta B\right)^2, \tag{1.11}$$

where the first term is the experiments statistical counting sensitivity and the second term the one originating in systematic effects related to magnetic field inconsistencies, gathered in the term δB.

The BeamEDM Experiment

The experimental approaches trying to determine a nEDM by measuring the frequency shift from equation 1.7 make use of Ramsey's separated oscillating fields method [13], which builds on Rabi's resonance method [10]. The experiments currently setting the lowest upper limits for a nEDM apply this method to ultracold neutrons (UCN) in so-called storage experiments. UCN's have a lifetime of more than 14 minutes [14], which is a very long lifetime compared to other instable hadrons [15]. This is advantageous, as in general, the statistical sensitivity for the frequency shift measurements relevant for nEDM experiments goes as

$$\sigma(d_\mathrm{n}) \propto \frac{\hbar}{ET\sqrt{N}}, \tag{1.12}$$

where E is the electric field strength, T is the interaction time of the neutrons with the field and N is the amount of measured neutrons [10]. Having a long neutron lifetime therefore is beneficial as it allows for long interaction times T.
A different approach is chosen for the BeamEDM experiment, though. Instead of using Ramsey's method for UCN's, the neutron interferometry method is applied to a beam of cold neutrons. It has the advantage of a much higher neutron rate N, which compensates for the entailing lower interaction time T. A downside of beam experiments, however, is that they were currently limited by the systematic $v \times E$ effect, which comes along with the directed motion of neutrons. This is where BeamEDM's concept of using pulsed neutron beams comes into play [16]. BeamEDM is a novel nEDM experiment that is planned to be

conducted at the planned *European Spallation Source* (ESS). The latest proof-of-concept (POC) experiment took place in August 2020 at the PF1b neutron beam facility [17] of Insitute Laue-Langevin in Grenoble, France. A picture of the installed experimental set-up is shown in figure 1.1. Compared to the foreseen 50 m long beamline the POC set-up featured a 6 m long beamline with 3 m of HV interaction length. The working principle of the POC BeamEDM experiment at ILL is explained hereafter.

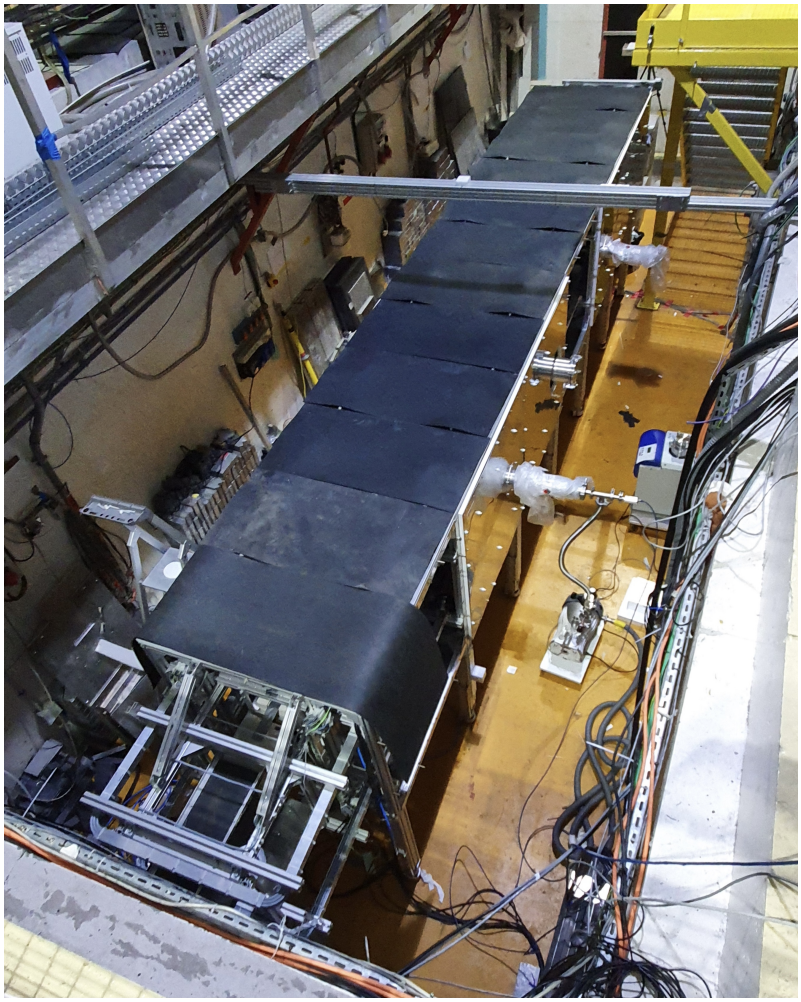

Figure 1.1.: The BeamEDM set-p at the polarised cold neutron beam facility PF1b of Institute Laue-Langevin, Grenoble, France, in August 2020. The bottom of the picture shows the upstream end of the set-up where the neutron beam enters the beamline. The whole set-up is covered by a MuMetal shielding (however, two side panels are missing in this picture) and a layer of lead rubber for radioprotective reasons.

A beam of cold neutrons (mean wavelength of 4.0 - 4.5 Å, corresponding to a velocity of approximately 930 m s^{-1}) is extracted from a vertical liquid deuterium cold source and guided to the experimental facility [17], where they arrive in a horizontally polarised state. After leaving the neutron guide, a magnetic guidance field repolarises the neutrons vertically. Before the neutrons are released into the BeamEDM set-up, a Fermi-type chopper [18] pulses the continuous neutron beam. Having a pulsed beam is a key concept of the experiment that helps us to get rid of certain systematic effects, as will be explained later. Using simple beam apertures, the neutron beam is split into two separate beams, a lower and an upper one. In a first stage the two polarised beams enter a spin-flipping device, where the neutron spins are flipped by 90°. This is realised by generating a magnetic AC field with a frequency equal to the neutrons' Larmor frequency from equation

(1.5). The spin-flip of the neutrons initiates a Larmor precession around a vertically applied static and homogeneous magnetic field $\vec{B}_0$, that is generated by a rectangular set of Helmholtz coils and spans across the entire beamline. After entering a nonmagnetic vacuum flight tube, the neutrons travel across the entire beamline where, besides the magnetic field $\vec{B}_0$, they are exposed to constant high-voltage electric fields, $\vec{E}_1$ and $\vec{E}_2$, with opposite polarities for the two beams. After a certain interaction length the neutrons, again, get spin-flipped by 90° and reach a neutron spin-analyser that separates the two neutron beams into four beam-spots that are recorded with a neutron detector. A non-vanishing nEDM could be detected in that way, since the presence of the electric fields would lead to a phase shift of the neutrons between the two beams, which would translate into an detectable asymmetry between the upper and the lower beam spots, shown in figure 1.2.

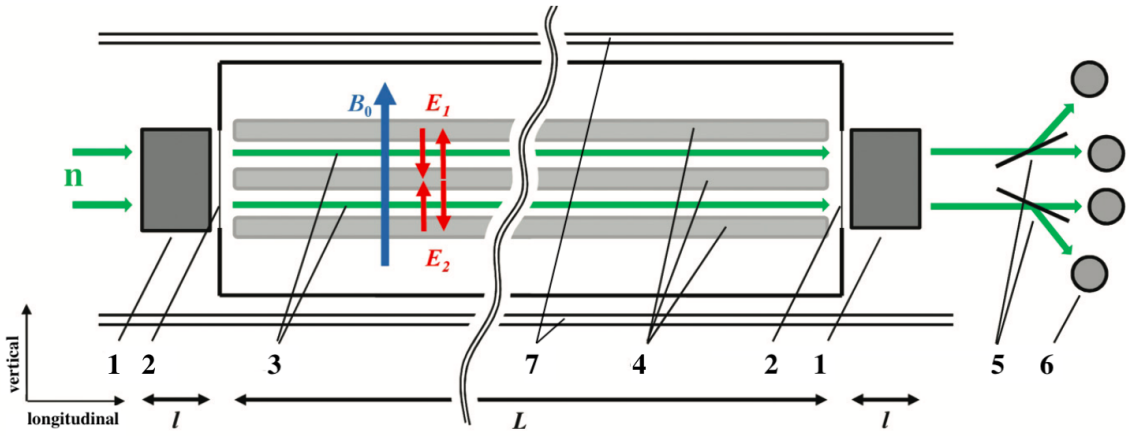

Figure 1.2.: BeamEDM scheme taken from [16]. The neutron beams' paths are indicated in green. (1) $\pi/2$ spin-flippers of length l (2) Aluminium windows for vacuum tube beam entry (3) upper and lower neutron beam interacting with local magnetic and electric field (4) HV electrodes of length L generating the electric fields $\vec{E}_1$ and $\vec{E}_2$ in vertical direction (5) spin-analysing supermirrors (6) neutron detectors (7) two-layer MuMetal shielding covering the whole set-up

The advantage of a pulsed beam instead of a continuous beam is that one can get rid of the systematic $\vec{v} \times \vec{E}$ effect, as the velocities of the detected neutrons can be determined by their time of flight. Since the $\vec{v} \times \vec{E}$ effect manifests itself linearly with the neutron velocity in the measured frequency shift (see equation (1.10)) it can be separated from other magnetic spin interaction effects. Furthermore, using two beams simultaneously allows for the compensation of global magnetic field drifts. However, as a downside, the measurement gets sensitive to changes in the magnetic field gradients between the two beams. As a countermeasure, the magnetic field and its gradient inside the neutron beamline is constantly monitored using an array of fluxgate magnetometers and two layers of MuMetal shield the whole set-up from disturbing magnetic field sources. The characterisation of said MuMetal shielding is topic of this thesis.

2 | Theory

This chapter presents the derivation of certain theoretical calculations that are used within this thesis. First, an approach is explained with which the magnetic field generated by Helmholtz-like coil arrangements are readily calculated. In a second part the basic concepts of magnetic shielding theory are explained, with which most shielding related phenomena occurring in this thesis can be explained. In a last part the basic measurement concept of a fluxgate magnetometer is explained, since this measuring instrument is of central importance in this thesis.

2.1 | Analytic Solution for Magnetic Fields generated by rectangular Helmholtz Coils

We are interested in the magnetic field that is generated by a rectangular pair of Helmholtz coils. One way to calculate this would be using the Biot-Savart law. Another easier way to calculate the magnetic field is conducted by formulating the magnetic vector potential $\vec{A}$ and its curl, as by definition,

$$\vec{B} = \nabla \times \vec{A}, \qquad \vec{E} = -\nabla\phi - \partial_t \vec{A}, \tag{2.1}$$

where $\vec{E}$ is the electric field and ϕ is the (scalar) electric potential. For a rectangular coil with length $2l$ and width $2b$ laying centred in the x-y plane, the relation of the B field and it's vector potential can be written as

$$B_x = -\partial_z A_y, \quad B_y = \partial_z A_x, \quad B_z = \partial_x A_y - \partial_y A_x. \tag{2.2}$$

According to [19] the components of the vector potential $\vec{A}$ for the rectangular coil can then be written as

$$A_x = \frac{\mu_0 I}{4\pi} \ln\left[\frac{(r_1 + l + x)(r_3 - l + x)}{(r_2 - l + x)(r_4 + l + x)}\right], \quad A_y = \frac{\mu_0 I}{4\pi} \ln\left[\frac{(r_2 + b + y)(r_4 - b + y)}{(r_3 - b + y)(r_1 + b + y)}\right], \tag{2.3}$$

where μ_0 is the magnetic permeability of vacuum, I is the electric current running through the coil and the coefficients r_i are denoting the distances between the four corners of the rectangular coil and a certain point with coordinates x, y and z. They are defined as

$$r_1 = \sqrt{(l + x)^2 + (y + b)^2 + z^2}, \tag{2.4a}$$

$$r_2 = \sqrt{(l - x)^2 + (y + b)^2 + z^2}, \tag{2.4b}$$

$$r_3 = \sqrt{(l - x)^2 + (y - b)^2 + z^2}, \tag{2.4c}$$

$$r_4 = \sqrt{(l + x)^2 + (y - b)^2 + z^2}. \tag{2.4d}$$

Combining equations (2.2) and (2.3), the magnetic field's z-component can be written as

$$B_z = \frac{\mu_0 I}{4\pi} \sum_{i=1}^{4} \left[\frac{(-1)^i d_i}{r_i \cdot (r_i + (-1)^{i+1} C_i)} - \frac{C_i}{r_i (r_i + d_i)}\right], \tag{2.5}$$

where we have additionally defined

$$\begin{aligned} C_1 &= -C_4 = l + x, \\ C_2 &= -C_3 = l - x, \\ d_1 &= d_2 = y + b, \\ d_3 &= d_4 = y - b. \end{aligned}$$

This is a ready-to-use formula with which the magnetic field's z-component is readily calculated. In the same way the magnetic field's x- and y-component can be written as

$$B_x = \frac{\mu_0 I}{4\pi} \sum_{i=1}^{4} \left[\frac{(-1)^{i+1} z}{r_i \cdot (r_i + d_i)} \right] \qquad \text{and} \qquad B_y = \frac{\mu_0 I}{4\pi} \sum_{i=1}^{4} \left[\frac{(-1)^{i+1} z}{r_i \cdot (r_i + (-1)^{i+1} C_i)} \right]. \tag{2.6}$$

For a scenario with multiple parallelly arranged coils of the same dimensions, the individually generated fields can simply be summed up as

$$B_{j,\text{tot}} = \sum_k B_j(x - x_k, y - y_k, z - z_k), \tag{2.7}$$

where j denotes either x, y or z and the coordinates x_k, y_k and z_k denote the coordinates of the centre of each coil that is considered for the sum. This formula allows for an easy calculation of magnetic fields that we would expect from rectangular Helmholtz coil pairs, such as the ones as described in sections 3.2.2 and 3.2.1.

2.2 | Magnetic Shielding Theory

In this section we look at the basic concepts of magnetic shielding theory, in order to have an idea how our implemented MuMetal shielding works.
Electromagnetic fields do not penetrate all materials equally well. With the right choice of material and geometry of a so called magnetic shielding, electromagnetic fields can be partially prevented from propagating to a certain area, the so called shielded region. This effect can be used for either containing electromagnetic fields in a certain region or vice versa to keep electromagnetic fields away from a certain region (as shown in illustration 2.1).

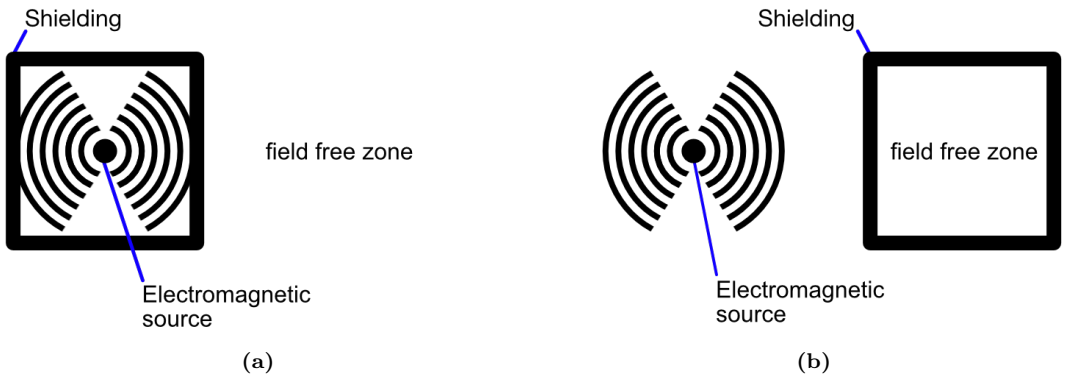

Figure 2.1.: Electromagnetic shieldings can either be used to confine an electromagnetic field within a certain region (a) or to shield a specific zone from external electromagnetic fields (b).

The shielding effectiveness can generally depend on the frequency of the emitted electromagnetic field, the shielding's material parameters and the shielding's geometry [20]. It

is measured e.g. by comparing the magnetic field strength $|\vec{B}|$ at a certain point within the deliberately shielded region in the presence and the absence of the shielding, i.e. we define the shielding effectiveness as

$$\mathrm{SE}_B = \frac{|\vec{B}_0(\vec{r})|}{|\vec{B}_S(\vec{r})|}, \tag{2.8}$$

where $|\vec{B}_0(\vec{r})|$ is the magnetic field strength at a certain spatial point within the shielded region in the absence of the shielding and $|\vec{B}_S(\vec{r})|$ the magnetic field strength at the same spatial point but with the shielding in place[1].

There are two main effects that contribute to the shielding mechanism of a material, i.e. *flux-shunting* and *eddy-current cancellation*. The effect which is dominant, again, generally depends on material properties and field frequency.

Flux-Shunting

To understand how the so-called flux-shunting effect comes into place, consider a static electric field for which the Maxwell equations state that

$$\vec{\nabla} \cdot \vec{B} = 0, \qquad \vec{\nabla} \times \vec{B} = 0. \tag{2.9}$$

Thus, the magnetic flux density $\vec{B}$ is curl- and divergence-free. The same can be said for the magnetic field strength $\vec{H}$, since it is in relation to the flux density by

$$\vec{B} = \mu(H)\vec{H}, \tag{2.10}$$

where μ is the magnetic permeability that can be dependent on the magnetic field strength in general and is a material property that measures the magnetisation of the given material after an exposure to an applied magnetic field.
In a magnetic shielding configuration where a material with magnetic permeability μ_s is in use, following Maxwell's equations, we can state that the normal component of the magnetic flux density $\vec{B}$, as well as the tangential component of the magnetic field strength $\vec{H}$ have to be continuous across the entire shieldings surface [21]. These conditions give rise to the flux-shunting effect. As $\vec{B} = \mu\vec{H}$ has to hold within the shielding material and $\vec{B} = \mu_0\vec{H}$ has to hold in the surrounding air at the same time, the B-field and the H-field are perpendicularly 'drawn' into the shielding on the air-side, whereas inside the shielding they are tangentially redirected with respect to the surface. As a consequence, magnetic flux is pulled towards magnetic shields with high permeability and *shunted* along the shielding, nearly parallel to its surface. The effect of flux-shunting is visualised in figure 2.2a.

Eddy-Current Cancellation

If non-static magnetic fields are involved, a second shielding effect becomes relevant. According to the Maxwell-Faraday equation a time-varying magnetic field is accompanied by a spatially varying electric field. Thus, within the shielding, currents will be induced

[1] In certain literature also the following expression is used for the shielding effectiveness:

$$\mathrm{SE}_B = 20\log_{10}\left(\frac{|\vec{B}_0(\vec{r})|}{|\vec{B}_S(\vec{r})|}\right)$$

Furthermore, for the non-logarithmic expression also the inverse ratio is used sometimes, such that a low shield effectiveness value corresponds to a strong shielding. In this thesis we stick to the expression in equation 2.8.

by the time-varying magnetic field. Now, according to Lenz's law, the induced currents generate a magnetic field themselves, which will directly oppose the change of the varying external magnetic field. The two magnetic fields will cancel out each other to some extent, depending on the resistance of the shielding material, which dictates the strength of the induced current. A visualisation of the eddy current cancellation can be seen in figure 2.2b.
An analytical calculation for the shielding factor of a given shield is, generally speaking, quite complicated and only possible for very simple shield geometries, as Maxwell's equations have to be solved analytically. For geometries that are more complex than e.g. an infinite sheet or a simple sphere or cylinder, we have to rely on numerical methods to calculate the shielding effectiveness such as FEM simulations.
However, as a cylinder is a structure that is comparable to our used BeamEDM shielding set-up, we look at the analytically solved shielding effectivity of said structure in the following section.

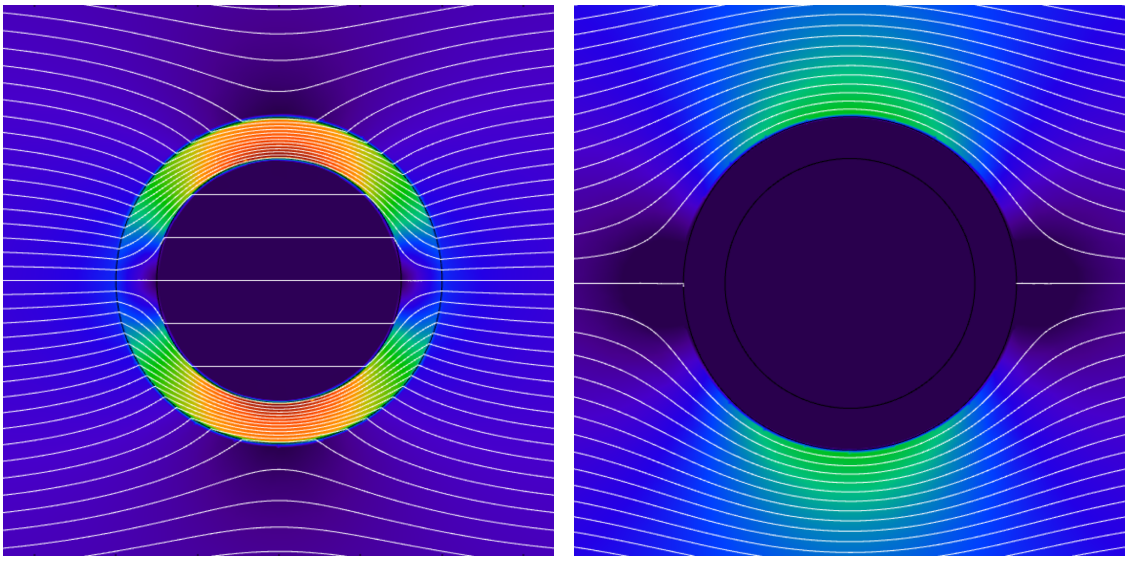

(a) Flux-shunting for a static magnetic field **(b)** Eddy-current cancellation for an alternating magnetic field

Figure 2.2.: The two main mechanisms responsible for magnetic shielding, (a) flux shunting and (b) eddy-current cancellation, schematically shown by means of field lines arrangement for a simulated ring-shaped shielding.

2.2.1 | Static Magnetic Field Shielding in Ideal Set-Ups

For simple shielding geometries such as spherical shells or infinitely long cylindrical tubes exposed to static magnetic fields the shielding factor from equation (2.8) can easily be calculated analytically [22, 23]. For a cylindrical shielding with a large relative permeability μ, i.e. $\mu \gg 1$, and a thickness d that is much smaller than its diameter D, i.e. $d \ll D$, exposed to a surrounding static magnetic field that is applied in a transversal direction to the shielding's orientation, the shielding factor S_T can be calculated by

$$S_T \cong \frac{\mu d}{D} + 1. \tag{2.11}$$

This shielding factor applies only for field strengths B for which the magnetic shielding does not saturate. This is particularly relevant for thin-walled shieldings and for high field strengths. Saturation of a material is reached, when increasing the applied external field strength H does not increase the magnetisation of the material anymore and its permeability μ goes to 1 again. Below the point of saturation where $\mu \gg 1$ the magnetic

flux which is redirected by the shielding is doubled and shared out to two walls. The magnetic flux B within the walls with thickness d is therefore given by

$$B \approx \frac{DB_e}{d}, \qquad B_e = \mu_0 H_e, \tag{2.12}$$

where B_e and H_e are the external magnetic fields, respectively the external magnetic flux density (effect well visible in figure 2.2a). Using the result for the transversal shielding factor S_T, a similar value for a transversely applied static magnetic field can be derived using the so called demagnetising factor N [22], which is a purely geometric factor defined by the length-to-diameter ration $p = \frac{L}{D}$ of the cylindrical shielding [24], and is given by

$$N(p) = (p^2 - 1)^{-1} \left(\frac{p \ln\left[p + \sqrt{p^2 - 1}\right]}{\sqrt{p^2 - 1}} - 1 \right). \tag{2.13}$$

Using the demagnetising factor N, the longitudinal shielding factor for a cylindrical shielding can be calculated from the transversal shielding factor S_T as

$$S_L = 4NS_T + 1. \tag{2.14}$$

As for a infinitely long cylinder, i.e. in the limit of $p \to \infty$, the demagnetising factor N approaches zero ($\lim_{p\to\infty} N = 0$), one can see that only a cylindrical shielding of finite length has an ability to shield longitudinal magnetic fields, where for an infinitely long cylinder the shielding effect vanishes for longitudinally applied fields.

Two-layer Shielding

Following the previous discussion of shielding magnetic fields using a single layer shielding, one can conclude from equations (2.11) and (2.14) that the shielding efficiency can be increased by either increasing the relative permeability μ of the used material or the shieldings thickness d. Another solution to achieve a potent magnetic shielding is to use several layers of magnetic shielding. For example, for a shielding set-up using two cylindrical layers of the same thickness d, inner radii D_1 and D_2 ($D_1 < D_2$) and transversal shielding factors of S_{T1} and S_{T2}, the total shielding factor of the set-up $S_{T,\text{tot}}$ can be calculated as [25]

$$S_{T,tot} = \left(1 - \frac{D_1^2}{D_2^2}\right) S_{T1}S_{T2} + S_{T1} + S_{T2} + 1. \tag{2.15}$$

From this equation we can see that the combined shielding factor of two individual shields has two contributions; on one hand we have the individual shielding factors directly adding up together, and on the other hand we have the first term in equation (2.15) which is a multiplicative combination of the two individual shielding factors. Therefore, in some cases, it can be much more efficient to add a second layer to a shielding to improve it, instead of e.g. choosing a thicker single layer shielding [26].

2.3 | Measuring Magnetic Fields with a Fluxgate Magnetometer

There are several ways to measure a magnetic field's direction and strength, where the most common ones make use of Hall effect sensors, optically-pumped atomic magnetometers (OPMs) or so called fluxgate magnetometers, the latter one being the one of interest for us as we use this kind of magnetometers in our experiment.

A fluxgate magnetometer can be used to determine the direction and the strength of an external magnetic field. Depending on the design of the fluxgate field strengths between 0.1 nT and 1 mT can be measured [27]. The main component of a fluxgate magnetometer is built of two magnetically soft cores that are wrapped by two receiver coils, as it is schematically shown in figure 2.3. The windings of the coils are in opposite direction, so that the induced voltages from an external magnetic field cancel out each other.

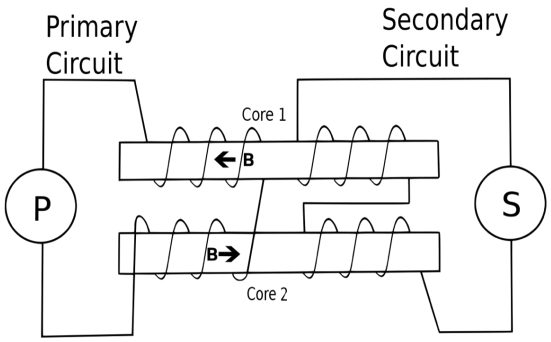

Figure 2.3.: Schematic drawing of a fluxgate magnetometer. Source: [28]

The two coils are divided into an active primary coil and a passive secondary coil. An alternating electric current is passed through the primary coil, which pushes the magnetic cores into alternating states of being magnetised, unmagnetised, inversely magnetised and unmagnetised again. The alternating magnetisation of the core induces an electric current in the secondary coil. This current can be registered and will provide information about the presence of a magnetic field with a component that is parallel to the magnetically soft cores. This is because in the presence of an external magnetic field that is parallelly aligned with the field produced by the primary coil, the magnetic saturation of a core is reached faster than in the absence of a field. In the same time, the field will be antiparallel to the field of the other winding, which will lead to a slower magnetic saturation of the core. The asymmetry between the saturation of the cores leads to a signal measurable by the secondary coil, which is proportional to the external magnetic fields strength.

The fluxgates that were used for the measurements documented in this thesis (Stefan Mayer Instruments, FLC3-70) are triaxial fluxgate magnetometers, meaning they contain three orthogonally arranged coil-core pairs with which the magnetic field vector can be measured relative to the fluxgates orientation. The FLC3-70 is optimised to measure magnetic fields in the range of ± 200 µT and is sensitive for static as well as alternating magnetic fields with frequencies of up to 1 kHz [29].

3 | Description of the Experimental Set-Up as Installed in Bern

3.1 | Aluminium Scaffold

The aluminium scaffold is the skeleton of the BeamEDM experiment. Within the aluminium structure the experiment's key components are installed and held in place. The scaffold is built up in a modular way with its components being 1 m × 1 m × 1 m cubes. Inside the base frame of a cube several additional item profile bars are mounted. Primarily the item profiles form a centred sector within the cube, which will serve as the mounting structure for the beam pipes containing the electrode stacks for the BeamEDM experiment and further important components, such as beam apertures, spin-flippers and fluxgate magnetometers. Furthermore, the item profiles also serve as rails for the later on described magnetic field mapper (see section 3.3). In figure 3.1 a render of the assembled cube stack is shown with the design that was used for the measurements documented and referred to in this thesis. It consists out of six regular cuboid components, with the two end components having additionally attached half-cubes.

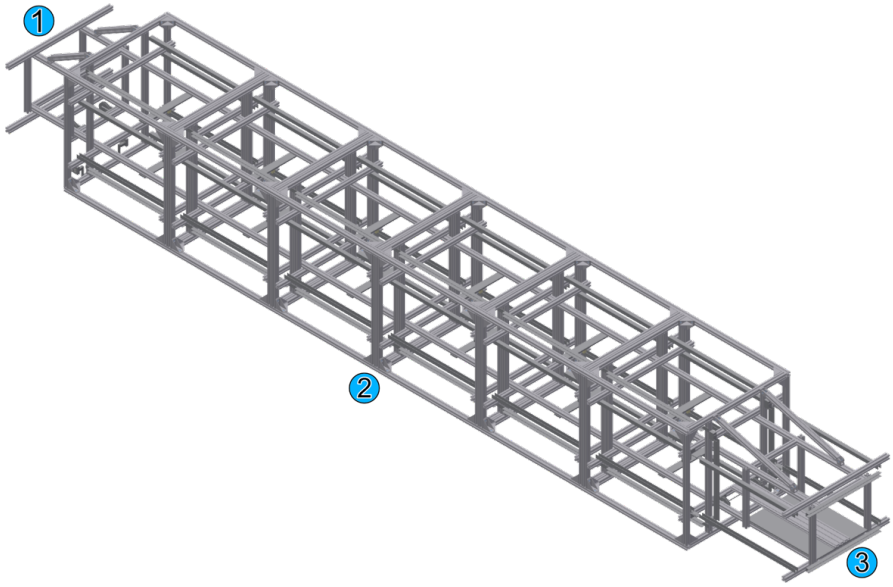

Figure 3.1.: A rendered image of the fully assembled aluminium scaffold, containing six of the modular building blocks and the two custom end pieces. The so called upstream end where the neutron beam will the experimental set-up is labelled with ①, the downstream end where the BeamEDM's spin analyser and detector will be installed is labelled with ③. In between, six identical aluminium cubes of length 1 m are installed (②).

Rendered pictures of a regular intermediate cube are shown in figure 3.2. Also the inner structure of a cube is readily visible in the front view render. The outer side length of the centrally formed cuboid structure is 57 cm, as indicated in figure 3.2b.

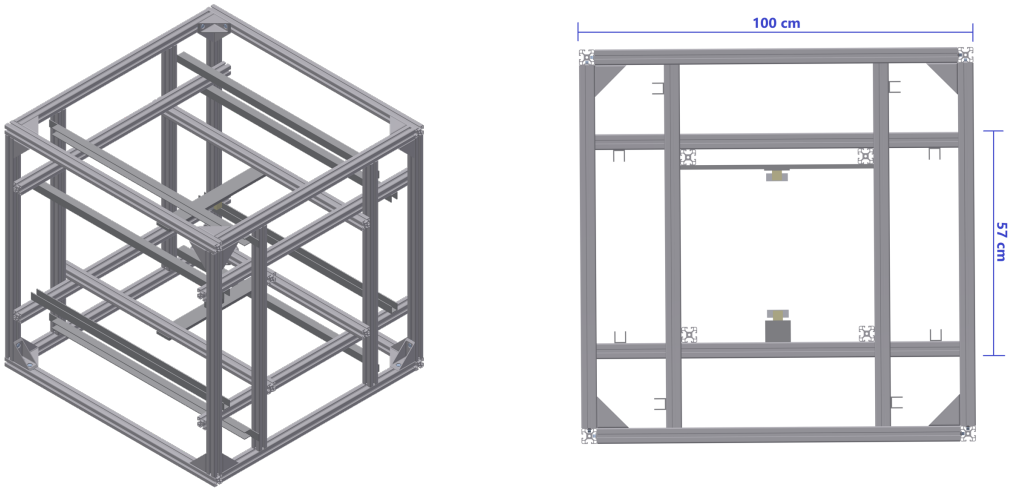

(a) Orthogonal view render **(b)** Front view render

Figure 3.2.: Rendered pictures of a single cuboid component of the modular aluminium scaffold. The outer framework with a side length of 1 m features an inner structure that is used for the installation of vacuum pipes for the BeamEDM experiment. In (b) the U-shaped channels used for the installation of beamline coils (see section 3.2.1) can be seen. The two pieces mounted on the horizontal bar at the centre part are used for the installation of fluxgate magnetometers responsible for the monitoring of the magnetic field during nEDM data taking.

Once assembled to a single structure, the whole line of cubes is put onto pairs of legs, that are attached at the intermediate sections between two cubes and, to some extent, hold together the cubes. The legs are adjustable in height each on its own such that a horizontal alignment of the whole set-up can be guaranteed.

Ending Pieces

Both cubes on the ends have a special attachment each, that serve as a framework for instruments that need to be mounted prior and subsequent to the magnetically shielded beamline, such as BeamEDM's neutron detector or its neutron beam apertures. Furthermore, an additional aluminium RF shielding has been designed that can be attached at the ending pieces. The details for the RF shielding are described in section 3.4.3. A CAD render of both special ending parts can be found in figure 3.3.

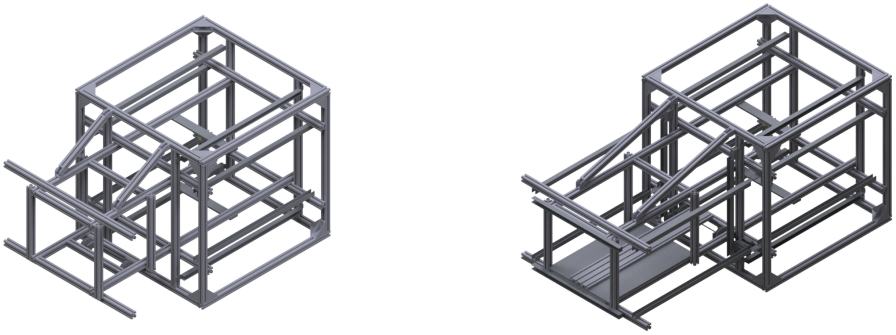

(a) Upstream end **(b)** Downstream end

Figure 3.3.: Rendered images of both special ending parts, attached to the respective cube. In (a) the upstream ending is shown, which serves as a mounting aid for neutron beam apertures used in the BeamEDM experiment, inter alia. In (b) the larger downstream ending is shown. The present aluminium plate and the profile bars on top of it are used for the installation of the spin analyser.

3.2 | Magnetic Coils

For the BeamEDM experiment a magnetic field of constant magnitude and direction is required within the beam line (as described in section 1.1) which is produced by Helmholtz-like magnetic field coils that are installed inside the aluminium scaffold. Three such coil pairs have been installed so that magnetic fields can be generated in all three directions independently.
Furthermore, to determine the shielding efficiency of the later on installed MuMetal shielding for externally generated magnetic fields, additional Helmholtz-like magnetic coils have been installed in the laboratory. Again, for each direction a coil pair has been installed. Both sets of magnetic field coils are described in the following section.

3.2.1 | Beamline Coils

For the purpose of the generation and stabilisation of a constant magnetic field for the BeamEDM experiment, three pairs of so called *beamline coils* are installed within the aluminium scaffold, a pair for each direction, i.e. longitudinal, horizontal and vertical. The coil pairs can be controlled independently. All three coil pairs are simultaneously used for magnetic field generation but also active field stabilisation. The coil windings are, therefore, split up into separate pairs, that are controlled independently as well. In this thesis, however, only the field generation part is described and discussed, whereas the magnetic field stabilisation is not part of the discussion.

Longitudinal Field Coil

The magnetic coil that produces and controls the magnetic field along the longitudinal direction consists out of a single cable with five cores (nominal wire size of $1\,\mathrm{mm}^2$ per core) in it, that is being wound around the aluminium frame as indicated in figure 3.4. For our measurements four wires are used for the magnetic field generation and the fifth wire is used for magnetic field stabilisation.
The entire longitudinal coil is made from a single cable. The coil winding is designed in such a way that the magnetic field generated by the cable part leading forth and the part leading back roughly cancel out each other. The distance between two coil loops is approximately 20 cm.

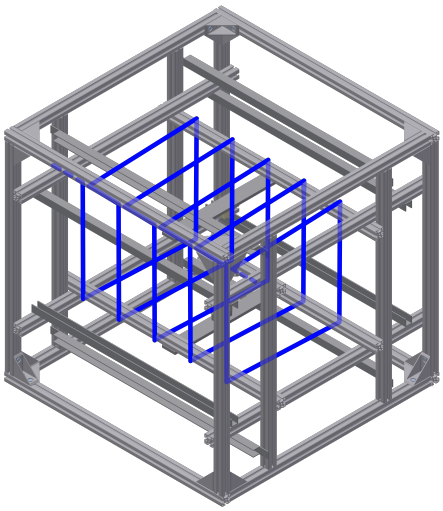

Figure 3.4.: Longitudinal coil winding scheme illustrated on a single cube. The distance between the loop windings is 20 cm.

Vertical Field Coils

The magnetic coils in vertical direction are the main coils of the BeamEDM experiment. A field of about 220 µT is desired in the vertical direction [16], which enforces the Larmor precession of the neutrons that are exposed to it. The vertical field coils are built up in a different modular way than the aluminium scaffold, as the individual coil components are of 2 m length. The main components consist of an aluminium U-channel that contains a bundle of nine cables. With each cable containing five copper wires (nominal wire size of 2.5 mm^2 per wire) we have a total amount of 45 windings available for both, the generation and stabilisation of vertically directed magnetic fields. Each cable ends in a polyamide plug and socket connector (*160 BU/ 5 DSS*) on each end. Due to the size of the connectors, bulges of wire form at the interconnecting pieces, as shown in figure 3.5b. At each ending of the aluminium scaffold custom shaped aluminium U-channels are used to close the coil loop. On the upstream end the coils reach out 60 cm out of the main scaffold structure, whereas on the downstream end the coils reach out 100 cm of the structure. This is also indicated in figure 3.5a.
Out of the 45 available wire windings, 35 are used for the field generation and five are used for the magnetic field stabilisation. The remaining five are used for the generation and the stabilisation of a magnetic field gradient along the vertical direction. The gradient field coils can either be used to compensate for an unwanted occurring magnetic gradient field during EDM measurements or for controlled monitoring of systematic effects of such a gradient field. The respective gradient field loops in the lower coil are therefore connected in opposite winding direction to the loops in the upper coil. Four of the five wire windings are assigned for the gradient generation while the remaining single winding is used for the stabilisation of the gradient field.

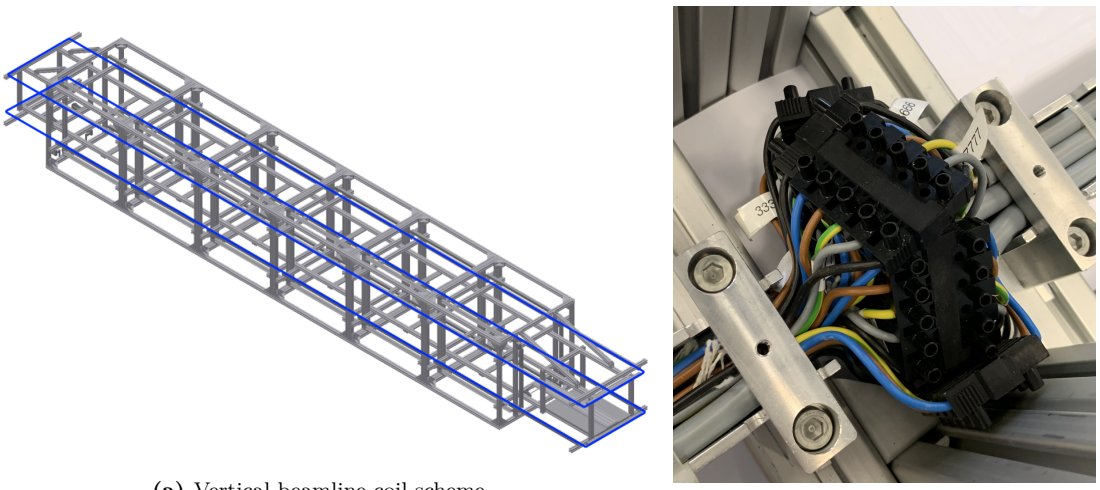

(a) Vertical beamline coil scheme

(b) Wire connector bulge

Figure 3.5.: A schematic illustration of the design of the vertical field beamline coils highlighted in blue is shown in (a). On both ends the coil loops reach out of the main scaffold structure, as they extend up to the very end of the custom end pieces. In (b) a bulge is shown that forms after the first, third and fifth cube, due to the size of the used 160 BU socket connectors.

Horizontal Field Coil

The coil pair for the horizontally directed magnetic field is build up in a similar way like the vertical coil. The difference is, however, that the coil loop is built up from the same type of cable as the longitudinal field coil (nominal wire size of 1 mm^2 per core) which is arranged together in an accordingly smaller aluminium U-channel. Furthermore, the bars

are only of a length of 1 m and a different type of connectors is used, i.e. 4.2 mm *Pitch Mini-Fit Jr.* connectors. Unfortunately, these connectors feature a much higher electrical resistance than those of the vertical coil, which has to be considered in the choice of power supply. The coil loops are closed with a U-channel bar that is attached vertically to the outer side of the ending cubes. These U-channels are flush to the item profiles that are on the edge level of the MuMetal shielding and therefore are not enclosed by any MuMetal shielding. This is also shown in figure 3.6.

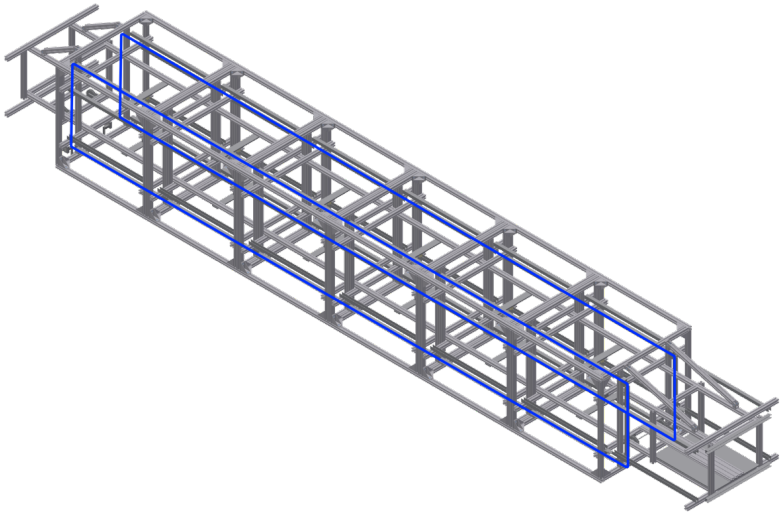

Figure 3.6.: A schematic illustration of the design of the horizontal field beamline coils that are highlighted in blue.

Power Supply and Resistances

The beamline coils for the longitudinal and horizontal field generation are each powered independently by a *KEYSIGHT E3634A DC Power Supply*. The main beamline coil for the vertical field generation is powered by a *FUG NTN 1400*. To reduce the signal that is being picked up by the beam line coils from electromagnetic induction (documented in detail in [30]) additional 200 Ω power resistors are connected in series with the coil. This is not further discussed, as for static field measurements, on which this thesis focuses on, the induction of signals is negligible.

The electrical resistances of the beamline coils have been measured and are documented in table 3.1.

Field Type	**Cable Wind.**	**Wire Wind.**	**Resistance**
Longitudinal (B Set)	1	4	13.1 Ω
Longitudinal (B Stab)	1	1	3.2 Ω
Horizontal (B Set)	8	40	77.1 Ω
Horizontal (B Stab)	1	5	10.2 Ω
Vertical (B Set)	7	35	10.9 Ω
Vertical (B Stab)	1	5	1.8 Ω
Vertical grad. (ΔB Set)	1	4	1.6 Ω
Vertical grad. (ΔB Stab)	1	1	0.7 Ω

Table 3.1.: Measured resistances of each beamline coil loop pair. For each direction a coil pair is present for field generation (*B Set*) and for field stabilisation (*B Stab*). For the vertical direction a gradient field (ΔB) can be generated and stabilised additionally.

3.2.2 | Room Coils

The room coils are installed as sketched in figure 3.7. The Helmholtz-coil pairs for the magnetic field generation in horizontal and vertical direction are made from two rectangular coil loops wound along the floor and ceiling (11.9 m × 4.2 m), and along the side walls respectively (11.9 m × 3.4 m). For the generation of the longitudinally directed magnetic field four rectangular coil loops are installed parallelly to the front and back walls (4.2 m × 3.4 m) in a roughly equidistant manner, where there is a 4 m spacing between each coil loop.
Due to the presence of a pillar at a position in the laboratory where one of the longitudinal coils should pass along, the one coil loop positioned near the upstream end of the scaffold features a buckling, as indicated in figure 3.7.
All coil loops have the same number of windings ($N = 5$) as they are made from a single wound five-core cable type (nominal wire size of 2.5 mm^2 per wire core). They are powered with a *KEPCO BOP 20-20DL* power supply. The power supply can be remotely controlled via the same LabVIEW VI that also controls to magnetic field mapper measurements, where an additional waveform generator is interposed between the *KEPCO* and the controlling PC. In this way the mappers measurement plan can be synchronised with e.g. the frequency of the generated room coil field.
To get an idea about the magnetic field strength that is generated by Helmholtz coils of such geometries as we have them in the laboratory, with the theory of section 2.1 we can calculate the expected field strength e.g. at the very centre of the unshielded aluminium scaffold. The calculated values are listed in table 3.2.

Longitudinal	Horizontal	Vertical
1.283 µT/A	1.004 µT/A	1.247 µT/A

Table 3.2.: Theoretical magnetic fields at the room's centre reached by perfect Helmholtz coils with comparable geometries.

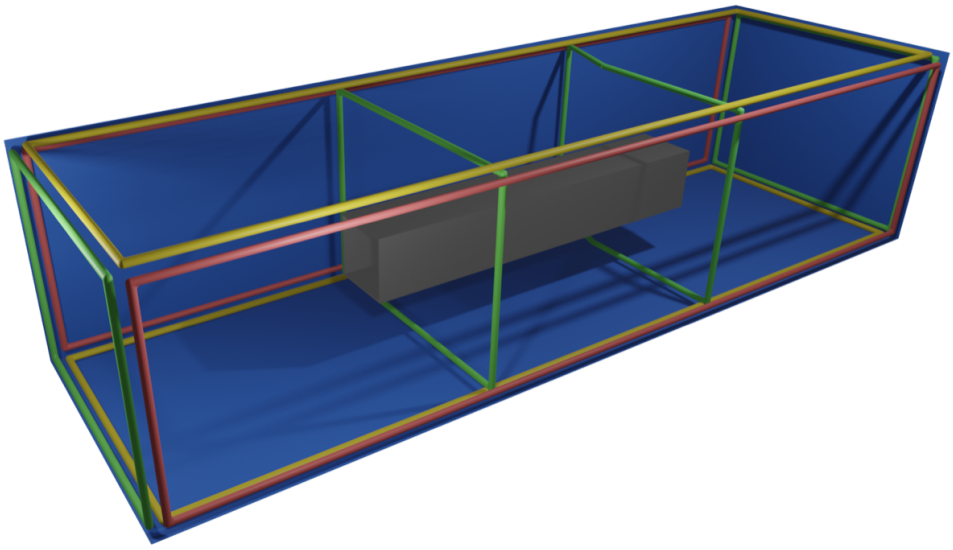

Figure 3.7.: A rendered sketch of the simplified room coil arrangement scheme. The longitudinal (green), horizontal (red) and vertical (yellow) coil pairs can be seen surrounding the MuMetal shielding. The longitudinal coil on the further end (upstream end) has a buckling in it, due to the window configuration in the laboratory. This buckling is shown here as well.

3.3 | Mapper

To measure magnetic fields within the set-up the so called *mapper* has been used. The mapper is a wagon-like device that essentially carries five fluxgate magnetometers (*Stefan Mayer* FLC3-70) and can be remotely controlled to move along rails in the centre scaffold-part. Besides the fluxgates, the mapper also carries an Intel NUC to which the fluxgate data is transmitted via a National Instruments DAQ device (*USB-6212, NI Multifunction I/O DAQ*) as well as two LiPo batteries to supply the devices with power. The whole wagon is attached to two lashing straps that are wound around reels such that the mapper can be moved through the set-up by a remotely controllable step motor (*Trinamic Motion Control QSH6018-86-28-310*).

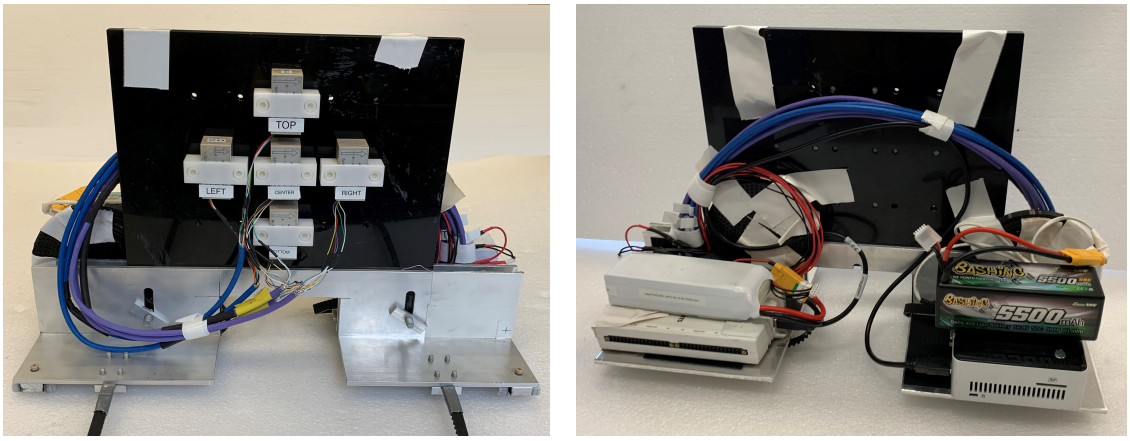

(a) Frontside of the mapper

(b) Backside of the mapper

Figure 3.8.: On the frontside (a) of the mapper we can see the five fluxgates in their cross-shaped arrangement. The fluxgates are connected to the NI DAQ device on the backside (b), via the purple patch cables. On top of the DAQ lies one of the two LiPO batteries that powers the DAQ. On the right-hand side the INTEL NUC is installed with its own LiPo battery lying on top of it.

Fluxgate Arrangement

The five FLC3-70 fluxgate magnetometers are mounted on a plastic plate as shown in figure 3.8a. All five of them are oriented in the same direction and labelled with *Top*, *Bottom*, *Left*, *Right* and *Centre*, according to their respective position on the plate. The centre fluxgate is positioned so that its own centre is roughly aligned on the central axis of the aluminium scaffold and its indicated coordinate system corresponds to the beamline coordinate system. The central fluxgate is horizontally centred, however, vertically, its centre lies 7.5 mm below the central axis of the beamline area. Between the centre of the central fluxgate and the centres of the surrounding fluxgates there is a 6 cm distance.

Remaining Parts; DAQ, PC, Batteries

The five fluxgates are connected to a *National Instruments* DAQ device (USB-6212). For all three axis the fluxgates put out a voltage that is proportional to the applied magnetic field component. The NI DAQ device measures the difference between the output axis-signal and the so called reference signal $OUT\text{-}$, which is provided by the fluxgates and is equal to half the operating voltage, i.e. $OUT\text{-} = \frac{V_+ - V_-}{2}$, where V_+ is the supply voltage of 15V and V_- is the supply ground. With five fluxgates we have 16 assigned channels that are measured simultaneously with the DAQ in *Referenced Single Ended* (RSE) Terminal Configuration, 5×3 axis signals on `AI0 - AI14` and the ground reference on `AI15/AI`

GND. An externally placed battery (*SWAYTRONIC 5200mAh 14.8V 4S LiPo*) delivers the necessary supply voltage for the fluxgates. Via USB connection the NI DAQ is connected to an Intel NUC (*NUC5CPYH*) on which the DAQ software runs. The Intel NUC is powered by its own LiPo battery (*Gens Ace 5500mAh 14.8V 50C 4S1P Lipo*). All these devices are mounted on the mapper wagon as well, as shown in figure 3.8. Furthermore, for certain measurements, two LiPo-checkers (*Yuki Model 700227*) were connected to the batteries, which allowed for a monitoring of the battery level.

Moving the Mapper through the Set-Up

With two tensioning belts that are attached to the mapper and strained to rolling axes on both ends of the set-up, the mapper can be moved through the whole set-up by a motor that rotates one of the two axes. The step motor can turn the axis in steps of 1.8°. The starting and end point of a measurement series is defined by two physical switches that are installed at two defined positions on the mapper's tracks. The mapper's position is measured with a laser distance measuring device (*UNI-T UT390B*) that is attached to one of the two rails the mapper rolls on. The laser measuring device measures the relative distance from the laser itself to a defined spot on the mapper wagon (indicated by a cross on the bottom right in figure 3.8a). By knowing the exact position of the laser device within the aluminium scaffold itself, the mapper's position can be determined from the laser distance measurements.

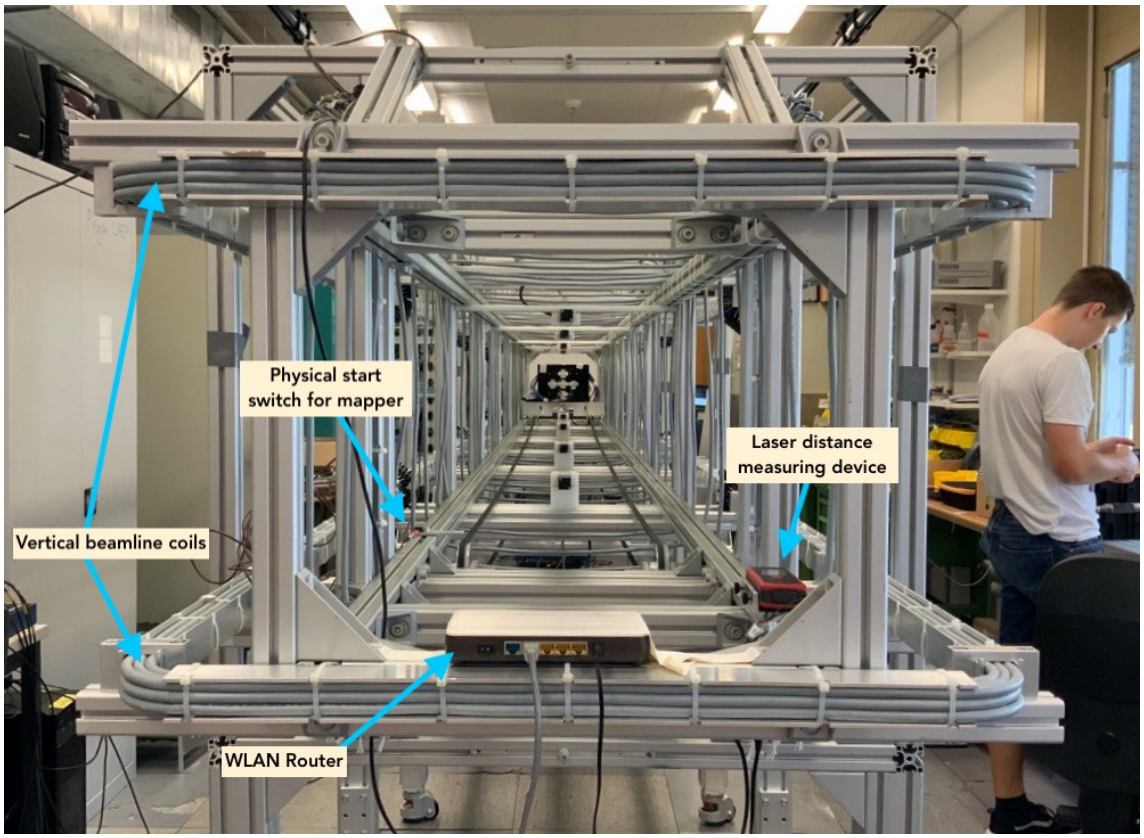

Figure 3.9.: The unshielded experimental set-up as seen from the upstream end. Here, the mapper is in the middle of a magnetic field map, moving to the downstream end of the beamline. The laser distance measuring device and the physical start/stop end switch can be seen as indicated, as well as the WLAN router in the lower middle. Furthermore, the main beamline coils pair, generating the vertical magnetic field, is indicated in the picture.

Communication between the Devices

The PC running the LabVIEW software is directly connected to the roomcoil's power supply and its waveform generator, to the laser distance measuring device, to the mapper's motor and to a WLAN router which is mounted at the upstream end of the aluminium scaffold, as shown in figure 3.9. The router allows for a wireless connection between the LabVIEW PC and the mapper's Intel NUC. For each measurement the LabVIEW PC transmits the relevant measurement information to the NUC, such as the start signal for each measurement and the smapling rate with which the measurement should be taken. Furthermore, also the distance measured by the laser device is transmitted to the NUC, on which it is the saved locally together with the recorded raw fluxgate data.

3.3.1 | The Controlling LabVIEW VI

The measurements are performed and controlled through a LabVIEW VI that controls all the measuring devices and delivers all the relevant data not measured on the mapper itself to the mapper's NUC where it is saved it locally. For a set of measurements a fluxgate sampling rate (i.e. the read out frequency of the NI DAQ channels) as well as the total amount of samples per stop is determined in the VI. This then also determines the measurement time per stop of the mapper. For each stop, a data-file is generated that contains the sample rate and the number of the total amount of samples in its header, while the measured voltages for the 16 DAQ readout channels (`AI0 - AI15`) are saved in the data file together with the measured position of the mapper. This measured position is the average of two measurements taken by the laser position meter during one mapper stop. Furthermore, the VI controls the motor that steers the mapper, where the amount of motor-steps that are taken between two mapper stops can be adjusted within the VI. The starting point and the end point of a measurement series are given by two physical switches that are at fixed positions on the mapper's tracks. The starting point switch can be seen in figure 3.9. Once the mapper triggers these switches they send a stop signal to the mapper's motor, which the reports this event to the controlling VI. This allows the LabVIEW VI to determine if the mapper is ready to start a new measurement cycle or if the mapper has reached the end of said cycle.
For the AC magnetic field measurements the VI also controls the frequency of the magnetic field generated by the room coils, by remotely controlling a waveform generator (*Keysight 33500B Series Waveform Generator*) that then controls the roomcoils' power supply. A list of frequencies can be passed to the VI, so that a new measurement series is automatically started once the mapper reaches its end point for a measurement series for a given field frequency. The field's frequency per series is saved within the data file name.
For a measurement the following parameters can be controlled and set within the VI control software:

- Sample rate of fluxgate measurements
- Number of samples to take during one measurement step
- Distance between mapper stops during a measurement series
- Number of Laser distance meter samples to average over per mapper stop
- Current strength to power room coils with for static field measurements
- Amplitude and frequency of AC current through room coils
- Name and storage path of generated data file on the mapper's NUC

Together, the sample rate and the number of samples to take during one mapper stop determine the measuring duration stop. While measuring low frequency AC fields one has to take into account to choose measuring times long enough to record at least half of the

desired AC signal in order for it to be analysable properly without a large uncertainty. This is discussed in more detail in [30].

3.4 | Passive Magnetic Shielding

To reduce systematic effects in the BeamEDM experiment's measurements, we want to have a magnetic field along the beam line which is as homogeneous as possible (see section 1.1). Therefore, we need to reduce externally generated magnetic fields, i.e. fields that are not produced by our main beamline coils, as much as possible. This is done with a passive magnetic shielding which is installed on the outside of the aluminium scaffold. We install two types of passive magnetic shields, a primary two-layer MuMetal shielding and a secondary RF shielding made from aluminium. Only the MuMetal's shielding efficiency is characterised within this thesis.

3.4.1 | MuMetal Shielding

To shield the interior of the aluminium scaffold from static magnetic fields and low-frequency AC fields we make use of a passive MuMetal shielding. MuMetal is an alloy made from nickel, iron, copper and molybdenum [31]. It has a very high relative (magnetic) permeability μ in the range of $50'000 - 800'000$ [32]. Therefore it is an excellent material for magnetic shielding for static and low-frequency magnetic fields (see section 2.2).
The shielding, manufactured by *Magnetic Shields Ltd*, is made from 24 MuMetal shielding panels. Each panel consists of two layers of MuMetal (1.5785 mm thickness), separated by 19 mm of nonconducting insulator material made out of PVC foam plates. Each regular panel is quadratic with a side length of 998 mm. Non-regular panels, i.e. the panels designed for the bottom side of the shielding, feature holes in it designated for the scaffolds feet to fit through. The shielding panels are directly mounted onto the aluminium scaffold using aluminium bolts. A rendered image of the full shielding without the scaffold can be seen in figure 3.10. The shielding covers the whole side length of the aluminium scaffold. For each modular cube of the scaffold there are four quadratic panels that are attached to the outer sides. To have a gap-less two layer shielding along the complete beam line, the gaps between two panels and at the cubes' corners are covered by additional MuMetal pieces, on the inside and on the outside.
There are five panels that feature feedthroughs for either the BeamEDM's high voltage (HV) connection or for the vacuum pump connection (not shown in the rendered shielding image). With a diameter of 25 cm the single HV feedthrough is larger than the four 10 cm diameter vacuum pump feedthroughs. For all measurements except the ones from section 4.3.3, the feedthrough holes have been covered with two MuMetal lids.

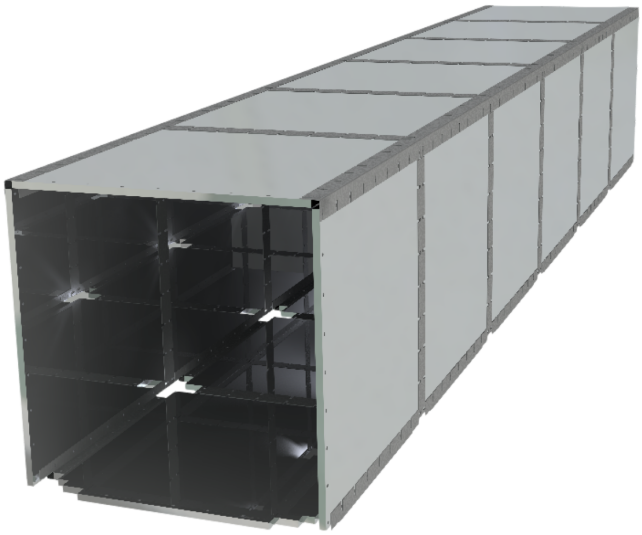

Figure 3.10.: A rendered image of the full MuMetal shielding without the aluminium scaffold. The six two-layer plates on each side are connected with additional MuMetal plates that cover the gaps. Corner-pieces bridge the gaps at the corners between two shielding plates, on the inside and on the outside. The bottom panels feature certain cut-outs that allow for the aluminium feet to be installed. These holes are not covered by MuMetal .

3.4.2 | Feedthrough Tubes

For the BeamEDM experiment, several lateral accesses to the beamline are needed in order to have access to the vacuum pipes and to deliver a the high-voltage, once the MuMetal shielding is installed. Therefore, as previously mentioned, five MuMetal panels have opening caps, where single layer MuMetal feedthrough tubes can be attached. A render of the shielding where all feedthrough tubes are installed is shown in figure 3.11. The large feedthrough tube has an outer diameter of 25 cm and a length of 75 cm, whereas the smaller feedthrough tubes have outer diameters of 10 cm and lengths of 30 cm. Their centres are located at exactly 25 mm distance from their respective near cube edge, horizontally. Vertically, they are centred within their respective shielding panel. The impact of the feedthrough tubes on the shielding effectiveness for static magnetic fields is documented in section 4.3.3.

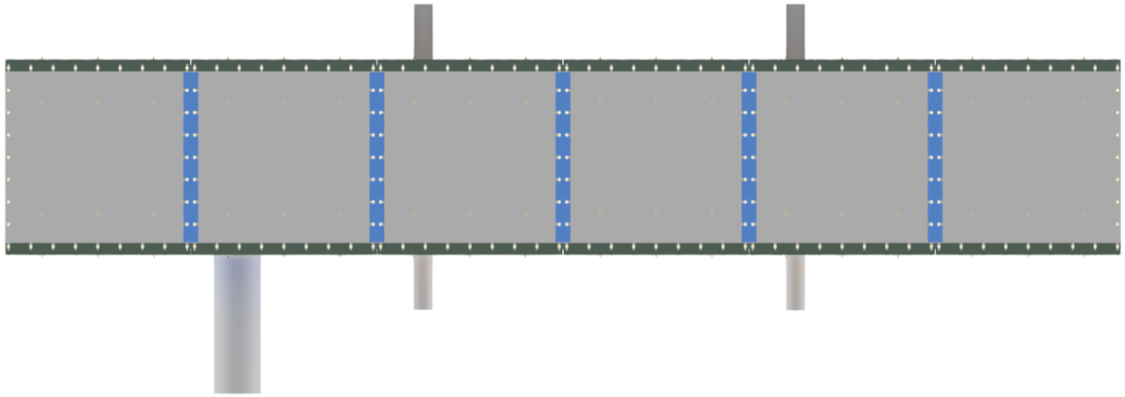

Figure 3.11.: A top-view render of the shielding, where all five feedthrough tubes are installed. The small vacuum pump feedthroughs are installed directly opposite to each other. Every feedthrough tube is vertically centred on their respective shielding plate. The left-hand side represents the upstream end, the right-hand side the downstream end.

3.4.3 | Aluminium RF Shielding

As apparent in figure 3.5a, the vertical beamline coil pair protrudes out of the MuMetal shielding. This makes it vulnerable for picking up external AC fields which then induce unwanted signals into the coil which then also transmit into the shielded beamline area. To reduce this effect, additional aluminium shielding was installed at both ends of the beam line. Since the aluminium RF shielding is not of importance for the static field measurements on which this thesis lays focus on, the RF shielding set-up is only described for the sake of completeness and will not be discussed further in detail. The documentation of the according measurements can be found in [30].
The aluminium plates which make up the RF shielding, coloured in yellow in figure 3.12, are cut out from raw aluminium plates of 4 mm thickness. They are directly mounted onto the respective ending pieces of the aluminium scaffold and electrically connected to each other using aluminium tape.

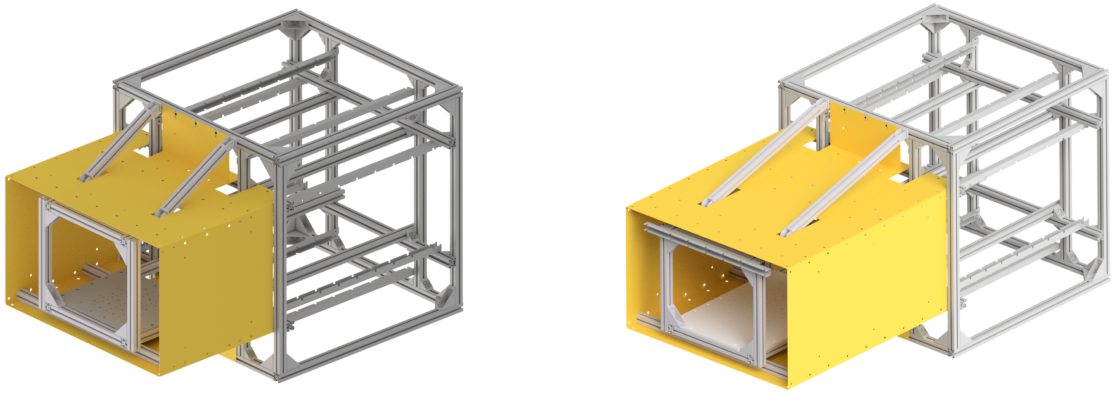

(a) The upstream end's RF shielding

(b) The downstream end's RF shielding

Figure 3.12.: Rendered pictures of both end pieces with their respective aluminium RF shieldings. The RF shielding's components are coloured in yellow.

3.5 | Room Geometry Kryolab

All the preliminary measurements of the shielding listed in this thesis have been conducted in the same room (Kryolab, ExWi Bern). A schematic drawing of the room including the positioning of the whole set-up within the room and the position of the room coils can be seen in figure 3.13.

Additionally, there are potentially magnetic structures present within the laboratory that could have an effect on the measurements. As shown in picture 3.14 there is a large ventilation shaft, a crane rail and several gas pipelines installed in the proximity of the aluminium scaffold. The magnetic behaviour of these parts has not been investigated.

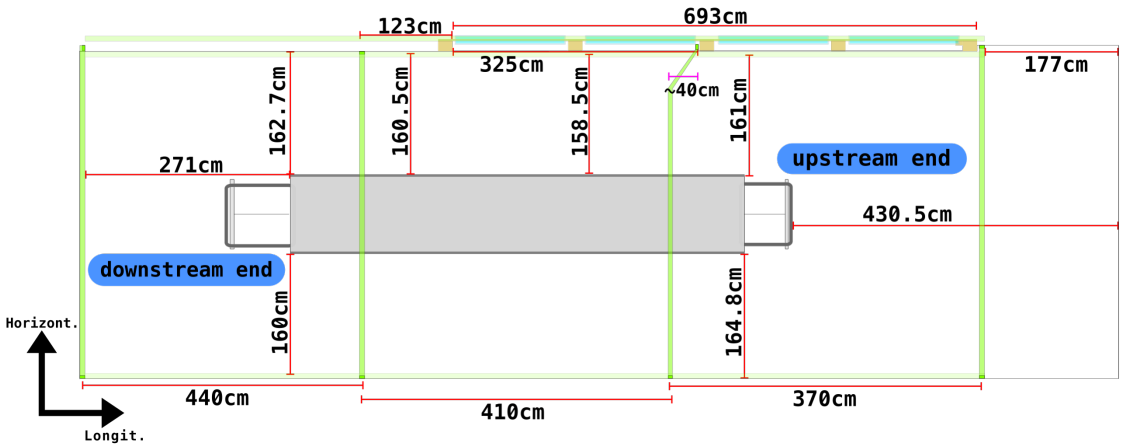

Figure 3.13.: A simple top view sketch of the room dimensions of the laboratory at the University of Bern. Indicated are some relevant distances that situate the experimental set-up within the laboratory. The room coils are indicated in green. The room height measures 3.7 m.

Figure 3.14.: Potentially magnetic parts within the laboratory that are installed on the ceiling, such as the ventilation shaft or the crane rail. The picture is taken from the upstream ending's side.

4 | Measurements and Simulations

In this chapter, the results from the static magnetic field measurements are presented. First, the results from the measurements with the unshielded set-up, i.e. the raw aluminium scaffold without MuMetal shielding installed, are shown. In a second part, the results from the measurements conducted with the installed MuMetal shielding are presented. The results from both measurement series are then compared with each other in order to characterise the MuMetal's shielding capacity in terms of shielding factors.
For both, the unshielded and the shielded case, an example of raw data and its step-by-step processing is displayed in order to get an idea of how the shown magnetic field maps along the beamline are actually obtained. Afterwards, for each set-up, magnetic field maps are demonstrated for all three directions of magnetic fields generated by the room coils.
Furthermore, also the field generated by the main beamline coil (vertical field direction) is measured in both, the shielded as well as the unshielded case. The results are compared to see how the presence of the shielding impacts the generated magnetic field within the beamline area. For the shielded scenario we then investigate whether the magnetic field meets the demands we have for the BeamEDM experiment to take place in regards of field homogeneity and occurring field gradients.

For coil generated static field measurements the background field of each respective measurement has been subtracted by measuring both field polarities per coil and calculating

$$B_{\text{measurement}} = \frac{|(B_+ + B_{\text{bckg}}) - (B_- + B_{\text{bckg}})|}{2} = \frac{|B_+ - B_-|}{2}, \tag{4.1}$$

where B_+ and B_- are the individuals fields generated by the coils for both polarities and B_{bckg} is the present background field. The shown measurements have been conducted with a constant motor step size of about 5'000 which translates into an approximate 5 cm distance between the field measurements. For all of the subsequently shown plots the measurement points are linearly interpolated. Each measurement point results from a 2 second measurement with a 10 kHz sample rate. In all plots of mapped data where the x-axis is labelled with '*Distance along the Beamline* $[m]$', the zero position of the mapper respective to the graph's x-axis is at the upstream end of the beamline.

4.1 | Measurements of Unshielded Magnetic DC Fields

The measurements in this section refer to measurements conducted with the unshielded set-up, i.e. neither MuMetal nor aluminium RF shielding was installed during the measurements.

4.1.1 | From Raw Data to Magnetic Field Maps

With a fluxgate sample rate of 10 kHz and a measurement duration of 2 seconds per mapper stop, the magnetic field along the complete beamline is measured in 92 discrete steps. For the measurement taken at the centre of the beamline, the raw data recorded by the centre fluxgate is shown in figure 4.1, where only a constant offset value has been subtracted from that has been determined for every fluxgate in use (see Appendix A).

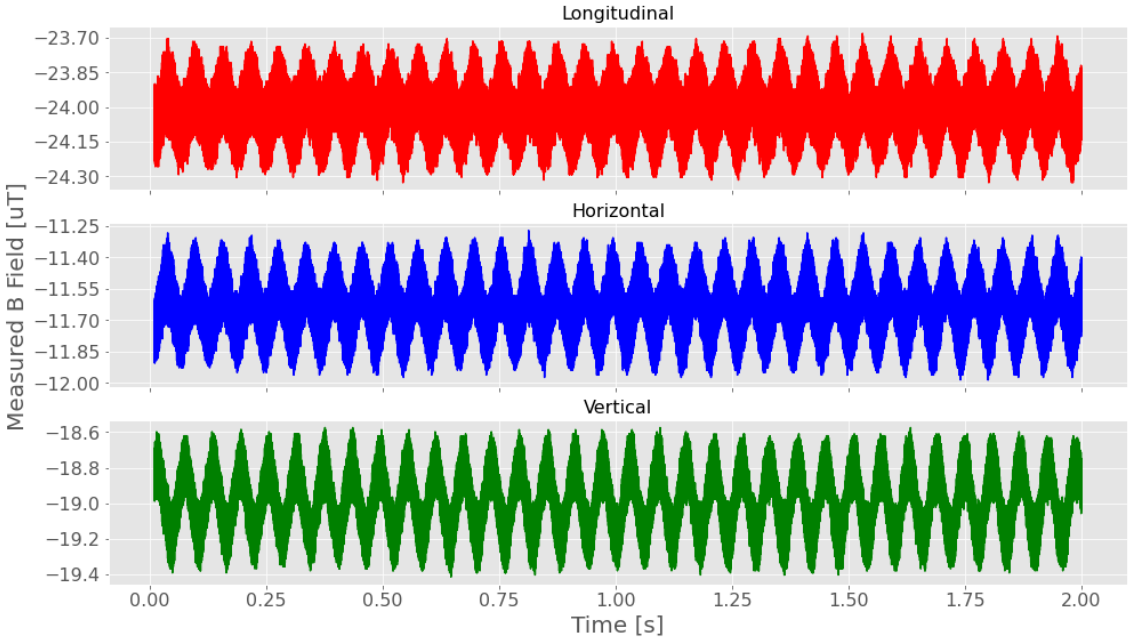

Figure 4.1.: The 20'000 data points per axis recorded by the centre fluxgate during the 2 second measurement at the central position along the beamline (corresponding to $x = 3$m on figures 4.4 - 4.6.) away from the beamline start. The only conversion that has been made is to multiply the originally stored voltages with the respective conversion factor of the FLC3-70 fluxgate in order to plot the measured magnetic field. The railway power line's 16.7 Hz background signal is clearly visible in the signal.

It can be readily seen that the strongest AC signal contribution is coming from a ∼17 Hz signal. This is an expected noise signal at the ExWi laboratories, as the SBB's high voltage railway electrification system is operated at exactly 16.7 Hz. Besides that, the signal is very noisy and is smeared out by a high frequency signal component with an amplitude of approximately 150 nT. This effect originates in aliased noise of the fluxgate excitation frequency and is not intrinsically physical. The effect is discussed in detail in [30]. To get rid of this high frequency sinusoidal noise, a digital fifth order low pass Butterworth filter with a cutoff frequency of $f_c = 1'000$ Hz is applied to the data, which effectively removes the aliased noise. The filtered signal is shown in figure 4.2.
The further contributing frequencies are then made apparent by Fourier transforming the signal using `Numpy`'s one-dimensional n-point discrete Fourier transformation for real valued arrays (*numpy.fft.rfft*). The obtained Fourier coefficients can be converted to the respective magnetic field strength's of the corresponding field frequencies and are shown in figure 4.3. To gain a higher resolution on the Fourier frequency-spectrum, the 2 second signal is zero-padded to a 10 second signal, so that we are able to resolve frequencies in steps of 0.1 Hz. As a consequence, wavey structures show up around the main peaks in the Fourier transform, which are not directly physical but only artefacts of the zero-padding signal processing [33].

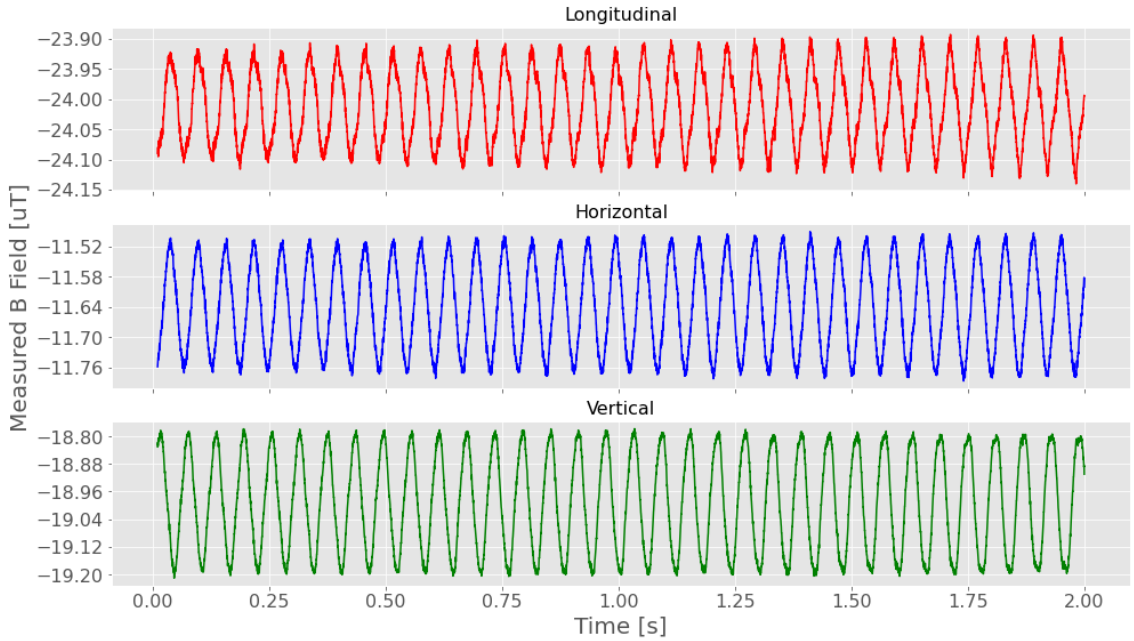

Figure 4.2.: The recorded data from figure 4.1 with a digital fifth order low pass Butterworth filter (cutoff frequency at 1 kHz) applied to it, in order to remove aliased noise of the fluxgate excitation frequency.

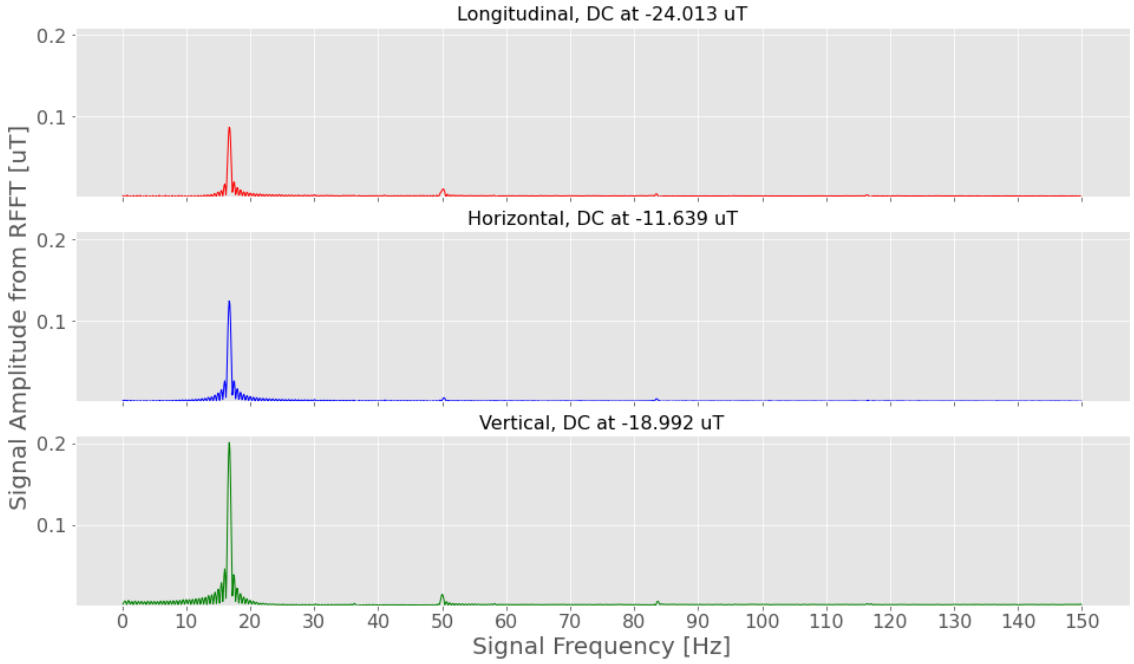

Figure 4.3.: The Fourier transformed signal which shows the main signal contributions at 16.7 Hz and 50 Hz. The rippled envelopes around the peaks are artefacts of zero-padding. Furthermore, the dominant harmonics of the main frequency show up at odd multiplicatives of its frequency, i.e. at 83.5 Hz the 5th order harmonic is visible. For a higher visibility of the mentioned Fourier components the static field component ($f = 0$ Hz) has been excluded from the plot and its value is indicated in the corresponding plot title.

As expected, besides the railway power grid frequency, the usual 50 Hz utility frequency is visible as the second main contribution in figure 4.3. The contribution to the 50 Hz peak is twofold, however, as the 3rd order harmonic from the railway frequency also contributes to the peak ($3 \times 16.7\,\text{Hz} \approx 50\,\text{Hz}$). The statistical error of the measured amplitudes is

around ±5 nT, as this is the standard deviation of the Gaussian distributed data points around the mean value of a fully shielded, noise-only signal.
The DC component of the measured field can be simply calculated as the mean value of the 2 second measurement. It is then also represented as the 0 Hz Fourier coefficient in the Fourier transformed signal in figure 4.3. For reasons of visibility, the DC component is excluded from the plot, its value is mentioned above the corresponding plot, however.
The DC values of these measurements are then used to create the magnetic field plots that are shown in the upcoming sections. A full beamline measurement consists out of approximately 97 single 2 second measurements, which are then interpolated using a cubic spline interpolation method, to create the field plots along the full beamline. The same can be done for AC magnetic field maps, where the value of the converted Fourier coefficient is plotted and interpolated along the beamline for a desired frequency (see [30] for AC field maps). The interpolation of the data points along the beamline is necessary for the subsequent determination of the shielding factors. This is because the mapper doesn't always measure at the exact same spots during separate measurement runs. As for the determination of the shielding factor we need to compare the magnetic field measured at the same location in the shielded and unshielded set-up, we interpolate the data points, such that magnetic field values of the exact same locations can be compared.

4.1.2 | Background Field

A background field is measured within the set-up. The main contribution to the magnetic background field is expected to come from earth's magnetic field itself. According to [34], the earth's magnetic field at the location of the laboratory was approximately at $\vec{B}_{\text{earth}} = 21.79\mu\text{T} \cdot \vec{e}_{\text{north}} + 0.97\mu\text{T} \cdot \vec{e}_{\text{east}} + 42.67\mu\text{T} \cdot \vec{e}_{\text{vertical}}$. Translated into the Cartesian coordinate system used in this thesis the magnetic background from earth's magnetic field is expected to be

$$\vec{B}_{\text{earth}} = \begin{pmatrix} B_{\text{longit.}} \\ B_{\text{horiz.}} \\ B_{\text{vert.}} \end{pmatrix} = \begin{pmatrix} -19.33\ \mu\text{T} \\ -10.09\ \mu\text{T} \\ -42.67\ \mu\text{T} \end{pmatrix}. \tag{4.2}$$

This field is not expected to change much, neither over the duration of a measurement nor over the measured distance. A background measurement was conducted with a mapper step size of 6cm, resulting in 94 equidistant measurements along the beamline. At each position the measurement lasted 2 seconds with a fluxgate sample rate of 10 kHz. For each component of the magnetic background field, i.e. the longitudinal, horizontal and vertical component, a plot is shown where the individual fluxgate measurements are plotted along the distance of the beamline, where the x-axis' origin refers to the outer edge of the scaffold item profile on the chopper end (upstream end) of the set-up and 6 m is on the opposite outer edge of the scaffold.

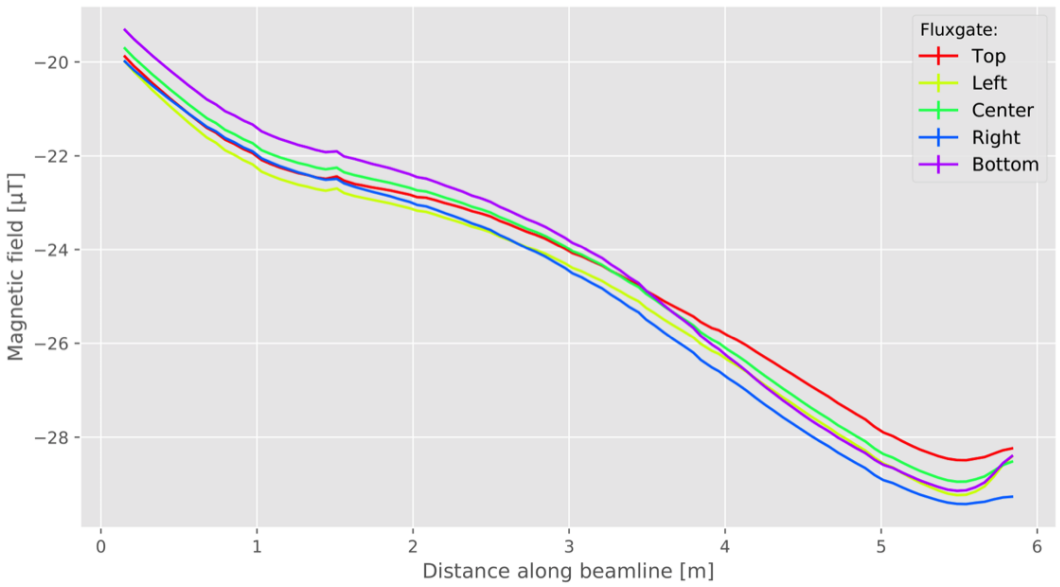

Figure 4.4.: Longitudinal component of the measured background field with the unshielded set-up.

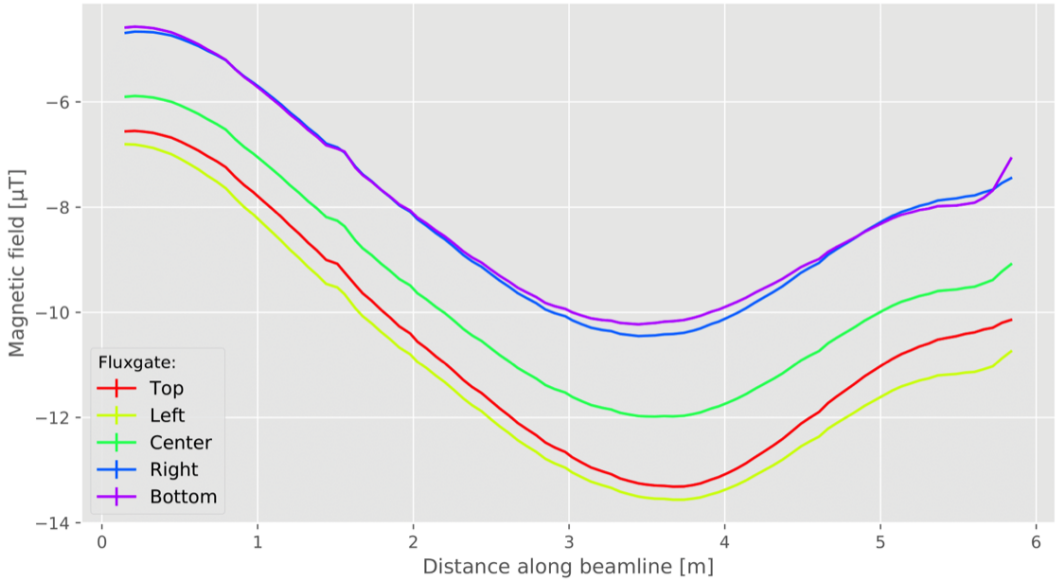

Figure 4.5.: Horizontal component of the measured background field with the unshielded set-up.

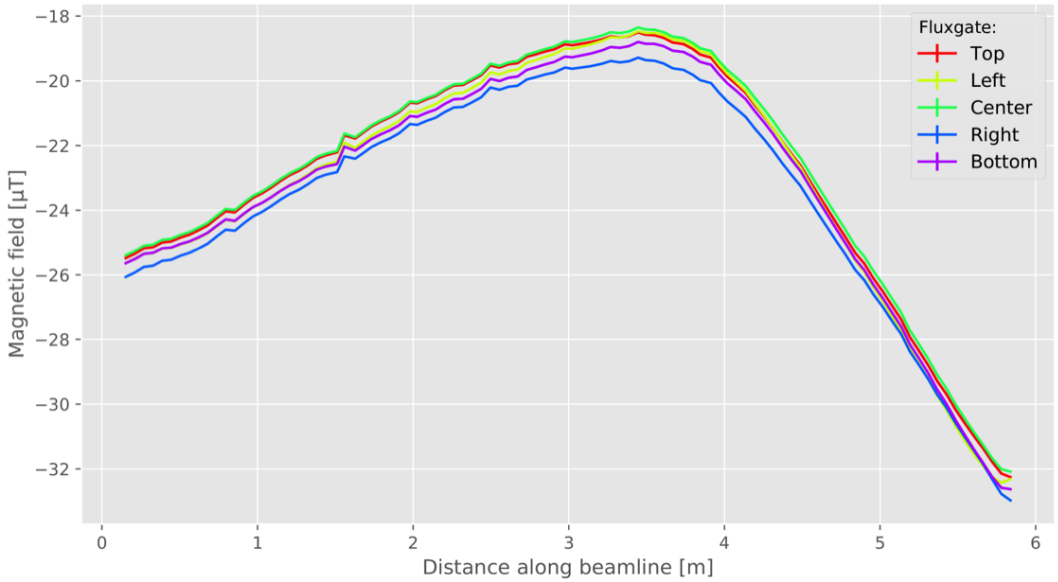

Figure 4.6.: Vertical component of the measured background field with the unshielded set-up.

For each direction an average between the five single fluxgate measurements is calculated. In figure 4.7 the background averages are then gathered in a single plot.

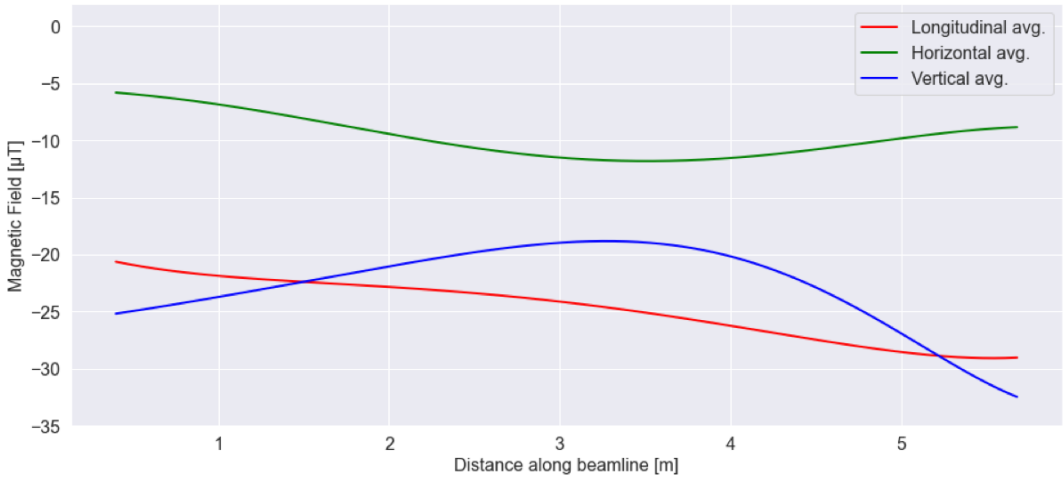

Figure 4.7.: Background field measurements in all three directions averaged over all five fluxgates.

The measured background field in the horizontal direction roughly corresponds to the expected value calculated in equation (4.2), whereas the longitudinal and the vertical component deviate from the expected earth's magnetic field background. Furthermore, for each field component we see the presence of a field gradient along the beamline axis, which surely is not expected to be part of earth's magnetic field. Additionally, in figures 4.4 - 4.6 we see that the fluxgates themselves already measure different magnetic fields during the same sweep.
The small order gradients between the fluxgates most likely stem from the residual magnetisation of the mapper components themselves, such as the DAQ device, the Intel NUC and the two batteries. The larger change in the measured fields along the beamline axis most likely originates in the presence of magnetised surrounding objects within the lab, such as the ventilation shaft or constructional steelwork.

4.1.3 | Room Coil Generated Static Fields

Using the room coils described in section 3.2.2, magnetic fields have been generated in each direction separately. For each direction a plot of the measured field in the respective direction is shown hereafter. Each plot shows the respective magnetic field component for the direction where the external field has been applied, measured in µT along the full movement capacity of the mapper by each individual fluxgate on the mapper. For all three measurements a fluxgate sample rate of 10 kHz was used and a measurement duration of 2 seconds per mapper stop was set.

Figure 4.8 shows the longitudinal magnetic field component measured for a field generated by the longitudinal room coils powered with a current of 9 A. Two maxima can be seen, whose positions correspond exactly to the positions of the two central longitudinal room coil loops. An average magnetic field of 14.3 ± 2.34 µT is reached along the beamline.

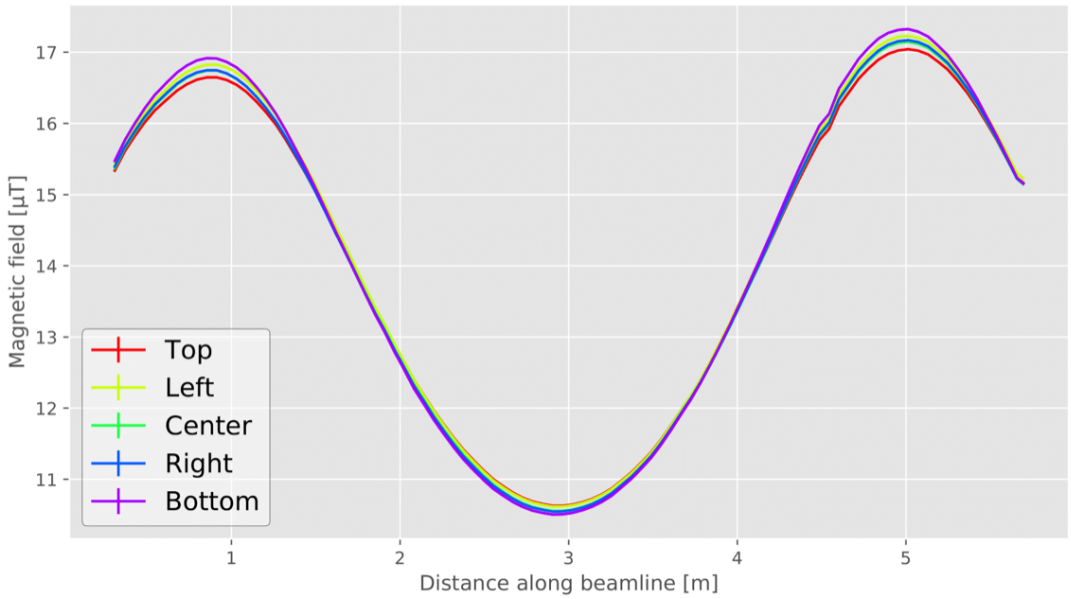

Figure 4.8.: Field generated with 9 A powered longitudinal room coils, measured in the unshielded set-up.

For the horizontal field, shown in figure 4.9, the coils have been powered with 10 A. The measured field is more constant compared to the longitudinal field and only varies around 0.7 µT along the beamline. An average field of 10.3 ± 0.3 µT is measured along the beamline.

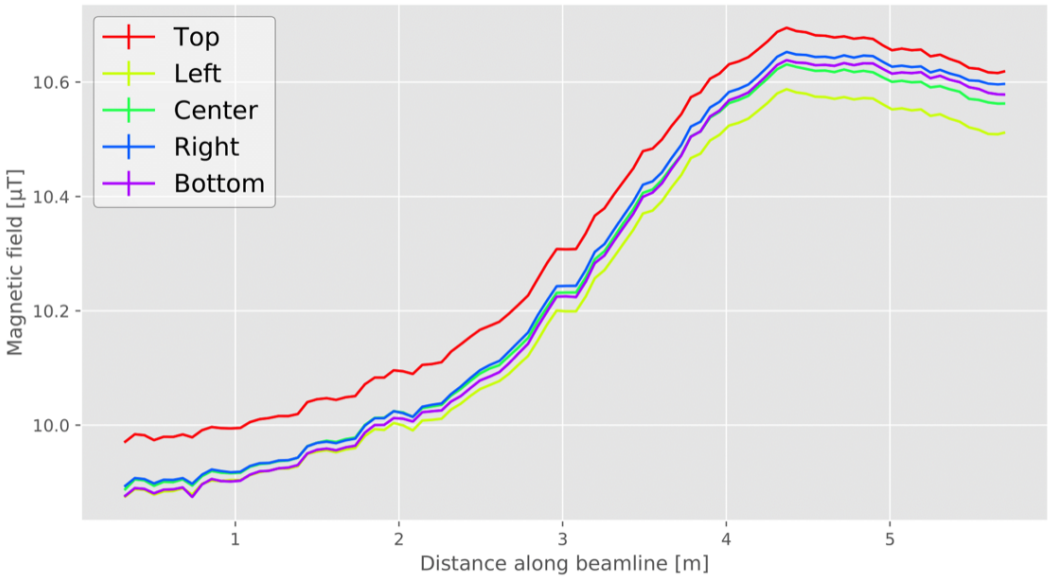

Figure 4.9.: Field generated with 10 A powered horizontal room coils, measured in the unshielded set-up.

Last but not least, figure 4.10 shows the field that is generated by the vertical room coils powered with 10 A. It is of comparable homogeneity as the horizontal field and n average field of 13.2 ± 0.2 µT is measured along the beamline.

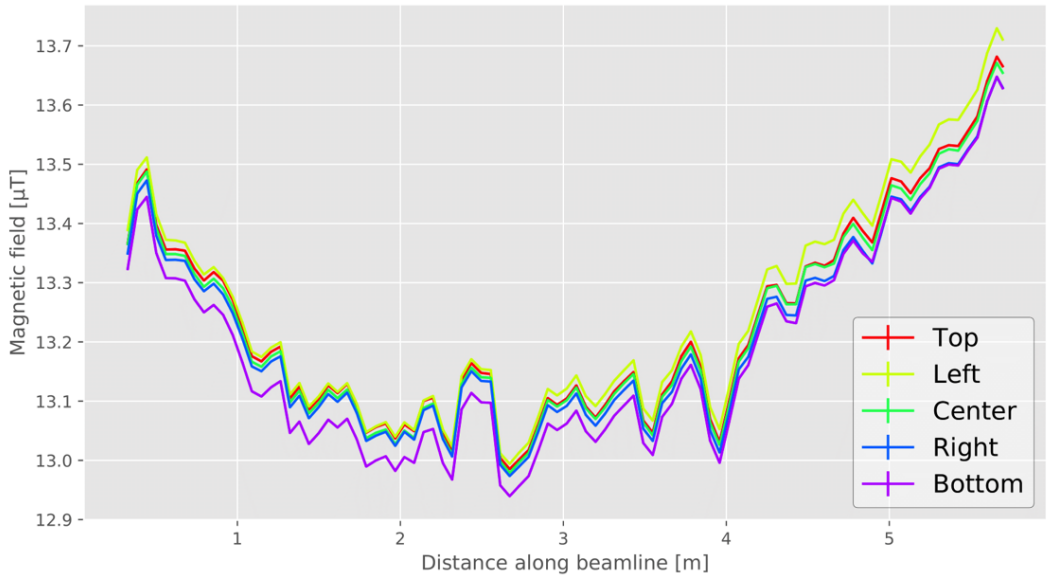

Figure 4.10.: Field generated with 10 A powered vertical room coils, measured in the unshielded set-up.

To compare the three measurements, we gather them in a single plot where for each direction the average of the five fluxgate's measured fields has been calculated and the magnetic field is normalised with respect to the applied current with which each room coil has been powered. Additionally, with dashed lines, the theoretically expected field generated by comparable coil arrangements is plotted, which is calculated with the procedure explained in section 2.1.

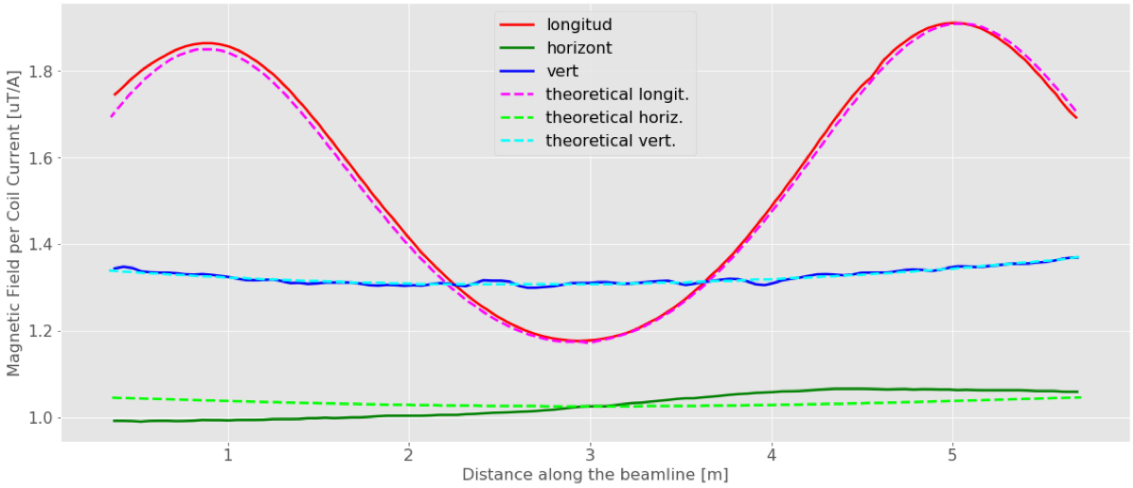

Figure 4.11.: For each field direction the averaged measured field component per applied Ampere in the respective direction is shown and compared to a theoretical value that is calculated for Helmholtz coil pairs of comparable dimensions.

For the longitudinal field we see that the measurements and the theory match quite well. The peak on the left side of the plot is slightly underestimated, which presumably comes from the fact that the coil loop at that position has a slight bump in it, as shown in figure 3.7. For the horizontal field the average values of the measurement and the prediction agree. The asymmetric field drift over the measured distance is not predicted by the theory, though. This could possibly be caused by surrounding magnetic material, such as (indefinite) cabinet contents which are accumulated near the downstream end of the set-up (apparent in figure 3.14). For the vertical direction, again, the average of the predicted and measured fields agree quite well. Compared to the other two measurements the vertically measured field is more jittery. The reason for this is not directly known, but it can be assumed that the background field, which is subtracted from the measurement, did not stay constant over the full period of measurements. A reasonable assumption is that simultaneously work was done in the laboratory featuring magnetic tools, which could explain the very irregular deviations over the measurement. However, this cannot be stated with certainty.

4.1.4 | Static Beamline Coil Fields Generated in the Unshielded Set-Up

The measurement for the main beamline coil generated static field (vertical direction) is performed in a similar way as the measurements for the room coils. Both polarities of the field, positive and negative, are measured separately. The background field can then be deducted by subtracting the measurements from each other (see equation (4.1)).
For the measurement of the main coil generated field all three components of the magnetic field are analysed separately and shown in the subsequent plots (figures 4.12, 4.13 and 4.14). For the measurements the coils have been powered by a steady 2 A DC current. For the plots the measured magnetic field has been normalised again with respect to the applied current, so that the measured magnetic field strength per applied current in µT/A is shown. The measured values for every single one of the five fluxgates is shown.
In figure 4.12 we see that for the main vertical component of the magnetic field, we reach a field strength of approximately 54 µT/A, averaged over all five fluxgates and over the full range of measurement. The generated field is roughly constant for the central 2 meters of the beamline (from 2 m to 4 m), whereas the field strength decreases near the ends of the coil. The generated field is not symmetric with respect to the 6 m long beamline zone, since the vertical beamline coil is not designed in a symmetrical way to it, as is shown in

figure 3.5a.

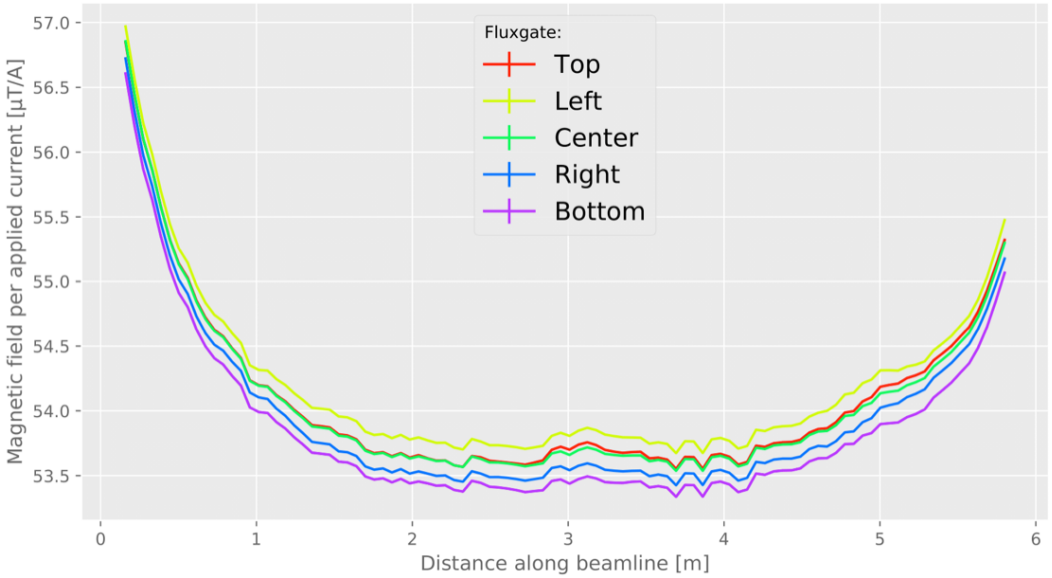

Figure 4.12.: The vertical component of the magnetic field per Ampere measured by the five fluxgates for the field generated by the vertical beamline coil powered by a steady 2 A DC current.

For the subordinate magnetic field components (longitudinal and horizontal direction) the measured magnetic field per current is much smaller, as expected, and on the order of approximately 1 µT/A:

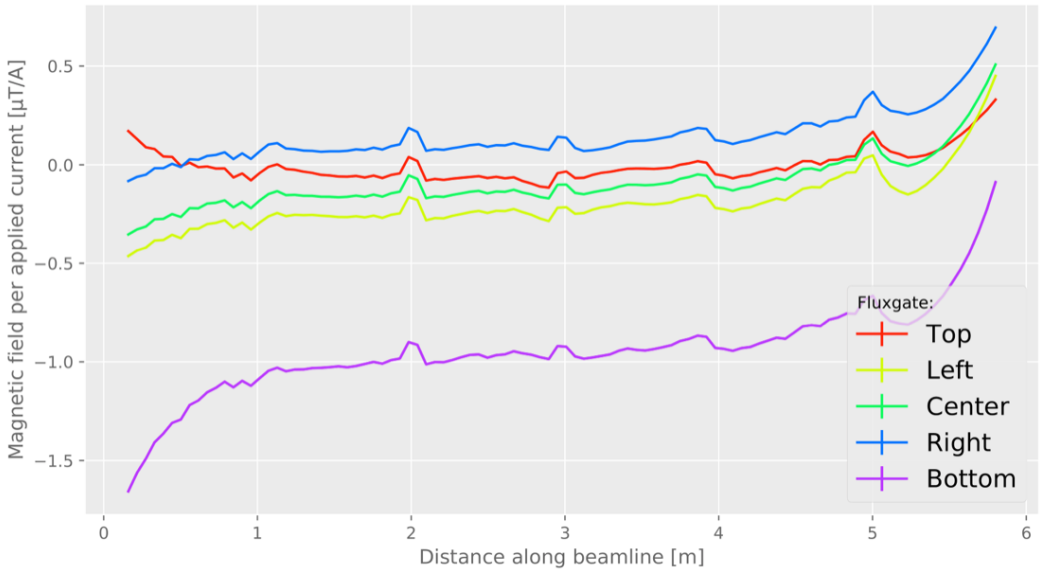

Figure 4.13.: The longitudinal component of the magnetic field per Ampere measured by the five fluxgates for the field generated by the vertical beamline coil powered by a steady 2 A DC current.

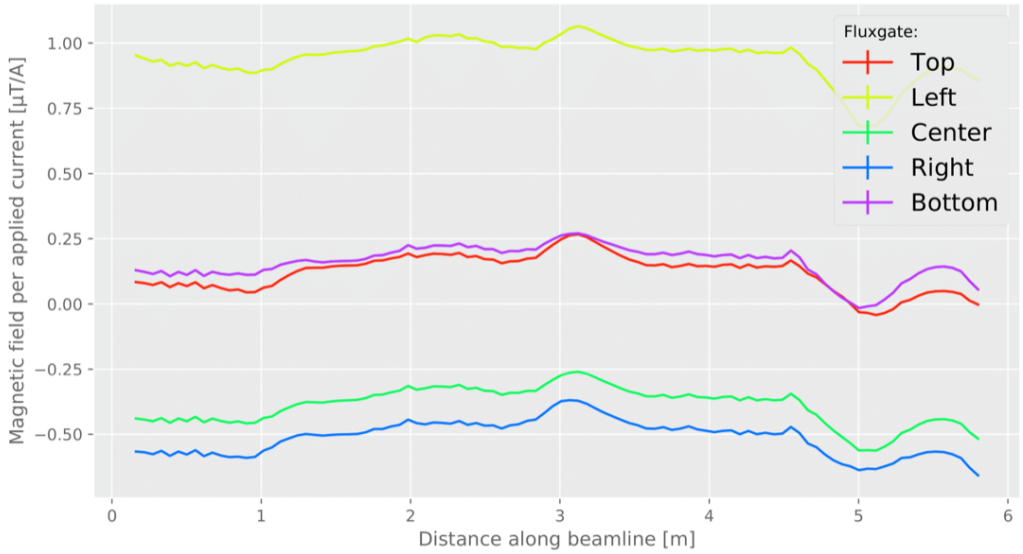

Figure 4.14.: The horizontal component of the magnetic field per Ampere measured by the five fluxgates for the field generated by the vertical beamline coil powered by a steady 2 A DC current.

4.2 | Measurements of Passively Shielded Magnetic DC Fields

The measurements from the last section have been repeated with the MuMetal shielding being installed along the full beamline. For the shown shielded measurements the plain MuMetal shielding was installed, i.e. there was no (aluminium) RF shield present and the HV feedthrough tubes are not installed, but the openings are closed with the respective MuMetal caps. The order of the shown measurements is the same as in the unshielded section. At first, the analysis of raw data is shown, where we look at the measured signal of the central fluxgate and its Fourier transform. This data analysis is followed by the measurements of the room coil generated static fields and the vertical magnetic field generated by the main beamline coil.

4.2.1 | Shielded Raw Background Data Analysis

Similar to the measurements in section 4.1.1 the (shielded) background field is determined, again, with a 10 kHz sample rate and a measurement duration of 2 seconds. The three measurements of the central fluxgate from the same mapper position, located at the centre of the beamline, are analysed. The raw signal is shown in figure 4.15, where, again, only the individual fluxgate's offset has been subtracted (see Appendix A). In comparison to the unshielded signal from figure 4.1 the 16.7 Hz sinusoidal component is not visible anymore and also no major regular signal component is readily discernible. Again, the raw signal is then filtered using the same low pass filter to remove aliased noise of the fluxgate's excitation frequency (as described in section 4.1.1). This is shown in figure 4.16.
Both signals, the filtered as well as the unfiltered, are basically noise-only. This is due to the fact that for frequencies around 20 Hz our MuMetal shielding reaches its maximum shielding capacity for alternating magnetic fields, with a shielding factor of about 200 longitudinally and around 700 horizontally and vertically (see [30]). The 16.7 Hz field amplitudes are all smaller than 200 nT in the unshielded case (figure 4.3), so we expect them to be indistinguishable from noise in the signals Fourier transform.

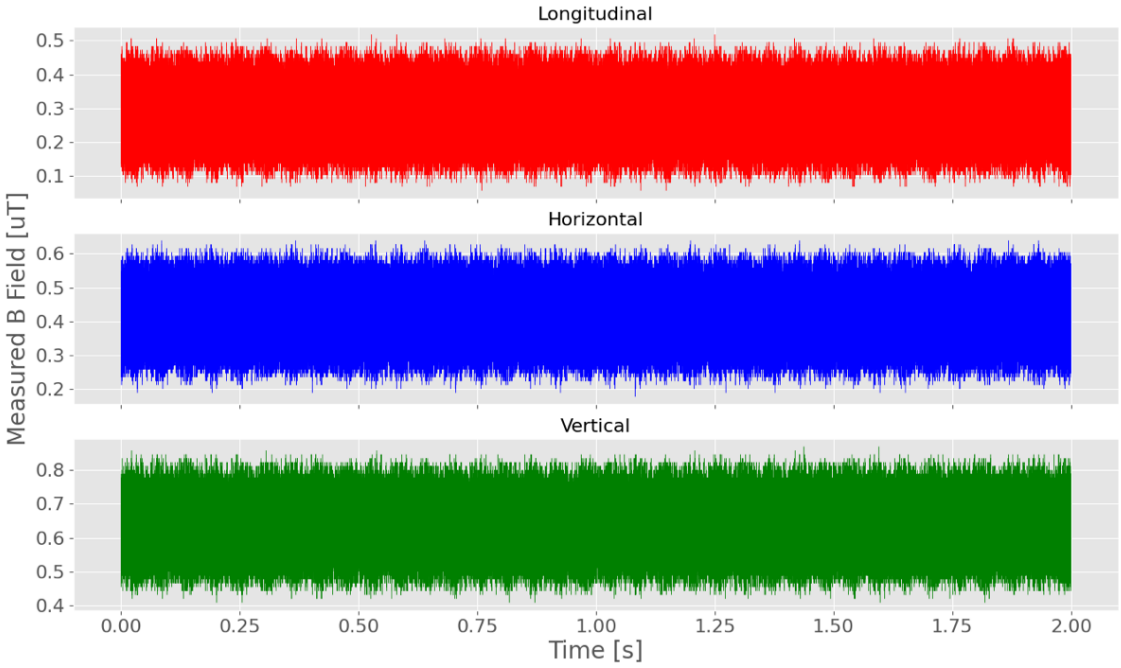

Figure 4.15.: The 20'000 data points per axis recorded by the centre fluxgate during the 2 second measurement at the shielded central position along the beamline. The fluxgates voltage signal is converted with the constant V/µT-conversion factor.

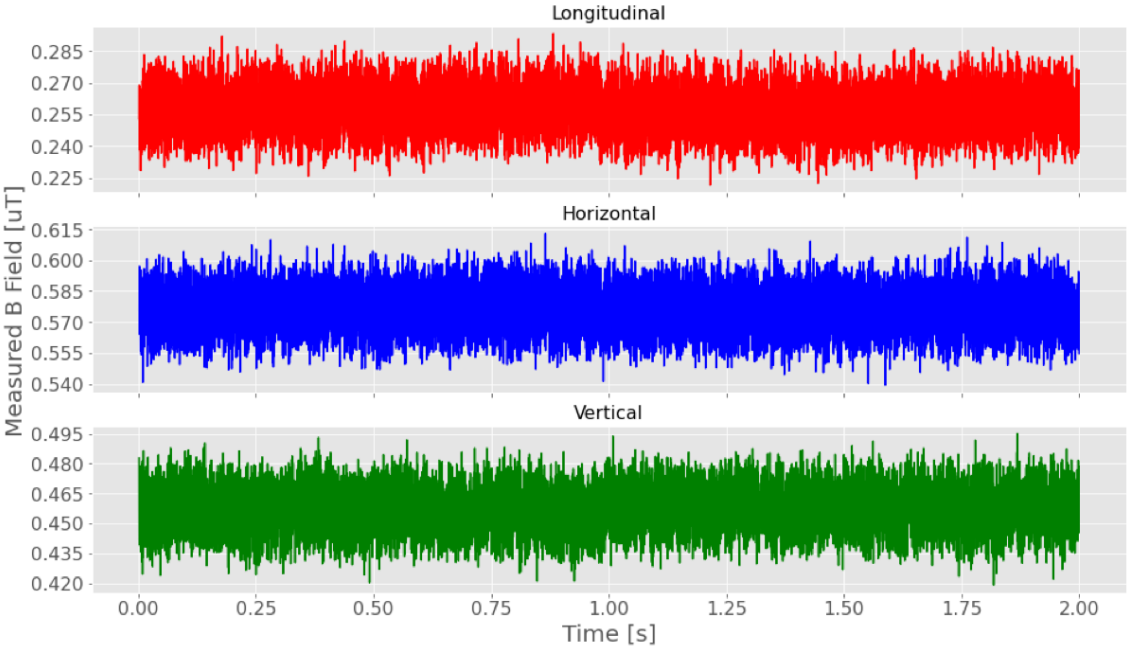

Figure 4.16.: The raw signal from figure 4.15 with a digital low pass Butterworth filter applied to it. The cut-off frequency is set at 1 kHz.

The filtered signal from figure 4.16 is zero-padded up to a 10 second signal and then Fourier transformed subsequently. The corresponding Fourier coefficients for the relevant frequency range are shown in figure 4.17. All signal components for the shielded signal are below a level of 2.5 nT. The standard deviations of the signals are 5.71 nT (longitudinal), 5.36 nT (horizontal), and 5.94 nT (vertical), respectively. It is noteworthy, however, that in all three axes we have peaks of comparable amplitudes at 30 Hz, 35.5 Hz, 57 Hz, and at 114.5 Hz, respectively. These peaks also show up in figure 4.18, where for all five mapper

fluxgates the average Fourier coefficients of the five central measurements[1] are shown for all three axes. The peaks' origin is unknown, but they can be assumed to either stem from the DAQ device or more likely from the Intel NUC. Both devices are placed within the vicinity of the measuring fluxgates and could possibly emit magnetic fields of such frequencies.

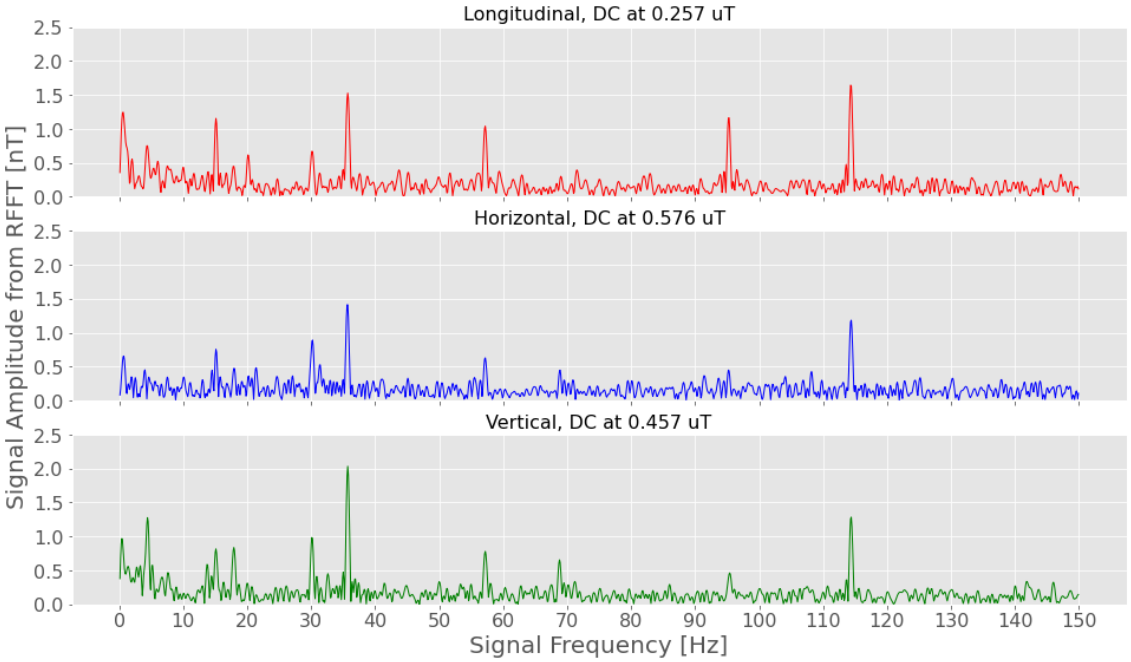

Figure 4.17.: The Fourier transform of the filtered signal from figure 4.16. The static field component for 0 Hz, i.e. the DC component, is excluded from the actual plots and its value is written in the title of their respective graph.

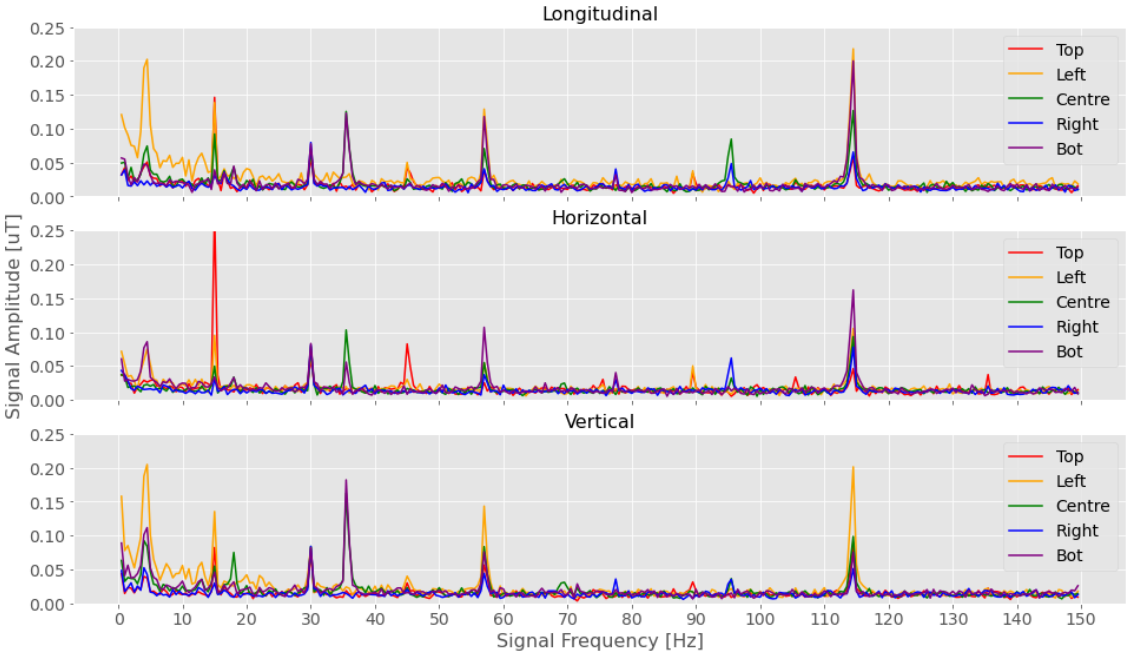

Figure 4.18.: The Fourier transformed signals of all five mapper fluxgates, averaged over the five central measurements along the beamline axis. The peaks at 30 Hz, 35.5 Hz, 57 Hz and 114.5 Hz are still visible in all five fluxgates' data sets.

[1]The five central measurements are the ones where the mapper stopped at distances of approximately 2.87 m, 2.94 m, 3.00 m, 3.06 m and 3.13 m.

4.2.2 | Shielded Background Field

The background field is measured in the same way as it has been done in section 4.1.2, but now with the full MuMetal shielding being installed. Figures 4.19 - 4.21 show the measurements in longitudinal, horizontal and vertical direction for all five fluxgates.
We see that, for all three components, the field is reduced to ±1 µT at the central 4 meters of the beamline (from 1 m to 5 m). For the longitudinal component we see a large increase of the magnetic field at the borders of the shielding up to values that are larger than in the unshielded set-up (figure 4.4). This effect is presumably caused by flux-shunting, explained in theory section 2.2. This effect would also explain the gradients in the horizontal and vertical component at the borders in figures 4.20 and 4.21. The flux-shunting effect 'attracts' the magnetic field lines so that they enter the shielding perpendicularly. Thus, this effect can lead to a local increase of the longitudinal magnetic field component, as the background field's horizontal and vertical components get redirected and will contribute to the longitudinal field.

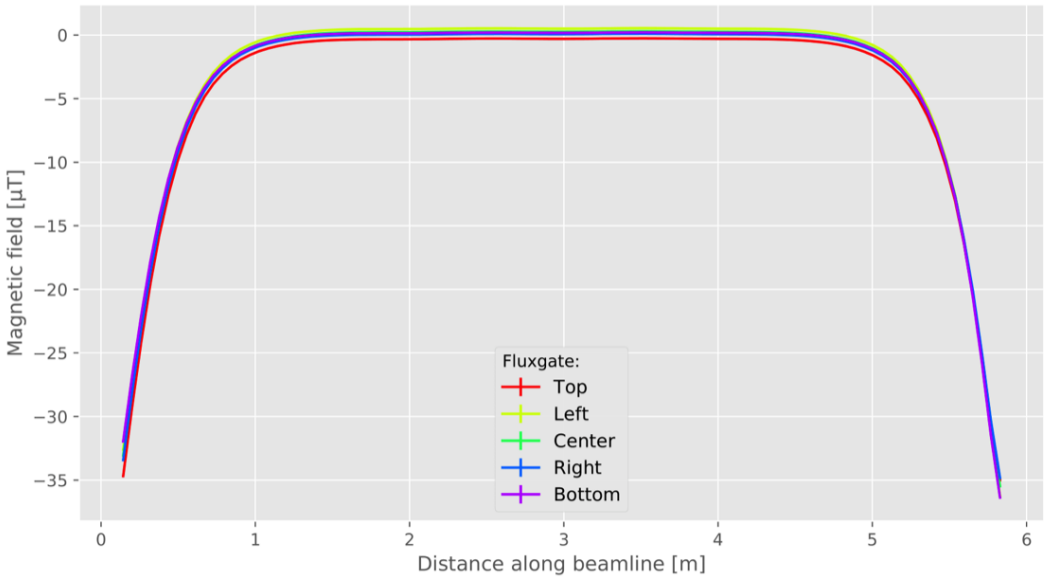

Figure 4.19.: Longitudinal component of the shielded background field.

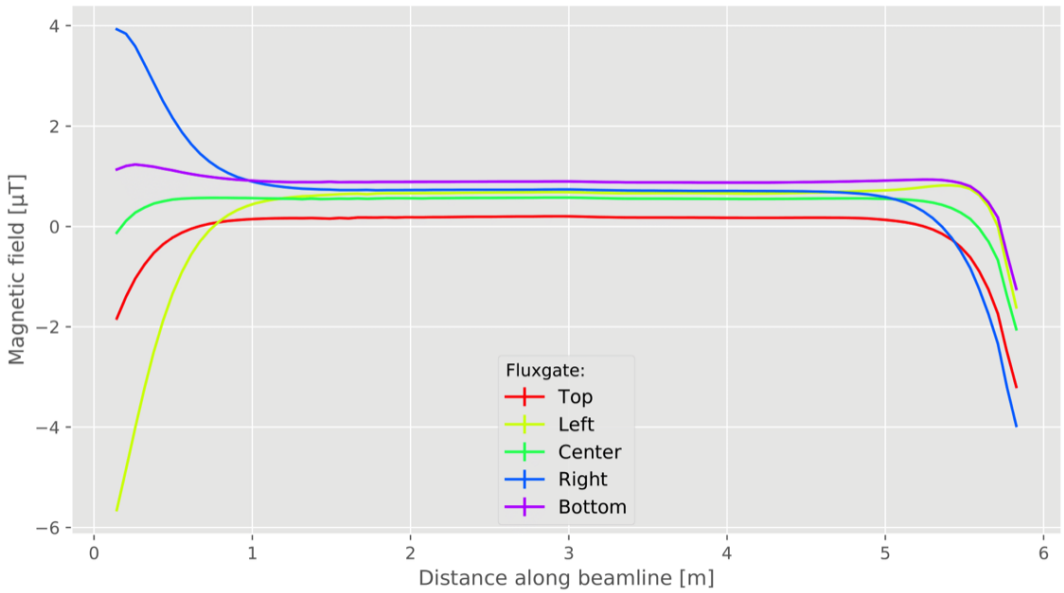

Figure 4.20.: Horizontal component of the shielded background field.

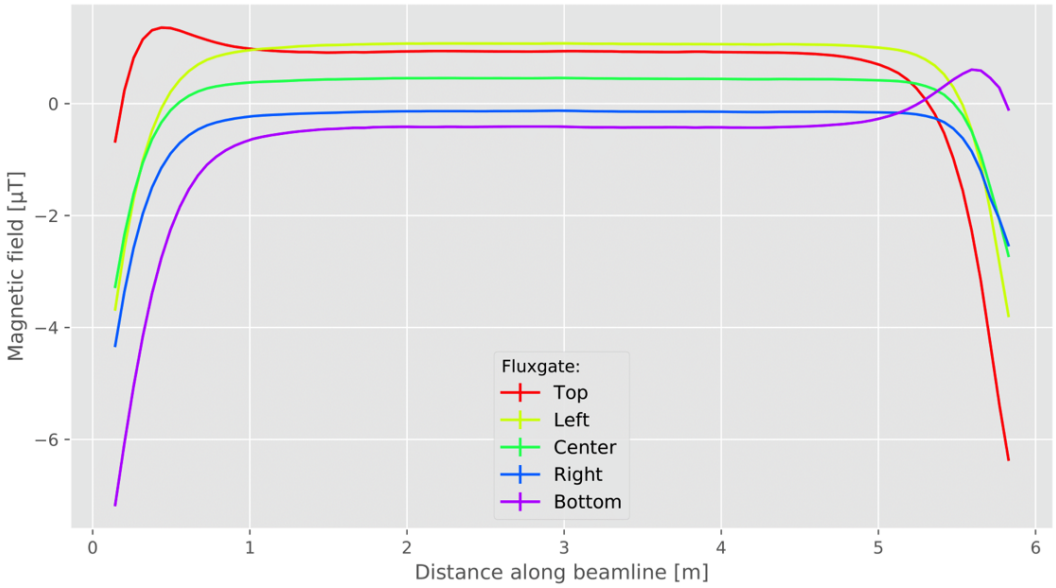

Figure 4.21.: Vertical component of the shielded background field.

4.2.3 | Shielded Room Coil Generated Static Fields

With the MuMetal shielding being installed, the field shown in figure 4.22 has been measured for a longitudinally applied field with the four coils being powered by 8 A DC current.

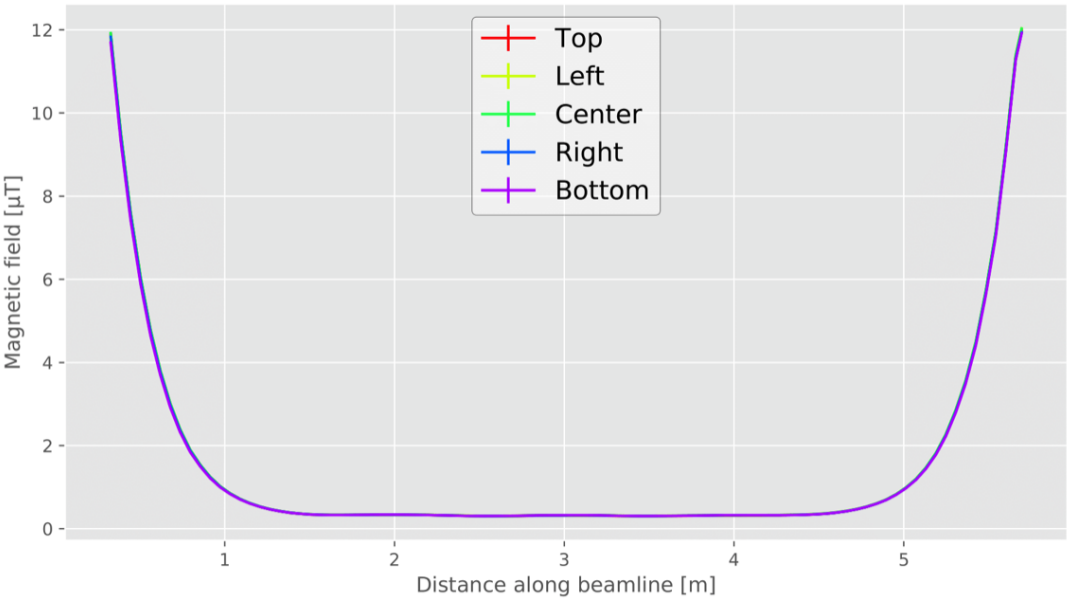

Figure 4.22.: Static magnetic field generated by the longitudinal room coils, powered by a 8 A DC current, and measured along the shielded beamline.

The plots in figures 4.23 and 4.24 show the shielded fields for the horizontally and the vertically applied fields, both generated by their respective coils, powered by a 10 A DC current.

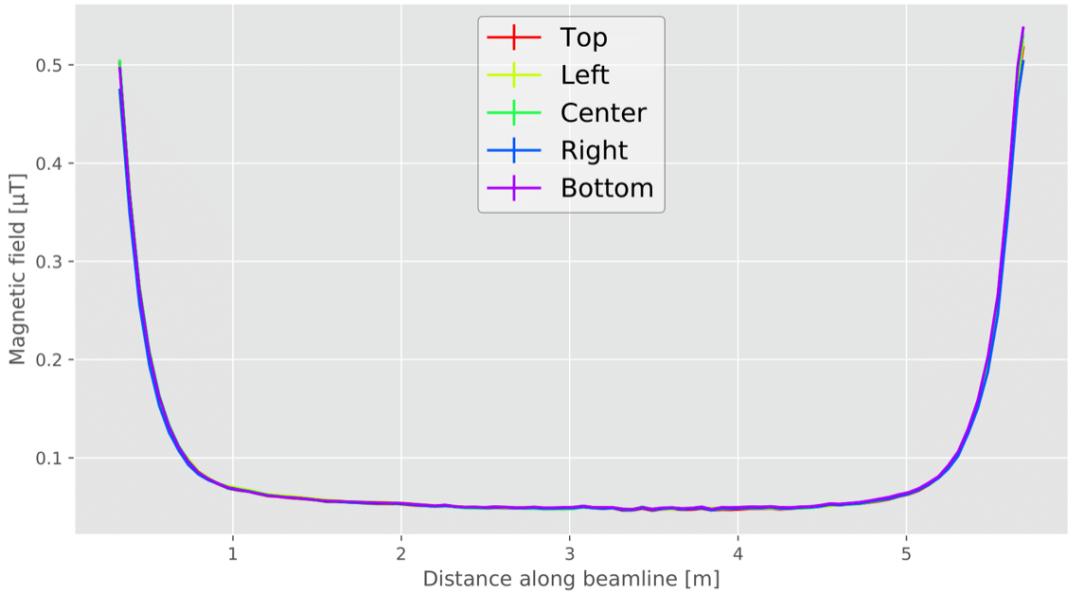

Figure 4.23.: Static magnetic field generated by the horizontal room coils, powered by a 10 A DC current, and measured along the shielded beamline.

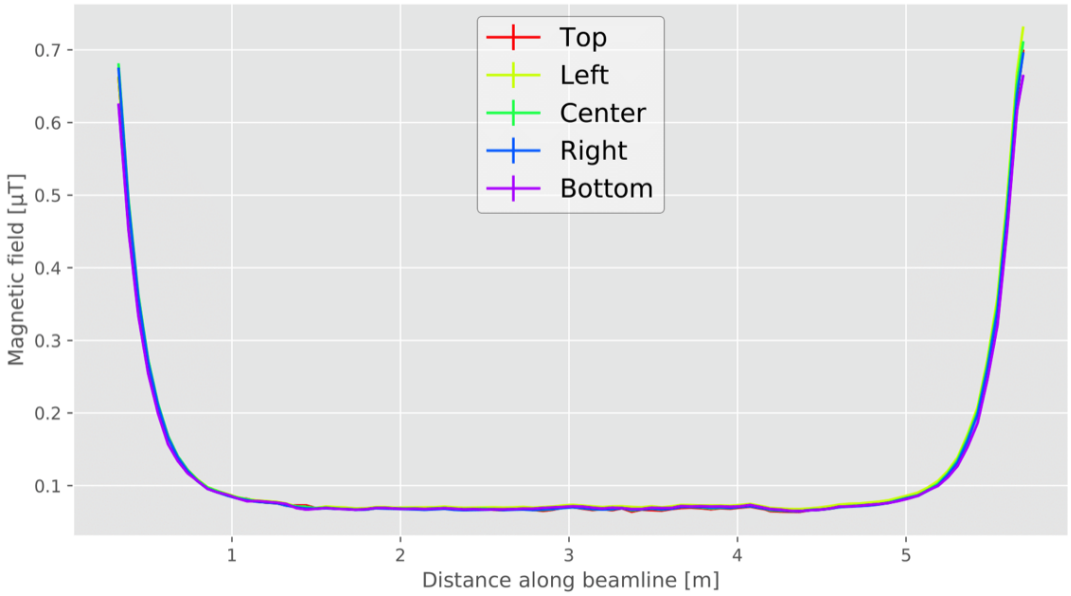

Figure 4.24.: Static magnetic field generated by the vertical room coils, powered by a 10 A DC current, and measured along the shielded beamline.

Again, all fields can be normalised to the respective applied coil current so that we can plot the gathered measured magnetic field in the respective direction per current. This is shown in figure 4.25. Only the interesting part, i.e. the centre 2 meters of the beamline where the shielding effectiveness fully applies, is shown in the plot, however.

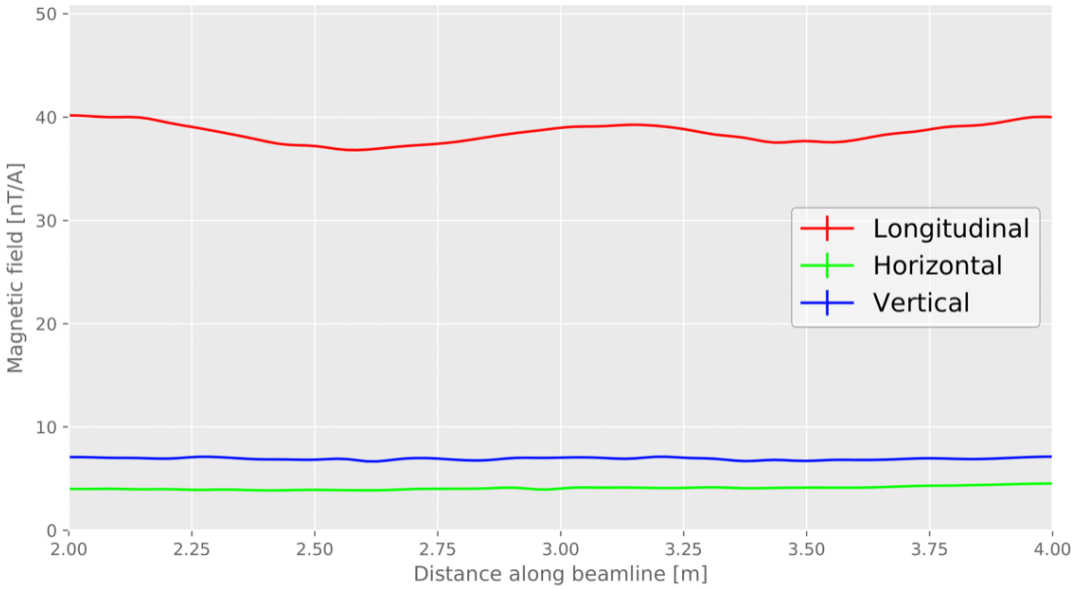

Figure 4.25.: The measured magnetic field for each direction is divided by the respective current with which the corresponding room coil was powered. Only the centre two meters on the beamline are shown here, as this represents the interesting part in this plot. Note that the scale of this plot is in nT/A.

4.2.4 | Shielded Beamline Coil Generated DC Fields

The measurements shown in section 4.1.4 have been repeated with the passive MuMetal shielding being installed. The vertical component of the magnetic field generated by the main vertical beamline coil measured by the five fluxgates (10 kHz samplerate, 2s measurement) is shown in the subsequent plot, where again the measurements are normalised to the current with which the magnetic coil has been powered (±2 A). In the main vertical direction approximately 89 µT A^{-1} are reached along the measured distance. At both ends of the beamline the vertical magnetic field strength drops by about 3 µT, while the field between 1 m and 5 m is held a constant at a level of ±0.2 µT/A. The locations of the bumps that can be observed at 1 m, 3 m and 5 m coincide with the position of the cable-connectors that form a bulge, as shown in figure 3.5b.

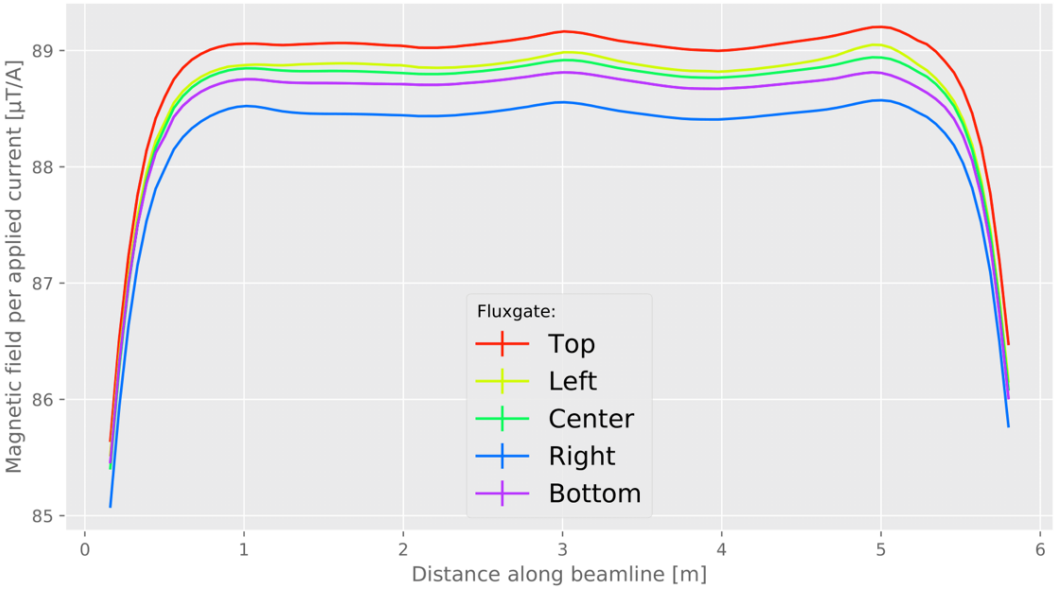

Figure 4.26.: Generated field (vertical component) of the main beamline coil, normalised to the applied current, calculated from the measured magnetic field from both coil polarities.

For the remaining secondary magnetic field components of the generated magnetic field, the longitudinal and the horizontal component respectively, the measured field is again on the order of 1 µT A^{-1}, as seen in figures 4.27 and 4.28.

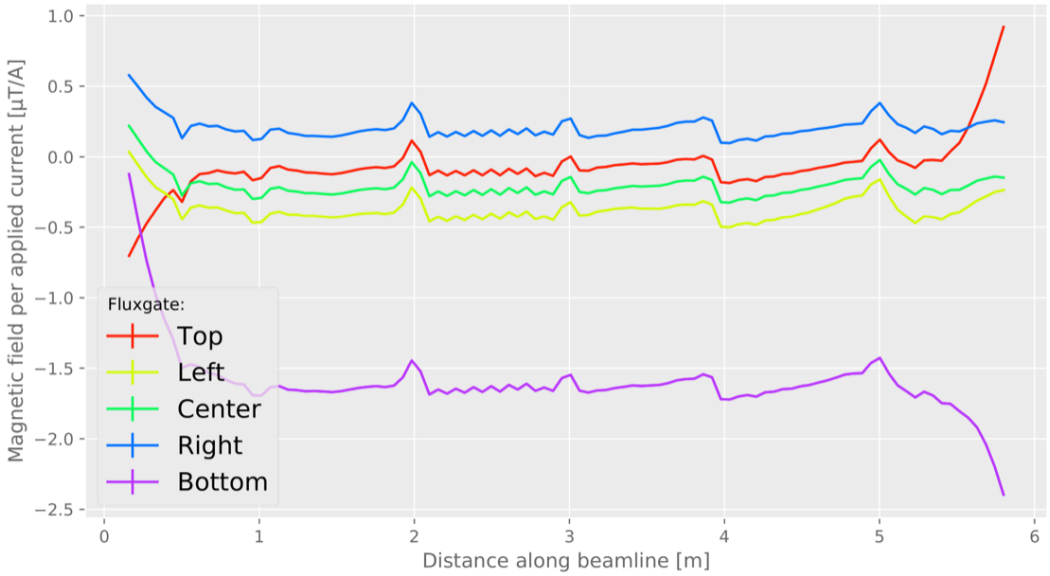

Figure 4.27.: Average generated field (longitudinal component) of the main beamline coil, normalised to the applied current, calculated from the measured magnetic field from both coil polarities.

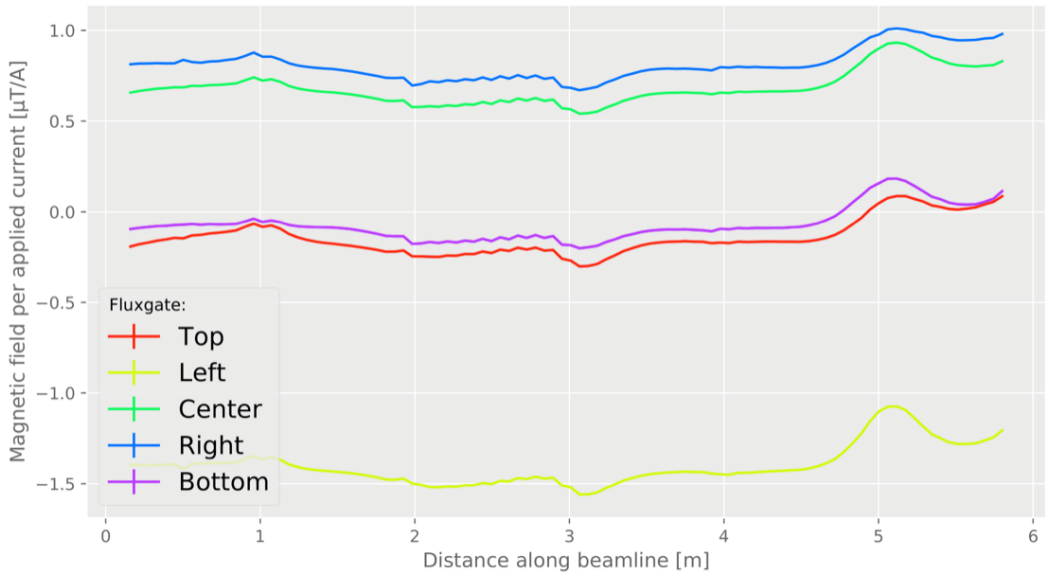

Figure 4.28.: Average generated field (horizontal component) of the main beamline coil, normalised to the applied current, calculated from the measured magnetic field from both coil polarities.

4.3 | Comparing Unshielded and Shielded Measurements

For externally generated magnetic fields, i.e. room coil generated magnetic fields, shielding factors are calculated which characterise the quality of the MuMetal shielding. Results from sections 4.1 and 4.2 are compared to each other. In a second part, we compare the vertical magnetic field component generated by the main beamline coil in the unshielded and in the shielded set-up. Furthermore, the quality, i.e. the homogeneity of the shielded beamline coil field is analysed, as this is a relevant characteristic for the BeamEDM experiment in terms of possible systematic errors. In a last, part the impact of the MuMetal feedthrough tubes (see section 3.4.2) on the shielding efficiency is studied.

4.3.1 | Shielding Factor of the Passive MuMetal Shielding for Room Coil Generated DC Fields

By comparing the measurements of magnetic field components of the shielded and unshielded case, a shielding factor can be determined for the MuMetal shielding according to equation (2.8). For each field direction, longitudinal, horizontal and vertical, the ratio between the measured fields in both cases is calculated for each fluxgate individually.
For the longitudinally applied magnetic field the shielding factor along the axis is calculated by comparing the fields which are shown in figures 4.8 and 4.22. A shielding factor maximum of about 50 is reached about 1.5 m away from the downstream end of the shielding, as can be seen in figure 4.29. On the same distance from the upstream end another local shielding maximum is found with a shielding factor of about 46. Inbetween the two maxima the shielding efficiency decreases and at the centre the shielding factor locally decreases down to 34. The average shielding factor for the central two meters of the beamline is 37.8 ± 2.7.

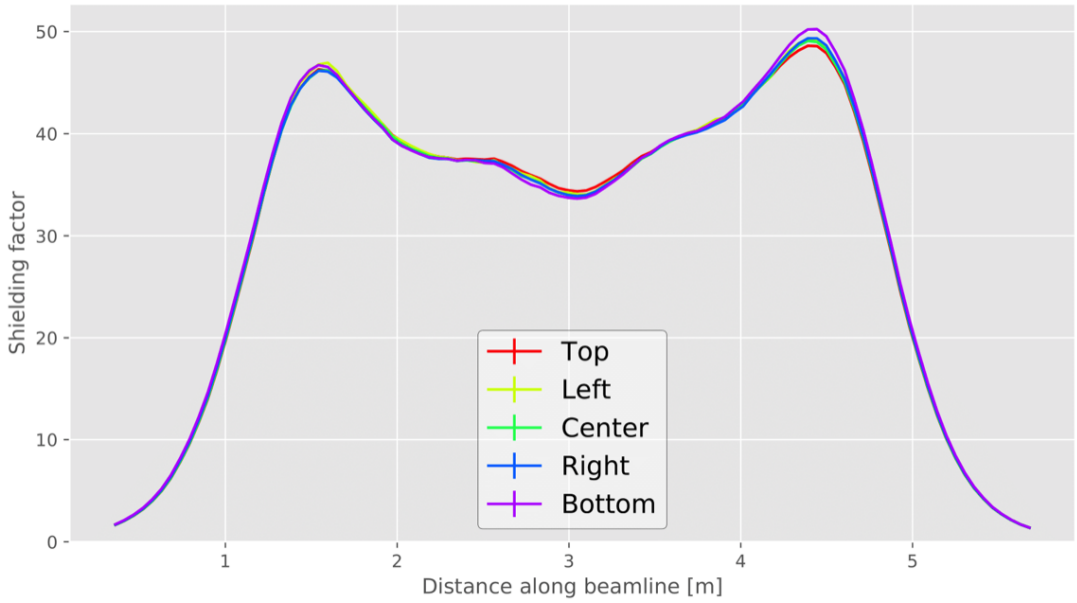

Figure 4.29.: Calculated shielding factor along the beamline for static fields applied in the longitudinal direction of the set-up.

For the shielding factor for horizontally applied magnetic fields we compare the measurements from figure 4.9 and 4.23. For horizontally applied magnetic fields we reach a shielding factor that is approximately four times as high as the one calculated for the longitudinal direction, as shown in figure 4.30. For the central two meters the average shielding factor is 196.5 ± 4.2

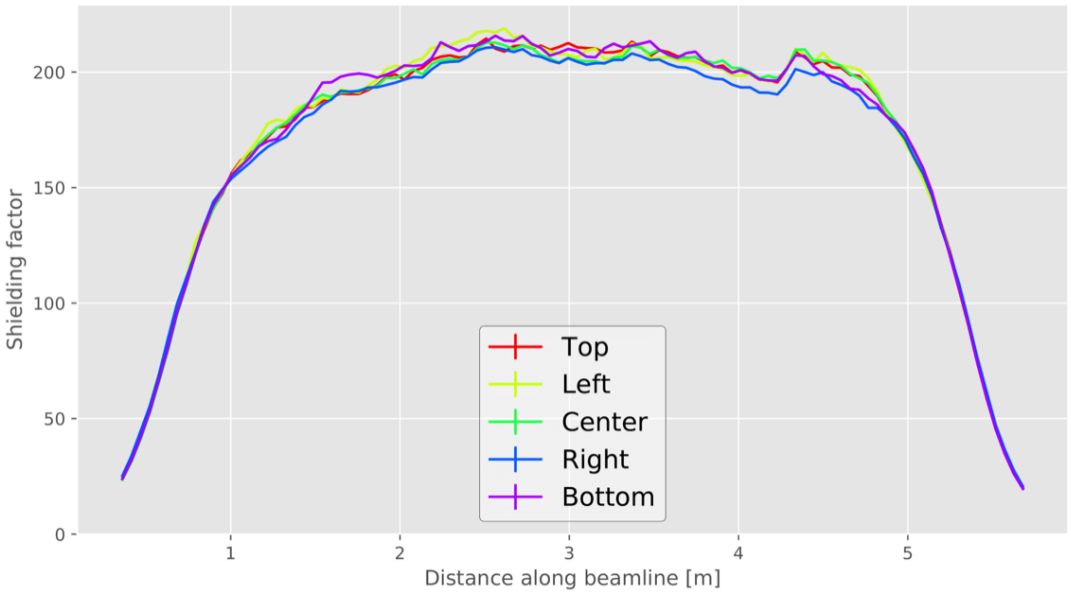

Figure 4.30.: Calculated shielding factor along the beamline for static fields applied in the horizontal direction of the set-up.

As expected from the geometry, the shielding factor in the vertical direction is comparable to the horizontal shielding factor. With an average shielding factor of 207.5 ± 3.5 for the central two metres, the shielding is about 7% higher than in the horizontal direction. The reason for this is conjectured to lie either within the different roomcoil geometry which leads to a different field homogeneity in the two directions, or within the MuMetal's openings in the bottom panels. The latter one can most probably be ruled out, as, if the openings in the bottom panels were the reason, this would lead to a visible difference between the magnetic field measured by the top and bottom fluxgate.

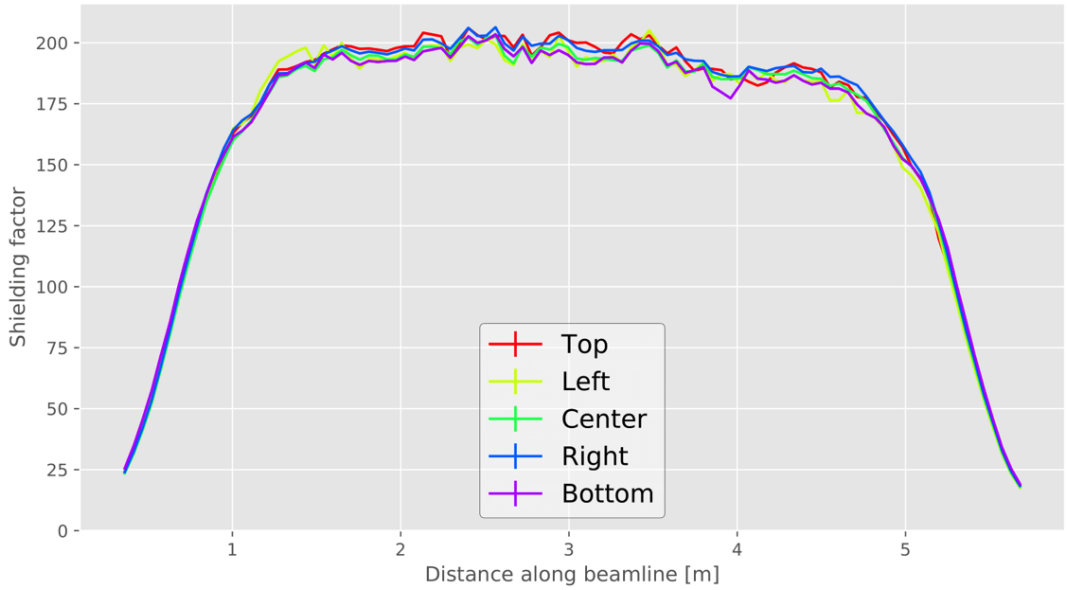

Figure 4.31.: Calculated shielding factor along the beamline for static fields applied in the vertical direction of the set-up.

For each shielding direction the average factor between the five fluxgates is calculated and shown in figure 4.32.

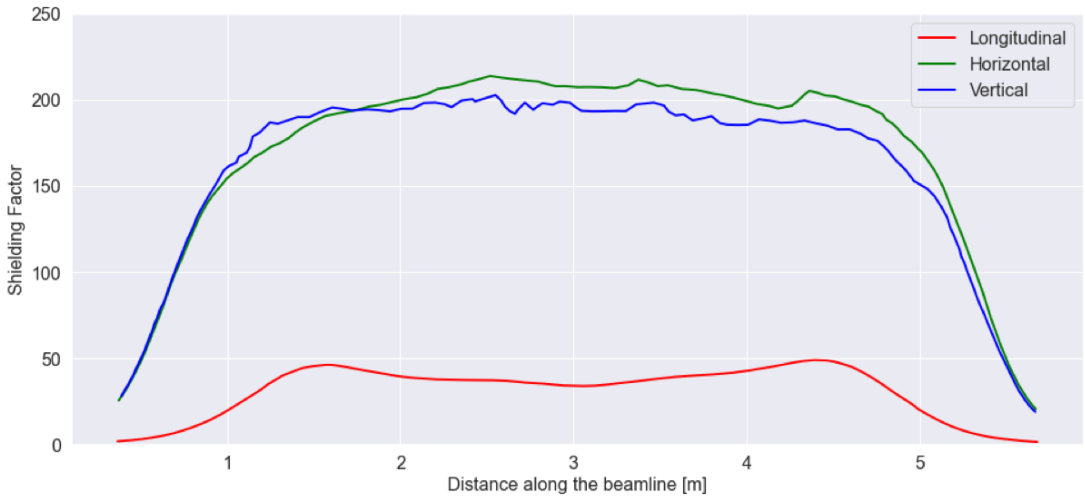

Figure 4.32.: The average shielding factor (average between the five fluxgates individually measured factors) along the beamline for individually applied fields in the longitudinal, horizontal and vertical direction.

If we look at what the theory predicts for the relation between transversal and longitudinal shielding (see theory in section 2.2.1), the measured value for the longitudinal shielding represents approximately what we would expect: For a transversal shielding of approximately $S_T = 200$ we can calculate the expected longitudinal shielding S_L with equation (2.14). We can approximate our rectangular shielding with a cylindrical shielding which has an equally large opening area, i.e. an opening radius of $\pi^{-\frac{1}{2}}$ meters and therefore a length-to-openings ratio of $p = 3 \cdot \sqrt{\pi}$. For these values we would expect the longitudinal shielding reach a factor of about 42, which fits the observations quite nicely, as the averaged shielding factor for the longitudinally applied magnetic field between 1.5 m and 4.5 m within the beamline lies at 40.95 ± 4.5.
The shape of the longitudinal shielding's graph, however, is not very easy to explain. We can see that at 1.5 m and 4.5 m shielding maxima are reached with factors of 46.15 and 48.95. The position of these maxima is a consequence of the flux-shunting effect. Their locations only coincidentally correspond to the locations of the longitudinal room coils. This is discussed later on in section 4.4.

4.3.2 | Vertical Beamline Coil Generated Field Comparison

In figure 4.33 we compare the vertical component of the magnetic field generated by the main beamline coil in the unshielded and in the shielded set-up. We can see that the MuMetal shielding enhances the field quality in terms of field strength per applied current and also in homogeneity. In the shielded set-up we have a roughly constant field between 1 m and 5 m, whereas in the unshielded set-up the field strength is constant only for the central two meters, between 2 m and 4 m. The average field strength per applied current for the shielded set-up is 88.8 ± 0.5 µT/A for the central 4 meters, which is about a factor of 1.65 higher than the generated field in the unshielded set-up. This is a consequence of the MuMetal shielding retaining magnetic flux inside the shielded region, as explained in section 2.2. A magnetic shielding is not only useful to shield a certain region from external sources, but does also confine magnetic field within a shielded region (see figure 2.1).

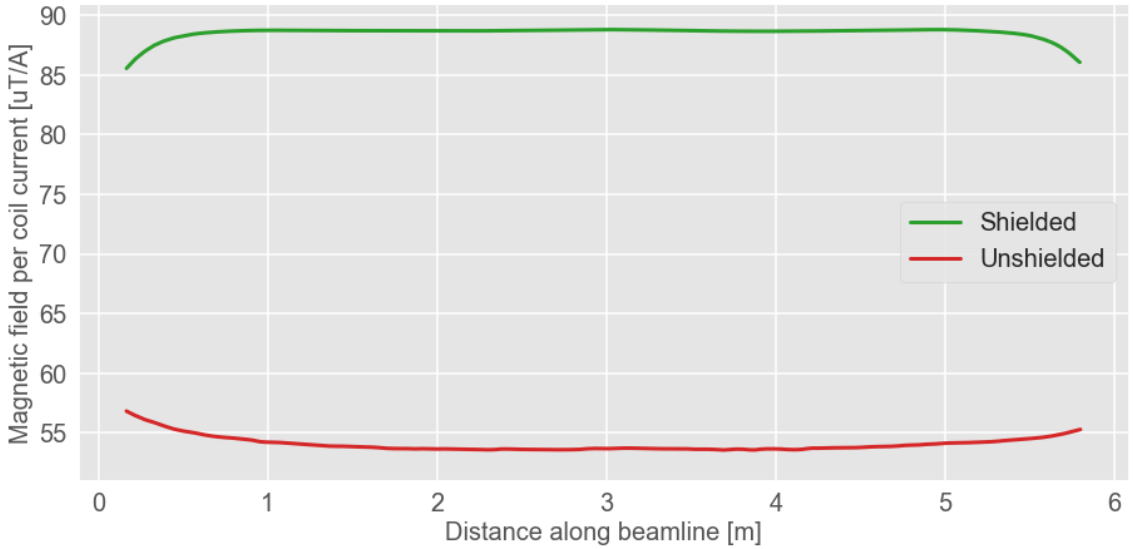

Figure 4.33.: Comparison of the vertical component of the magnetic field generated by the main beamline coil in the shielded and the unshielded set-up. The presence of the shielding increases the average field strength by a factor of 1.6. Furthermore, also the fields homogeneity is increased.

4.3.3 | Further Shielding Measurements: Feedthrough Tube Shielding

As explained in section 3.4.2 for the BeamEDM experiment it is important to know the shielding performance of the original experimental set-up with all parts of the shielding assembled in the way they will be used during the experiment. To determine the impact of the large HV feedthrough tube and the smaller vacuum-pump feedthrough tube, two additional measurements have been conducted: In a first step, only one of the tubes has been installed on one side of the shielding, namely the large HV feedthrough tube and the small tube on the bottom right, shown in figure 3.11. In a second step, all available feedthrough tubes have been installed, i.e. one HV feedthrough and four vacuum-pump feedthroughs. From the former measurement we expect to see the impact of each feedthrough type separately, while the latter measurement is a *worst case* measurement. Again, to calculate the shielding factors shown in figures 4.34 and 4.35 the magnetic field maps conducted with the respective shielding set-up are compared to the unshielded measurements from section 4.1.3. The mapper step size was set so that we have 97 measurements along the beamline and the fluxgate sample rate was set to 10 kHz again. Only the horizontal shielding performance is shown here, as this is the direction of interest as the feedthrough openings are installed on the lateral shielding plates. For the other field directions no difference in the shielding capability was noticed and the results are therefore not shown.

Separate Impact of One Large and One Small Tube

The shielding factor of the set-up with one large and one small tube installed, shown in figure 4.34, is compared to the shielding factor of the regular set-up with no tubes installed (figure 4.30). The impact of the two tubes is readily visible, as the presence of the tubes clearly decreases the horizontal shielding factor at their respective location on the x-axis. The shielding factor around the large tube's position (at 1.25 m on the x-axis) decreases by approximately 50, which is almost a 30% decrease in shielding efficiency. The impact of the smaller vacuum-pump feedthrough tube (at 4.25 m on the x-axis) is less clear, however still visible, as the shielding factor decreases by approximately 20, so roughly 10% of shielding efficiency is lost. What can be seen as well is that the most significant change in shielding efficiency is attained by the *Right*-labelled fluxgate (blue line), which is to be expected, as this is the fluxgate installed on the side facing the feedthrough tubes.

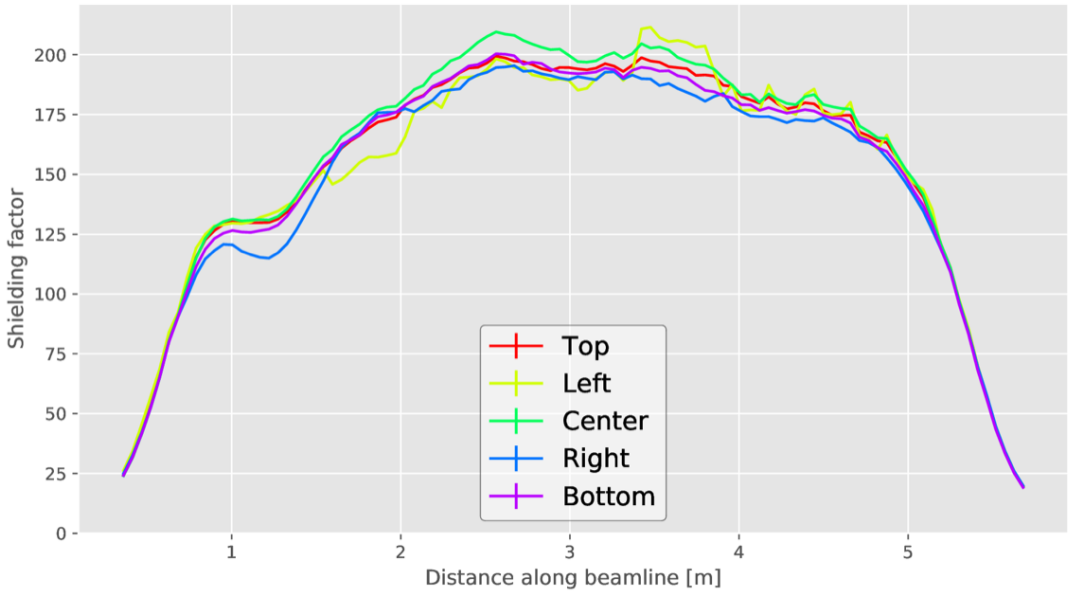

Figure 4.34.: The shielding factor for a static field applied in the horizontal direction which corresponds to the orientation of the openings of the installed feedthrough tubes. For this measurement two tubes were installed, both on the same side of the shielding. The large one (25 cm opening radius) is located at 1.249 m on the x-axis. The small tube (10 cm opening radius) is located at 4.249 m on the x-axis.

Impact of All Five Tubes

In the shielding factor measurement where all five feedthrough tubes were installed, again, a change in shielding efficiency can be seen, compared to the measurement with only two feedthrough tubes installed. The most prominent decrease in shielding efficiency is, as expected, at 2.25 m on the x-axis, where two vacuum-pump feedthroughs are installed additionally. Again, we roughly lose 10% of our shielding efficiency at the position of the smaller feedthrough tubes. There are two spikes in the shielding factor at 3.5 m and 5.15 m on the x-axis. These spikes are unexplained and are probably only artefacts of the measurements, as they are located at positions where the least impact of the feedthrough tubes is expected.

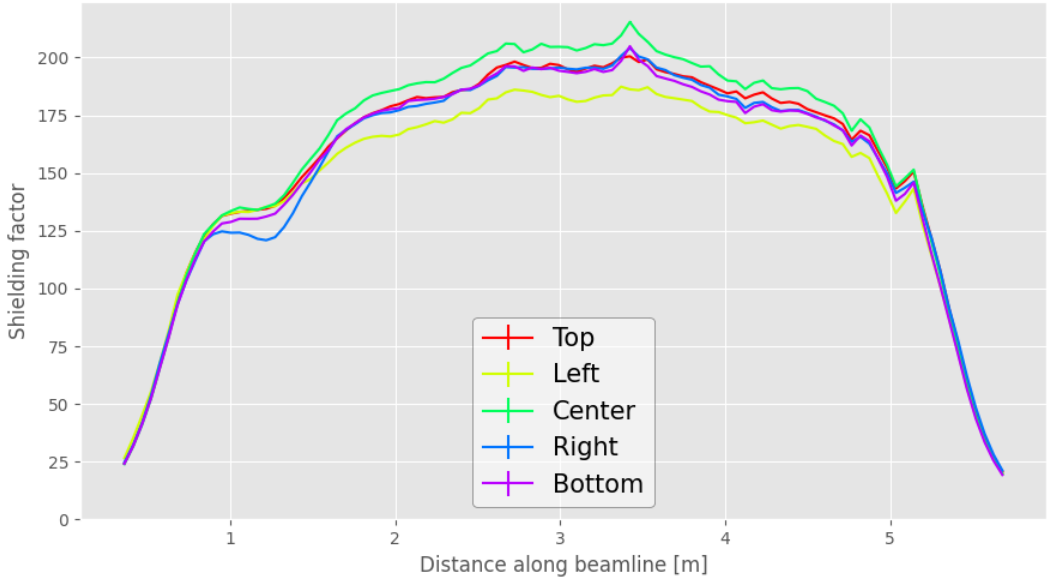

Figure 4.35.: The same measurements as in figure 4.34 but with all available feedthrough tubes installed. The shielding set-up in use is equivalent to the one shown in figure 3.11.

4.3.4 | Field Homogeneity of Shielded Beamline Coil Generated Static Fields

For the BeamEDM experiment the magnetic field provided by the beamline coils needs to reach a certain homogeneity, as the presence of a magnetic field gradient could dephase the neutron spins during the precession through the apparatus and hence diminish the visibility of the measurable Ramsey fringes [16]. If we demand less than a $\frac{\pi}{4}$ phase shift between neutrons hitting the detector on the right and the left beamspot edge with which the visibility of the signal is within an acceptable range, the gradients should not exceed $6\partial_y B_0 \approx \partial_z B_0 \lesssim \pi/(4\gamma_n T d) \approx 700$ nT/cm, where y denotes the horizontal and z the vertical direction, γ_n is the neutron's gyromagnetic ratio, T the interaction time of the neutrons with the magnetic field (which is 6 ms for a neutron velocity of 1000 m s^{-1} and a 6 m long beamline) and $d = 1$ cm is the distance between the electrodes of the BeamEDM apparatus, which at the same time represents the beam spot height. The factor 6 for the horizontal gradient has its origin in the beamspot's geometry, whose width is estimated to be six times its height.
From the measurement shown in figure 4.26 we can calculate the difference between the field measured by the top and bottom fluxgate and the left and right fluxgate to get an idea about the gradient in the vertical and horizontal gradient, respectively, by taking into account the distance between the corresponding fluxgates. For an appropriate background field correction, the considered gradient is the result from calculating the average between the gradients from both magnetic field polarities, i.e. $\Delta B = (\Delta B^+ - \Delta B^-)/2$. The following graph shows the calculated gradient of the vertical field component in vertical and in horizontal direction. For both gradients the average value and its standard deviation have been calculated and are shown at the centre position of the graphs in figure 4.36.

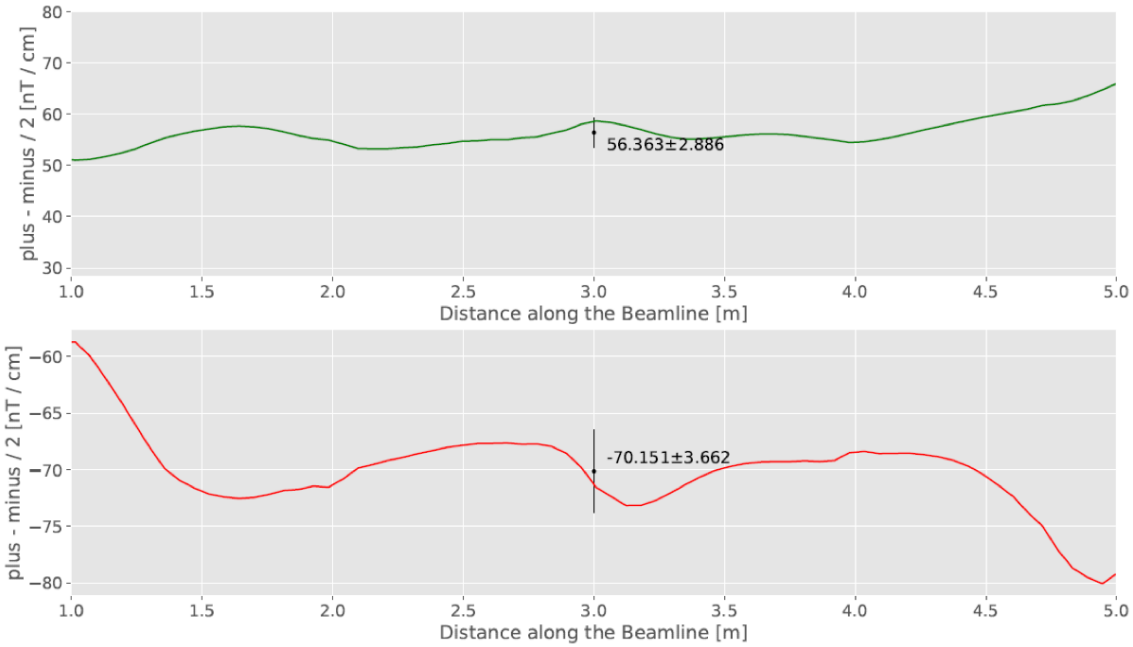

Figure 4.36.: Upper graph: The difference of the vertical field component measured by the top and bottom fluxgates per fluxgate-distance along the central section of the beamline, for a magnetic field generated by the main beamline coil with a current of 2A. The average gradient and its standard deviation have been calculated and are indicated by the labelled black dot at the centre.
Lower graph: The same procedure as for the upper graph, however the horizontal gradient of the vertical component is calculated, i.e. the difference of the measured field between the right and left fluxgate.

Both graphs are extracted from measurements where the main beamline coil has been powered with ±2 A (both polarities separately) and therefore a magnetic field strength of around $|B_0| \approx 180\,\mu T$ was generated. As for the BeamEDM measurements at ILL we desire a magnetic field strength of about 220 µT, we cannot directly say that we are within the demanded gradient range by looking at the 2 A fields. Therefore, linearity measurements have been performed and we look at the gradients that arise from the magnetic fields that are generated with 0.2 A, 0.5 A, 1 A and 1.5 A. In figure 4.37 we see the respective average values of the horizontal (*Left/Right*) and vertical (*Top/Bot*) gradients. A linear behaviour of the gradient becomes apparent and therefore we can extrapolate our gradient values to higher field strengths.

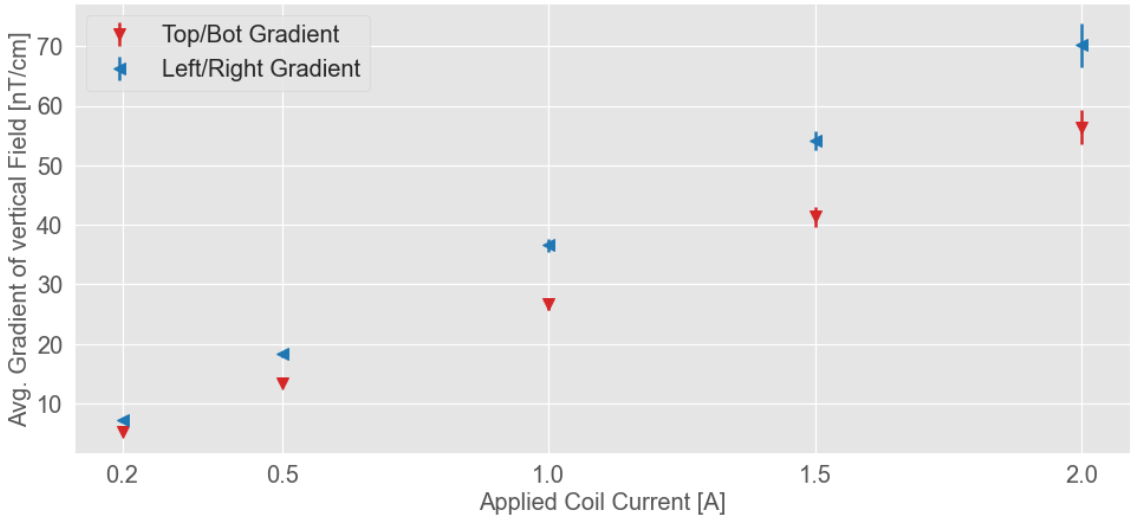

Figure 4.37.: The averages of the calculated gradients measured for different main coil operating currents. The calculation is performed in the same way as for the averages from figure 4.36.

One thing to mention is that at ILL we did not power the main coil in the exact same way as in the laboratory in Bern. At ILL the main coil was split into two separate coil loops due to power supply problems.[2] Therefore we extrapolate the generated gradient fields in terms of average field strength along the beamline and not in terms of supply current. For an average generated field strength of 220 µT along the beamline we therefore expect a gradient of $\partial_z B_0 = 69.74 \pm 3.6$ nT/cm and $\partial_y B_0 = 86.8 \pm 5.1$ nT/cm. For both directions we lie below our demanded gradient threshold.
One thing that we should bear in mind when analysing the gradients here is that we cannot be entirely sure whether the gradients measured along the beamline are constant or if they drift over time. An interesting thing to measure would be to have the mapper at a fixed position and continuously measure the gradient over a certain time span.

4.4 | FEM Simulations of Comparable MuMetal Shielding Set-Ups

We compare the measured shielding factors to values that are simulated for a comparable set-up using a finite element (FEM) simulation study that is conducted with the software COMSOL version 5.3a. COMSOL's *AC/DC module* has been employed as it includes a

[2] As described in section 3.2 the main beamline coil consisted out of a single loop with 7 cable windings. At ILL the coil was split into two separate loops with 3 windings and 4 windings. To reach the demanded field strength of 220 µT the loops were powered with 2.95 A and 1.8 A, respectively.

reliable solver for magnetostatic problems, including magnetic shielding phenomena [35].

The simulated MuMetal shielding is a simplified form of the real shielding from figure 3.10. It is built up from two shieldings of the same dimensions as our MuMetal shielding, however both layers are built from a single piece and, apart from the two openings at both ends, feature no holes, connecting pieces or other additional parts. The shielding is embedded in an ambient domain of air of size $10\,\mathrm{m} \times 5\,\mathrm{m} \times 3\,\mathrm{m}$. The simulated shielding, as shown in figure 4.38, is exposed to static homogeneous magnetic fields that are applied in transversal, horizontal and vertical direction with respect to the shielding by imposing boundary conditions for the surrounding magnetic field on the ambient domain. The magnetic field strength is chosen to be of the same strength as the fields that were applied for the measurements in section 4.1.3 and 4.2.3, respectively. To determine a shielding factor, the ratio of the magnetic field strength along a central line cut (illustrated in figure 4.38) is calculated for the two cases where the shielding is present and absent, respectively.

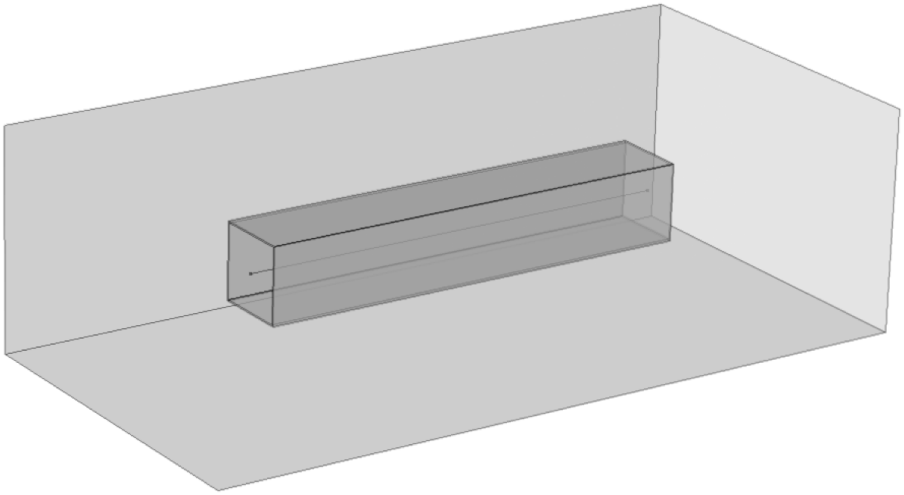

Figure 4.38.: The simulated shielding scenario consists of two layers of MuMetal have a thickness of 1.57 mm with a gap spacing of 2 cm in between. Boundary conditions for surrounding magnetic fields can be imposed onto the ambient domain walls, so that a homogeneous magnetic field can be applied to the shielding.

4.4.1 | Matching the Shielding's Relative Permeability μ from the Measurements

For the simulation a choice for the relative permeability μ of the MuMetal shielding has to be made. Common table values for the relative permeability of MuMetal range from 80'000 up to 500'000, depending on the exact composition of the alloy and the quality of the processing. In order to make a first estimation for the parameter we make use of equations (2.11), (2.14) and (2.15) and insert the results obtained from our shielding factor measurements. From the theory it follows that a relative permeability of $\mu =$ 103'000 leads to a shielding factor of 200 transversely and 42 longitudinally which is a good approximation of our measurements (see figure 4.32). With this value for μ set within the simulations the longitudinally simulated shielding matches quite well with the measured values, as can be seen in figure 4.39. Albeit the peaks' locations on the x-axis are not perfectly matched, a similar shape is reproduced. As for the measurement the applied external magnetic field is not perfectly homogeneous in direction (especially for the longitudinal field), deviations are expected to occur in comparison to the simulation, where the applied fields are perfectly homogeneous. The inhomogeneity within the applied field strength, however, was found to have no major influence on the shielding capability of the

set-up. This behaviour is expected since the shielding factor is constant with the applied field strength. With the same choice of parameters the shielding for transversely applied fields was simulated. As can be seen in figure 4.40 the transversal shielding is largely overestimated by the simulation with the same choice of μ =103'000. The simulated shielding factor is larger by a factor of approximately 5, compared to the measurement. Additional attempts to match the transversal shielding with a different value of μ showed, that a relative permeability of $\mu = 41'000$ yields the best match for simulated and measured transversal shielding. This is also apparent in figure 4.40. Now, if this value of the relative permeability is used to simulate the transversal shielding again, as expected, the simulated value lies below the measured one, off by a factor of approximately 2.5.

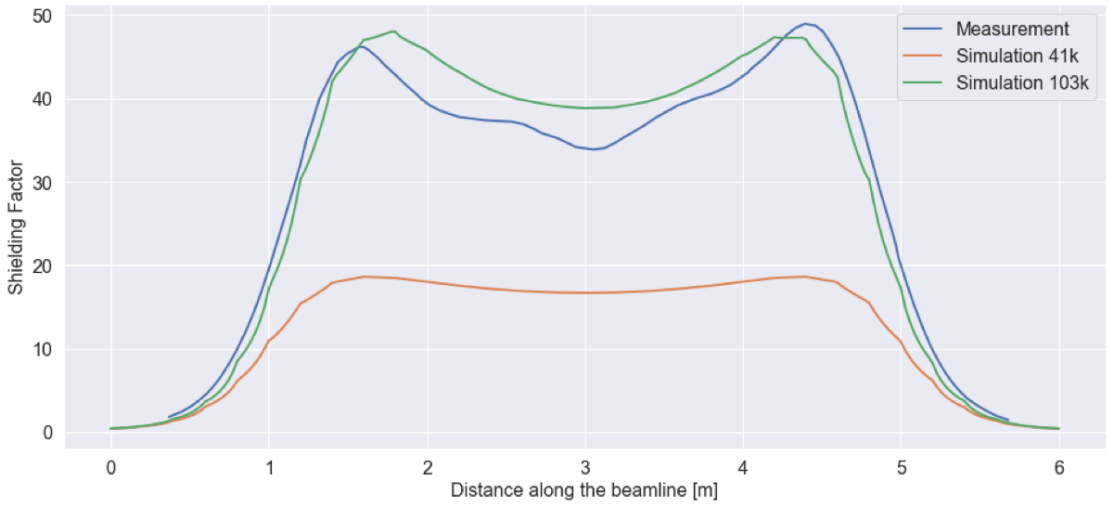

Figure 4.39.: Simulated longitudinal shielding factor for two different relative permeabilities, compared with the measured longitudinal shielding factor from figure 4.29. The simulation with the theory predicted relative permeability of $\mu = 103'000$ matches well with the measurement. With a relative permeability of $\mu = 41'000$ the shielding is underestimated by a factor of approximately 2.5.

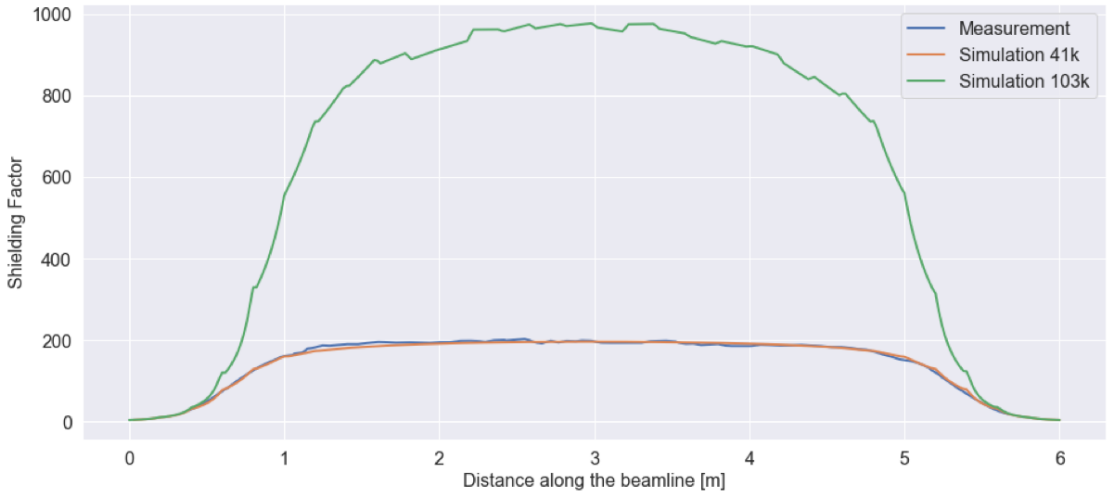

Figure 4.40.: Simulated transversal shielding factors compared with the measured vertical shielding factor from figure 4.32. With the theory predicted relative permeability of $\mu = 103'000$ the simulation overestimates the shielding by a factor of approximately 5. The best match between simulation and measurement was found with a value of $\mu = 41'000$.

Although we cannot reproduce the measured shielding factors with a single simulation set-up, we gain insight on the behaviour of the MuMetal shielding. In particular, the occurrence of the shielding maxima in the longitudinal shielding is not surprising anymore and the correlation between the location of said maxima and the position of the two central

longitudinal room coil loops is presumably only of accidental nature, since said maxima are reproduced with a perfectly homogeneous simulated field.

5 | Magnetic Field Background at ILL, Grenoble

All of the above measurements for the characterisation of the MuMetal shielding has been conducted before the actual beam time at Grenoble, where the BeamEDM experiment took place in August 2020. During the BeamEDM experiment, five fluxgates have been installed around the experimental set-up to measure the magnetic background field prevailing at the experimental zone PF1b. The same type of fluxgates (FLC3-70) that was installed on the magnetic field mapper has been used. Four fluxgates have been installed on the legs of the aluminium scaffold, as shown in figure 5.1, whereas one fluxgate was installed above the whole set-up, in a roughly centred way. All fluxgates have been installed in the same orientation. All three axes are read out with a 1 Hz rate over an irregular time period of 35 days (the irregularities originating from front-end shutdowns of the central DAQ software). The externally recorded magnetic field can be compared to the magnetic field that is recorded within the beamline area. To monitor the internal magnetic field (used for the active magnetic field stabilisation, inter alia), eight fluxgates (*SENSYS FGM3D/250*) are installed along the beamline, as indicated by the blue labels in figure 5.1. They are placed approximately 32 cm away from the bottom or from the top shielding plate, respectively. The internal fluxgates, just like the external ones, are read out with a 1 Hz sample rate.

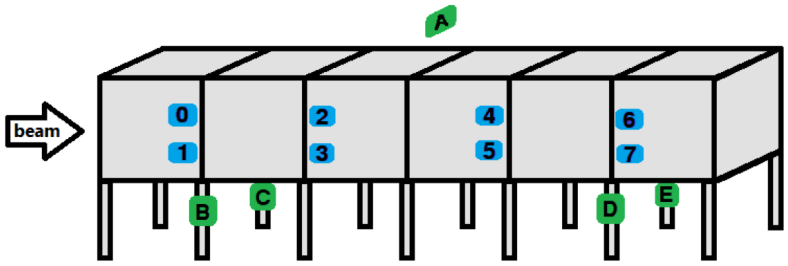

Figure 5.1.: Sketch of the positioning of the external fluxgates positioning (in green) and the internal fluxgates positioning (in blue) at ILL, PF1b. The neutron beam direction is indicated by the arrow on the left. Four external fluxgates (*B, C, D, E*) are installed on the second and fifth leg of the set-up, in 40 cm distance to the shieldings bottom plates. The fifth fluxgate (*A*) is installed in a roughly centred manner above the set-up. It is placed at a distance of 613 mm to the shieldings top plates and 220 mm off the longitudinal centre of the set-up, nearer to he upstream end. In blue the approximate positions of the internal fluxgates and their labelling is shown. Their mounting structure can be seen in figure 3.2.

Fully Shielded Background Field

We analyse the magnetic field data of two separate events. The first data series that is looked at was recorded after the completed installation of all shielding components, i.e. MuMetal and RF-shielding (16.08.2020, 21:30 CEST). After the installation was completed, the experimental site has been left at 02:00 a.m. and all relevant devices around the set-up have been shut down. During the following ∼7 hours we expect to observe an undisturbed background field that is originating only in non BeamEDM related sources. The next logbook entry is timestamped at 09:00 am, when the $ArCO_2$ gas valves have been opened and when possibly someone was working near the fluxgates. Figure 5.2 shows the magnetic field magnitude measured by the external fluxgate *FGA* and the magnitude measured by the internal fluxgate *FG2*. Besides the magnetic fields, also the measured temperature of the shielding plate below *FGA* is plotted.

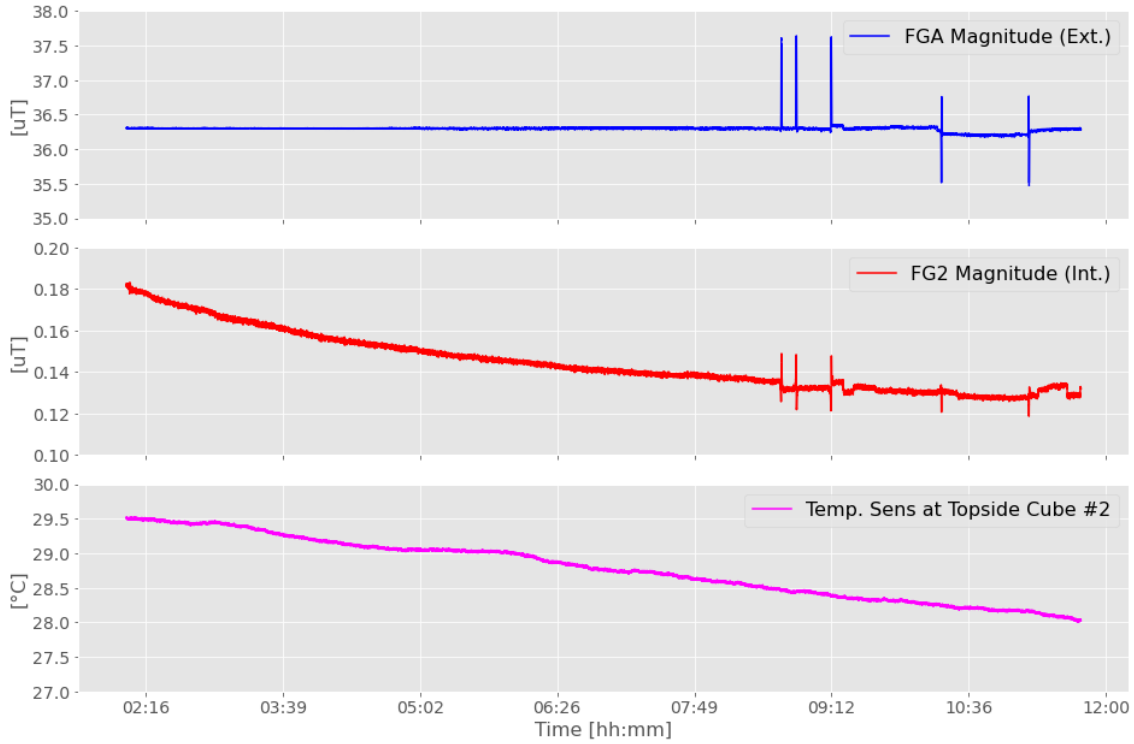

Figure 5.2.: The magnetic field magnitude recorded by the external fluxgate *FGA* (blue) and the internal fluxgate *FG2* (red) during the night of the 17.08.2020 where only background field from non BeamEDM related sources is expected. In pink also the temperature of the MuMetal shielding is plotted over time.

We can see that during the night the actual background field stays rather constant. Until 4 a.m. we have fluctuations on the order of 5 nT, then some unknown source begins to generate fluctuations of ∼40 nT. The spikes at around 9 a.m. which are supposedly caused by somebody coming by the experimental set-up in PF1b, have amplitudes of ~ 1.3 µT. These spikes are simultaneously monitored on the internal fluxgate, however, there, the spike-amplitude is only on the order of 14 nT and therefore approximately two orders of magnitude smaller. This is more or less the shielding effectivity we would expect to occur after having characterised the shielding in the previous sections. With the 1 Hz sample rate data of the fluxgates only quasi-static magnetic fields are recorded, for which the shielding factors are comparable to our static field shielding factors [30]. Here we have to pay attention, however, as we cannot directly infer the shielding factor here from comparing magnetic fields recorded at different locations, since we don't know the exact source of the noise and how its signal would translate into the unshielded set-up. Because keep in mind, that to calculate the shielding factor we compare the magnetic field measured at the same location, measured with and without the shielding in presence.
From the internal fluxgate data we can observe an exponential decrease of the magnetic field over time, which isn't observed on the series of external data. This is presumably some remanent magnetisation that is left within the MuMetal shielding, as this was the only ferromagnetic component in use. Another reason could be that the effect has its origin in the temperature decrease of the MuMetal shielding. In contrast to the decreasing magnetic field, the temperature falls linearly over time, however. Thus, a sole correlation between temperature and remanent magnetisation of the MuMetal seems to be rather unlikely.

Actively Stabilised Magnetic Field during Axion Measurements

The second data series of magnetic fields that we look at was measured during a 24 hour axion measurement with 1'400 separate runs with continuous, non-pulsed neutron beams. For these measurements a vertical magnetic field of 220 µT was generated by the vertical beamline coils and the field was actively stabilised using the other beamline coils. The field stabilisation was set in a way, so that the average of the magnetic field components by the four inner internal fluxgates was held constant on the desired value (220 µT vertically and 0 µT horizontally and longitudinally). The stabilisation is executed with a 10 Hz rate. For this purpose the internal fluxgates are running with a 10 kHz sample rate and for each stabilisation cycle the mean average of 1'000 samples is calculated and fed into a PID control loop algorithm.[1] In figure 5.3 four plots are shown: The data of the external fluxgate *FGA* and the internal fluxgate *FG2* are shown. Additionally the field measured by internal fluxgate *FG7* is shown, which is a fluxgate that is on the downstream ending of the set-up and which is not considered for the active field stabilisation. Last but not least, the average magnitude of the stabilised field is shown. It is calculated as the norm of the vector composed of the individual stabilised magnetic field components.[2]
The background noise is rather constant at a level between 36 µT and 36.7 µT. Again we have some momentary events that cause spikes of 1.7 µT amplitude. These spikes are not visible on the data series of *FG2*, but only on the outer fluxgate *FG7*. This is as expected, since the combination between active and passive magnetic field stabilisation should be able to nullify such disturbances from the central beamline area.
In the fourth data line in figure 5.3 we see that the stabilised magnetic field magnitude scatters around the desired 220 µT. The individual measurements are Gaussian distributed around a mean value which lies 19.86 fT above the intended value, with the standard deviation of the distribution being 414 pT. If we look at the individual stabilised field components and their average deviations from the target values, for the full time-span of the axion measurement series we calculate the values shown in table 5.1. With a mean magnetic field of 18.52 fT the horizontal component is best adjusted to its target value. The dispersion around the mean value is on the same order of magnitude, i.e. $\sim 5 \times 10^{-4}$ µT, for all three directions.

	Target Value	Mean Deviation
Longitudinal	0 µT	$(-1.32 \pm 461) \times 10^{-6}$ µT
Horizontal	0 µT	$(+0.02 \pm 414) \times 10^{-6}$ µT
Vertical	220 µT	$(-0.54 \pm 615) \times 10^{-6}$ µT

Table 5.1.: The measured mean deviation from their target value during the 24 hour axion measurement cycle for the respective magnetic field direction.

[1] The PID's *I* and *D* parameters were effectively set to 0, whereas the P parameter was set to 1.
[2] The longitudinal component is the average of the longitudinal components of *FG2, FG3, FG4* and *FG5*, and analogously for the horizontal and vertical axis.

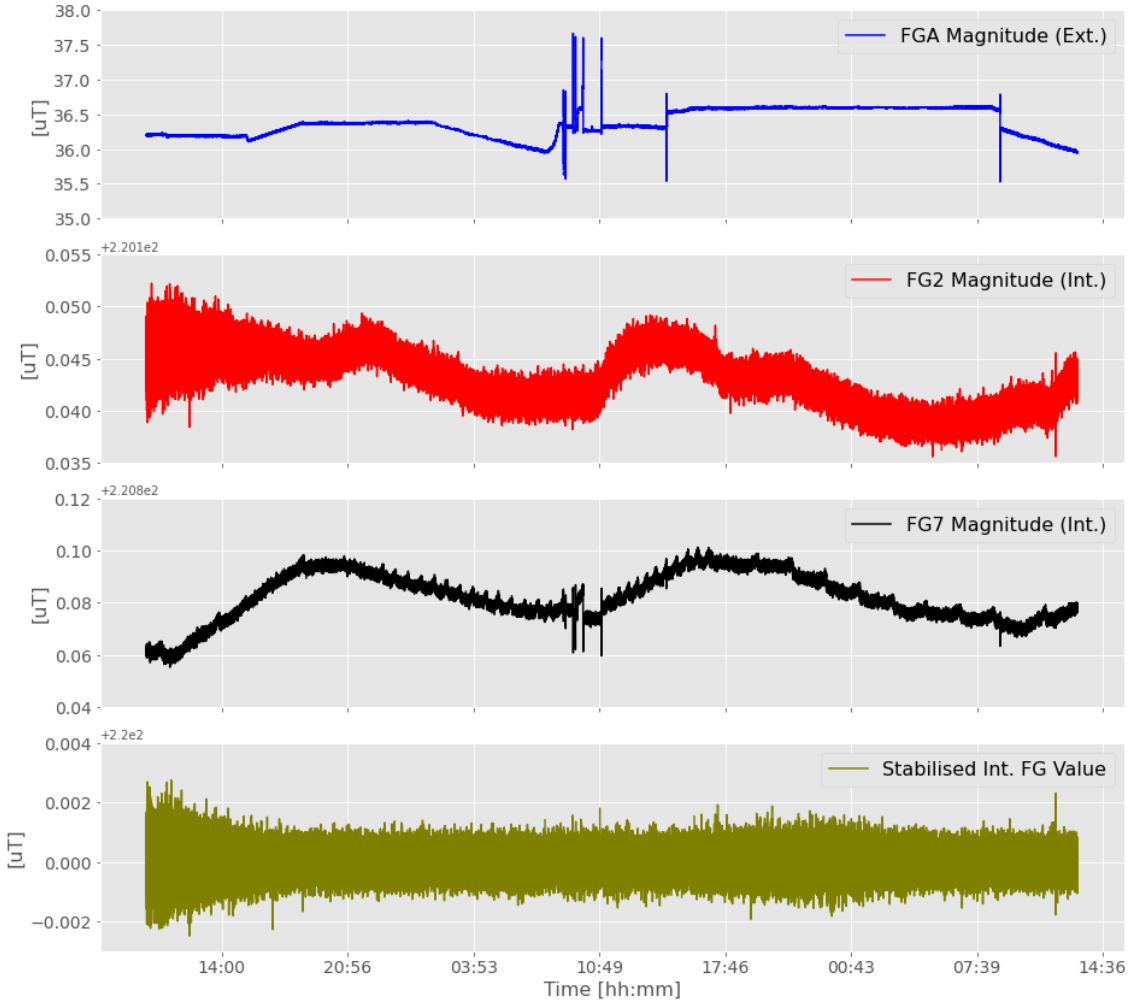

Figure 5.3.: The magnetic field magnitude recorded by the same fluxgates as shown for the previous measurement (*FGA* (blue) and *FG2* (red)) during a 24 hour axion data taking measurement with the active magnetic field stabilisation up and running. Additionally, the field measured by *FG7* is shown, which is one of the internal fluxgates near the downstream end of the shielding and which is not directly considered for the active magnetic field stabilisation. As a fourth quantity the magnetic field part which is actively stabilised is shown in olive. It is the component-wise average measured by the four central fluxgates, i.e. *FG2*, *FG3*,*FG4*, and *FG5*.

6 | Discussion

In chapter 3 the utilised set-up for the shielding characterisation has been described. The process of how raw fluxgate data is processed in order to calculate shielding factors has been exemplified on two example data sets of both, data obtained in shielded and unshielded measurements. Along the set-up's beamline five fluxgates measure the magnetic field in all three axes in discrete measurements of 2 seconds with a 10 kHz sample rate. To get rid of fluxgate generated aliased noise a low-pass filter is applied to the recorded data, whereof the DC component is analysed for the static field shieldings, or the individual alternating field components are analysed by means of its Fourier transform to deduce the shielding effectivity for alternating fields. With this procedure, the MuMetal shieldings individual shielding factors for static fields applied in different directions have been determined in this thesis. The shielding of static magnetic fields generated by the three sets of room coils happens in an expected manner and reaches shielding factors that are comparable to theoretically predicted values. Longitudinally, the two-layer MuMetal shielding is found to decrease static magnetic background fields with a factor of approximately 41 (see figure 4.29). For laterally applied static fields, shielding factors of 197 horizontally and 208 vertically are reached. Further measurements have been conducted with MuMetal feedthrough tubes installed, as they are needed for the BeamEDM's final set-up design. The impact on the static shielding factors reach from a local 10% decrease in shielding factor, caused by separately installed small tubes, up to a local 30% decrease in the shielding factor at the position where the large feedthrough is installed. Furthermore, the magnetic field generated by the vertical beamline coil has been investigated. The installation of the MuMetal shielding resulted in an increase of the generated magnetic field by a factor of 1.6. The respective field homogeneity after the installation of the shielding was examined and found to meet the minimum requirements for a sufficient visibility of the Ramsey fringes. The practicability of the shielding in use has then been investigated by looking at two data sets of magnetic fields recorded by fluxgates installed at the experimental site at PF1b at ILL, Grenoble, during the beamtime in August 2020. The evaluation of the data coarsely showed an expected shielding of external magnetic noise by the passive MuMetal shielding, according to the preceding shielding characterisation. Likewise, the interplay between active and passive shielding has been looked at by means of magnetic field data taken during a 24 hour experimental run with neutron data taking. During this run no correlation between the magnetic background field and the field measured at the centre domain of the beamline, where the field is actively stabilised, was found. Moreover, magnetic background incidents are shielded with an (estimated) factor 50 at the shieldings openings.

The conducted COMSOL simulations shown in section 4.4 delivered a cautious insight into the magnetic fields behaviour for the longitudinal shielding of static fields. It would be worth further pursuing the simulations in order to be able to predict the shieldings behaviour under certain changes. Once both, the longitudinal and the lateral shielding factors of the simulation and the measurements agree, one could investigate into geometrical optimisations of the shielding by means of the simulation. This could include possible optimisations of the shieldings thickness or e.g. the spacing between the two shielding layers.

Potential Improvements to the Measuring Method and the Set-Up

There are several factors that could improve the quality of the shielding characterisation. A first obvious potential improvement could come from reworking the mapper's design in such a way, that the amount of magnetic instruments on it is reduced. The current design leads to unforeseeable residual magnetic field, especially for alternating magnetic fields, since unknown and irregular magnetic fields could be generated by e.g. the mapper's INTEL NUC or the batteries in use. Since the batteries, for instance, are not even at a very fixed position on the mapper, as they need to be detachable for the sake of recharging, their influence on the measurement is different from sequence to sequence. Therefore, a mapper equipped with fluxgates only would be more optimal for these measurements. Another source of disregarded magnetic background stems from the possible magnetisation of the MuMetal itself. This problem could be approach by two possible solutions. On one hand, background measurements could have been conducted more frequently, i.e. before every single measurement sequence, and not only at the beginning of the day how it has been conducted most of the times. On the other hand, one could get rid of the shielding's remanent magnetisation by degaussing it. This could be realised by applying an alternating magnetic field of decreasing strength using the room coils. However, this should then be done between every measurement sequence, such that no additional background field is inflicted on the measurements. The analysed ILL magnetic field data from figure 5.2 showcases the importance of the degaussing procedure for the shielding characterisation. Another investigation that would be interesting to make is to repeat room coil measurements with the vertical beam line coil field turned on at 220 µT. Due to the increased governing field strength the shielding is urged towards its saturation point, which could strongly influence the shielding capability of the MuMetal. However, according to the MuMetal manufacturer's specifications we are far off from reaching the materials saturation point, which is stated to be at around 0.75 T [36]. Nevertheless, an investigation in this direction would remain interesting, as it is unknown if our MuMetal in use meets those indicated specifications.

A | Appendix

Fluxgate Offset Measurements

Each individual fluxgate that has been installed on the mapper has been put into a Helmholtz coil of the type found in [37]. Each fluxgate's characterstic offsets have been evaluated and are listed in the following table.

Fluxgate	Label	Offset [µT]
19	Top X	0.33911
	Top Y	0.23858
	Top Z	-1.92251
20	Left X	1.36046
	Left Y	0.66886
	Left Z	0.63859
UB20	Centre X	-0.77279
	Centre Y	-0.16056
	Centre Z	0.17728
UB17	Right X	-0.19206
	Right Y	-0.61549
	Right Z	-0.92718
UB19	Bottom X	-0.02581
	Bottom Y	-0.11857
	Bottom Z	-0.12929

Table A.1.: Measured fluxgate offsets in µT for all five fluxgates and their three respective axes.

References

[1] C. S. Wu, E. Ambler, R. W. Hayward, D. D. Hoppes, and R. P. Hudson. Experimental test of parity conservation in beta decay. Phys. Rev., 105:1413–1415, Feb 1957. doi: 10.1103/PhysRev.105.1413. URL https://link.aps.org/doi/10.1103/PhysRev.105.1413.

[2] J. H. Christenson, J. W. Cronin, V. L. Fitch, and R. Turlay. Evidence for the 2π decay of the k_2^0 meson. Phys. Rev. Lett., 13:138–140, Jul 1964. doi: 10.1103/PhysRevLett.13.138. URL https://link.aps.org/doi/10.1103/PhysRevLett.13.138.

[3] Julian Schwinger. The theory of quantized fields. i. Phys. Rev., 82:914–927, Jun 1951. doi: 10.1103/PhysRev.82.914. URL https://link.aps.org/doi/10.1103/PhysRev.82.914.

[4] G Lüders. On the equivalence of invariance under time reversal and under particle-antiparticle conjugation for relativistic field theories. Dan. Mat. Fys. Medd., 28(5): 1–17, 1954. URL https://cds.cern.ch/record/1071765.

[5] Makoto Kobayashi and Toshihide Maskawa. CP-Violation in the Renormalizable Theory of Weak Interaction. Progress of Theoretical Physics, 49(2):652–657, 02 1973. ISSN 0033-068X. doi: 10.1143/PTP.49.652.

[6] Andrei D Sakharov. Violation of cp invariance, c asymmetry and baryon asymmetry of the universe. Soviet Physics Uspekhi, 34(5):392–393, may 1991. doi: 10.1070/pu1991v034n05abeh002497. URL https://doi.org/10.1070/pu1991v034n05abeh002497.

[7] Michael Dine and Alexander Kusenko. Origin of the matter-antimatter asymmetry. Reviews of Modern Physics, 76(1):1–30, Dec 2003. ISSN 1539-0756. doi: 10.1103/revmodphys.76.1. URL http://dx.doi.org/10.1103/RevModPhys.76.1.

[8] C. L. Bennett, M. Halpern, G. Hinshaw, N. Jarosik, A. Kogut, M. Limon, S. S. Meyer, L. Page, D. N. Spergel, G. S. Tucker, and et al. First-year wilkinson microwave anisotropy (wmap) observations: Preliminary maps and basic results. The Astrophysical Journal Supplement Series, 148(1):1–27, Sep 2003. ISSN 1538-4365. doi: 10.1086/377253. URL http://dx.doi.org/10.1086/377253.

[9] Antonio Riotto and Mark Trodden. Recentprogress inbaryogenesis. Annual Review of Nuclear and Particle Science, 49(1):35–75, Dec 1999. ISSN 1545-4134. doi: 10.1146/annurev.nucl.49.1.35. URL http://dx.doi.org/10.1146/annurev.nucl.49.1.35.

[10] P. Schmidt-Wellenburg. The quest to find an electric dipole moment of the neutron, 2017.

[11] Shahida Dar. The neutron edm in the sm: A review. arXiv preprint hep-ph/0008248, 2000.

[12] C. Abel and et al. Measurement of the permanent electric dipole moment of the neutron. Phys. Rev. Lett., 124:081803, Feb 2020. doi: 10.1103/PhysRevLett.124.081803. URL https://link.aps.org/doi/10.1103/PhysRevLett.124.081803.

[13] Norman F. Ramsey. A molecular beam resonance method with separated oscillating fields. Phys. Rev., 78:695–699, Jun 1950. doi: 10.1103/PhysRev.78.695. URL https://link.aps.org/doi/10.1103/PhysRev.78.695.

[14] S Arzumanov, L Bondarenko, S Chernyavsky, W Drexel, A Fomin, P Geltenbort, V Morozov, Yu Panin, J Pendlebury, and K Schreckenbach. Neutron life time value measured by storing ultracold neutrons with detection of inelastically scattered neutrons. Physics Letters B, 483(1):15–22, 2000. ISSN 0370-2693. doi: https://doi.org/10.1016/S0370-2693(00)00579-7. URL https://www.sciencedirect.com/science/article/pii/S0370269300005797.

[15] P.A. Zyla et al. Review of Particle Physics. PTEP, 2020(8):083C01, 2020. doi: 10.1093/ptep/ptaa104.

[16] Florian M. Piegsa. New concept for a neutron electric dipole moment search using a pulsed beam. Phys. Rev. C, 88:045502, Oct 2013. doi: 10.1103/PhysRevC.88.045502. URL https://link.aps.org/doi/10.1103/PhysRevC.88.045502.

[17] ILL Institut Laue-Langevin Grenoble. Pf1b: Polarised cold neutron beam facility - instrument description. URL https://www.ill.eu/users/instruments/instruments-list/pf1b/characteristics. Online; accessed 23 February 2021.

[18] Helmut Schober. Neutron Scattering Instrumentation, pages 37–104. Springer US, Boston, MA, 2009. ISBN 978-0-387-09416-8. doi: 10.1007/978-0-387-09416-8_3.

[19] E. Weber. Electromagnetic Fields: Mapping of fields. Electromagnetic Fields. Wiley, 1950.

[20] Celozzi Salvatore, Rodolfo Araneo, and Giampiero Lovat. Electromagnetic Shielding. 2008.

[21] J. F. Hoburg. Principles of quasistatic magnetic shielding with cylindrical and spherical shields. IEEE Transactions on Electromagnetic Compatibility, 37(4):574–579, 1995. doi: 10.1109/15.477342.

[22] A. Mager. Magnetic shielding efficiencies of cylindrical shells with axis parallel to the field. Journal of Applied Physics, 39(3):1914–1914, 1968. doi: 10.1063/1.1656455. URL https://doi.org/10.1063/1.1656455.

[23] A. Mager. Magnetic shields. IEEE Transactions on Magnetics, 6(1):67–75, 1970. doi: 10.1109/TMAG.1970.1066714.

[24] J. A. Osborn. Demagnetizing factors of the general ellipsoid. Phys. Rev., 67:351–357, Jun 1945. doi: 10.1103/PhysRev.67.351. URL https://link.aps.org/doi/10.1103/PhysRev.67.351.

[25] T J Sumner, J M Pendlebury, and K F Smith. Convectional magnetic shielding. Journal of Physics D: Applied Physics, 20(9):1095–1101, sep 1987. doi: 10.1088/0022-3727/20/9/001. URL https://doi.org/10.1088/0022-3727/20/9/001.

[26] J.F. Hoburg. A computaitional methodology and results for quasistatic multilayered magnetic shielding. IEEE Transactions on Electromagnetic Compatibility, 38, No.1:92–103, 1996. doi: 10.1109/15.485702.

[27] Valery Korepanov and Andriy Marusenkov. Flux-gate magnetometers design peculiarities. Surveys in Geophysics, 33(5):1059–1079, June 2012. doi: 10.1007/s10712-012-9197-8. URL https://doi.org/10.1007/s10712-012-9197-8.

[28] Wikimedia Commons. Schematics of a fluxgate magnetometer, 2015. URL https://de.wikipedia.org/wiki/Fluxgate-Magnetometer#/media/Datei:Magnetometro_fluxgate.svg. File: Magnetometro_fluxgate.svg.

[29] Stefan Mayer Instruments. Datenblatt dreiachsiger fluxgate-magnetfeldsensor flc3-70. URL https://stefan-mayer.com/images/datenblaetter/Datenblatt_FLC3-70.pdf. Online; accessed 19 November 2020.

[30] Andreas Gsponer. Characterization of magnetic shielding for the beam edm experiment. Master's thesis, University of Bern, Hochschulstrasse 6, 3012 Bern, 2 2021. Supervisor: Prof. Florian Piegsa.

[31] Magnetic Shields Ltd. Mumetal material technical data, 2018. URL https://magneticshields.co.uk/technical/material-technical-data. Online; accessed 24 January 2021.

[32] S. Sgobba. Physics and measurements of magnetic materials, 2011.

[33] Shlomo Engelberg. Digital Signal Processing: An Experimental Approach. Springer Publishing Company, Incorporated, 1st edition, 2008. ISBN 1848001185.

[34] NGDC NOAA GOV. Earth magnetic field calculator. URL https://www.ngdc.noaa.gov/geomag/calculators/magcalc.shtml#igrfwmm. Online; accessed 03 January 2021.

[35] COMSOL Multiphysics GmbH. Comsol ac/dc module for electromagnetic fem simulations. URL https://www.comsol.com/acdc-module. Online; accessed 20 March 2021.

[36] Magnetic Shields Ltd. Mumetal b(h) curve, 2018. URL https://magneticshields.co.uk/technical/b-h-curves-mumetal-50-nife. Online; accessed 03 March 2021.

[37] S.L. Serviciencia. 600 mm helmholtz coils data sheet, 2011. URL http://www.serviciencia.es/folletos/BH600B-En1.pdf. Online; accessed 03 March 2021.

Erklärung

gemäss Art. 30 RSL Phil.-nat. 18

Name/Vorname: Gottstein Alexander Leonard

Matrikelnummer: 14-120-927

Studiengang: Physik

Bachelor ☐ Master ☑ Dissertation ☐

Titel der Arbeit: Passive Magnetic Shielding Characterisation for Static Fields within the BeamEDM Experiment

LeiterIn der Arbeit: Prof. Florian Piegsa

Ich erkläre hiermit, dass ich diese Arbeit selbständig verfasst und keine anderen als die angegebenen Quellen benutzt habe. Alle Stellen, die wörtlich oder sinngemäss aus Quellen entnommen wurden, habe ich als solche gekennzeichnet. Mir ist bekannt, dass andernfalls der Senat gemäss Artikel 36 Absatz 1 Buchstabe r des Gesetzes vom 5. September 1996 über die Universität zum Entzug des auf Grund dieser Arbeit verliehenen Titels berechtigt ist.
Für die Zwecke der Begutachtung und der Überprüfung der Einhaltung der Selbständigkeitserklärung bzw. der Reglemente betreffend Plagiate erteile ich der Universität Bern das Recht, die dazu erforderlichen Personendaten zu bearbeiten und Nutzungshandlungen vorzunehmen, insbesondere die schriftliche Arbeit zu vervielfältigen und dauerhaft in einer Datenbank zu speichern sowie diese zur Überprüfung von Arbeiten Dritter zu verwenden oder hierzu zur Verfügung zu stellen.

Ort/Datum

Bern, 31. März 2021

Unterschrift